X-Shooting ULLYSES: Massive stars at low metallicity

XIII. Putting the bi-stability jump to the test in the LMC

T. Alkousa[1], P.A. Crowther[1], J.M. Bestenlehner[1, 2], H. Sana[3], F. Tramper[4], J.S. Vink[5], D. Pauli[3], J.Th. van Loon[6], F. Najarro[4], R. Kuiper[7], A.A.C. Sander[8], M. Bernini-Peron[8], and The XShootU collaboration

[1] Astrophysics Research Cluster, School of Mathematical and Physical Sciences, University of Sheffield, Hicks Building, Hounsfield Road, Sheffield S3 7RH, United Kingdom e-mail: `Talkousa1@sheffield.ac.uk`
[2] School of Chemical, Materials and Biological Engineering, University of Sheffield, Sir Robert Hadfield Building, Mappin Street, Sheffield S1 3JD, United Kingdom
[3] Institute of Astronomy, KU Leuven, Celestijnenlaan 200D, B-3001, Leuven, Belgium
[4] Departamento de Astrofísica, Centro de Astrobiología, (CSIC-INTA), Ctra. Torrejón a Ajalvir, km 4, 28850 Torrejón de Ardoz, Madrid, Spain
[5] Armagh Observatory and Planetarium, College Hill, Armagh BT61 9DG, United Kingdom
[6] Lennard-Jones Laboratories, Keele University, ST5 5BG, United Kingdom
[7] Faculty of Physics, University of Duisburg-Essen, Lotharstraße 1, D-47057 Duisburg, Germany
[8] Zentrum für Astronomie der Universität Heidelberg, Astronomisches Rechen-Institut, Mönchhofstr. 12-14, 69120 Heidelberg

ABSTRACT

Context. Due to the important role massive stars ($> 8 M_\odot$) play in galactic evolution across cosmic ages, it is important to obtain a deeper understanding of the behaviour of mass-loss in low metallicity environments, which largely determines the path a massive star takes throughout its life and its final fate. This would allow us to better predict the evolution of massive stars in the early universe.
Aims. We aim to investigate the theoretical bi-stability jump, which predicts an increase in mass-loss rates below $T_{\rm eff} \approx 25-21$ kK. We further aim to constrain the photospheric and wind parameters of a sample of LMC late-O and B-supergiant.
Methods. We utilise the 1D, non-LTE radiative transfer model CMFGEN in a grid-based approach, and subsequent fine-tuned spectroscopic fitting procedure that allows us to determine the stellar and wind parameters of each star. We apply this method to ultra-violet data from the ULLYSES programme and complementary optical data from the XShootU collaboration. We also utilise evolutionary models to obtain the evolutionary masses and compare them to our derived spectroscopic masses.
Results. We derive physical parameters and wind properties of 16 late O- and B-supergiants that span a wide temperature range $T_{\rm eff} \approx 12-30$ kK, surface gravity range $\log (g/{\rm cm\,s^{-2}}) \approx 1.8-3.1$, and a mass-loss rate range $\dot{M} \approx 10^{-7.6}-10^{-5.7}$ $M_\odot\,{\rm yr^{-1}}$. We also compare our results to previous studies that attempted to investigate the metallicity dependence of wind properties.
Conclusions. We find that our derived photospheric and wind properties are consistent with multiple previous studies. For most of our sample, we find that the evolutionary masses and the spectroscopic masses are consistent within the uncertainties. Our results do not reproduce a bi-stability jump in any temperature range, but rather a monotonic decrease in mass-loss rate at lower temperatures. We obtain a wind terminal velocity-effective temperature relation for LMC supergiants $v_\infty/{\rm km\,s^{-1}} = 0.076(\pm 0.011)T_{\rm eff}/{\rm K} - 884(\pm 260)$. We find that our derived mass-loss rates do not agree with the mass-loss rates predicted by any of the numerical recipes. This is also the case for the ratio of the terminal wind velocity to the escape velocity $v_\infty/v_{\rm esc}$, and we derive the relation $v_\infty/v_{\rm esc} = 4.1(\pm 0.8) \log (T_{\rm eff}/{\rm K}) - 16.3(\pm 3.5)$. We find that there is a metallicity dependence of wind parameters from a comparison with a previous SMC study, and we obtain the modified wind momentum-luminosity relation $\log D_{\rm mom}^{\rm LMC} = 1.39(\pm 0.54) \log (L_{\rm bol}/L_\odot) + 20.4(\pm 3.0)$.

Key words. stars: massive, stars: early-type, stars: mass-loss, supergiants, stars: atmospheres, stars: winds, outflows

1. Introduction

Massive stars ($> 8M_\odot$) are hot and luminous stars that possess powerful winds that provide significant radiative, chemical and mechanical feedback to their surroundings at every evolutionary stage . Due to significant mass-loss via stellar winds, the evolution of massive stars cannot be predicted solely by determining the initial mass, so the mass that is lost throughout the life of a massive star could be the difference between its life ending in core-collapse supernova (ccSNe II/Ib/Ic) and leaving behind a black hole (BH) or a neutron star (NS) or directly collapse to a BH without a ccSN (Smartt 2009).

Massive stars are rare by absolute numbers, but their high temperatures, and subsequently, their extreme ultra-violet (UV)

fluxes are thought to have played an essential role in re-ionizing the Universe (Haiman & Loeb 1997). Their ionizing radiation may also drive star formation in their host galaxies (Crowther 2019)

Massive stars eject mass during all evolutionary stages via stellar winds. In the advanced evolutionary stages (supergiants), their stellar winds become more powerful than on the zero age main sequence (ZAMS), leading to copious amounts of mechanical feedback to their surroundings (for a general review on massive star feedback see e.g. Geen et al. 2023).

Due to efficient internal mixing processes, these stellar winds become enriched in elements synthesized in the interior layers of the star (Langer 2012). This process plays an important role in

the chemical enrichment of the ISM, which in turn has a significant impact on the chemical evolution of the parent galaxy. The explosive nucleosynthesis in ccSNe yields elements heavier than iron, which also drives the chemical evolution and metallicity Z of the host galaxy (Smith 2014).

Empirically derived stellar parameters accompanied by evolutionary (Yoon et al. 2006; Brott et al. 2011) and population synthesis models (Leitherer et al. 1999; Stanway & Eldridge 2018) can be used to peer into the collective evolutionary paths of massive stars. Thus, bridging the gap between the empirical and theoretically predicted properties of massive stars (Vink et al. 2001; Krtička et al. 2021; Björklund et al. 2023) is a fundamental pillar for an overall better understanding of the galactic evolution on a cosmic timeline.

Blue supergiants are visually the brightest stars in external galaxies (Bresolin et al. 2001). They have successfully been used as extragalactic distance indicators and diagnostics of heavy-metal metallicities (Kudritzki et al. 2003; Urbaneja et al. 2005a; Przybilla et al. 2006; Kudritzki et al. 2024).

The principal motivation for the present study is to investigate the behaviour of the winds of late O and early B-supergiants in the LMC, more specifically in the temperature range associated with the "bi-stability jump". The term "bi-stability jump" describes a phenomenon of a steep "jump" in stellar wind density around $T_{\rm eff} \approx 25-21$ kK, which was first coined by Pauldrach & Puls (1990) from a spectroscopic analysis of P Cygni, where two solutions were possible. The first solution has a high temperature (the "hot" side of the jump) involved higher ionization levels which would produce a faster and relatively low density wind. The second solution had a lower temperature (the "cool" side of the jump), where the wind recombines to lower ionization stages, which results in a significant drop in the terminal velocity and a denser wind. Later, Lamers et al. (1995) observed a jump in the ratio $v_\infty/v_{\rm esc}$ from ≈ 2.6 for supergiants earlier than B1 (≈ 25 kK) to $v_\infty/v_{\rm esc} \approx 1.3$ for supergiants of types later than B1 (Kudritzki & Puls 2000). The reason for this jump is attributed to the recombination of Fe IV to Fe III as explained in Vink et al. (2000), since these lines dominate the acceleration in the subsonic part of the wind (Vink et al. 1999). Fe III has far more lines in the UV region close to the peak of the spectral energy distribution (SED) compared to Fe IV. Thus, more momentum is transmitted to the material and a much higher mass loss is produced.

Vink et al. (2001) provides a numerically derived, mass-loss prescription, where the temperature of the jump which divides the range into "cool" and "hot" depends on the Eddington parameter $\Gamma_{\rm e}$ and the metallicity. The introduction of the bi-stability jump could potentially increase the mass-loss rate by a factor of seven for the "cool" solution compared to the "hot" for stars that are located roughly around the bi-stability jump.

On the other hand, newer mass-loss prescriptions using a different approach to calculate the radiative acceleration, such as Björklund et al. (2021) and Krtička et al. (2021) do not predict such a steep increase in mass-loss rates. There have been multiple efforts to explore the behaviour of the wind of blue supergiants around the bi-stability jump in the Milky Way (Crowther et al. 2006; Benaglia et al. 2007; de Burgos et al. 2024a), the LMC (Verhamme et al. 2024), and the SMC (Bernini-Peron et al. 2024).

This investigation is facilitated by the advent of the Ultraviolet Legacy Library of Young Stars as Essential Standard (ULLYSES, Roman-Duval et al. 2025), to which 1000 orbits of *Hubble Space Telescope* (HST) were dedicated, making this the largest HST Director's Discretionary program ever conducted.

ULLYSES compiled an ultra-violet (UV) spectroscopic Legacy Atlas of about 250 OB-stars in low-Z regions, spanning the upper Hertzsprung-Russell diagram. The XShooting ULLYSES (XShootU) collaboration (Vink et al. 2023) also compiled a complementary optical spectral library of the same stars using the medium resolution spectrograph X-shooter (Vernet et al. 2011) mounted on the Very Large Telescope (VLT). This complimentary dataset is referred to as Xshooting ULLYSES (XshootU). =The ULLYSES and XShootU observations were not conducted simultaneously. Consequently, the impact of the time-dependent nature of stellar winds on non-photospheric spectral lines cannot be explored. Such an analysis can only be conducted with extensive time-series of optical and UV spectra (see e.g, Markova et al. 2005; Massa et al. 2024).

Although several studies investigate the properties of OB-supergiants in the Milky Way (MW, e.g., Herrero et al. 2002; Repolust et al. 2004; de Burgos et al. 2023), and the Magellanic Clouds (MCs, e.g., Crowther et al. 2002; Bestenlehner et al. 2020; Brands et al. 2022), using various analysis techniques, none of these studies had the unique ULLYSES/XshootU dataset. Unlike optical-only studies, the UV spectra of OB-supergiants provide a deeper insight into the properties of the wind, allowing the direct measurement of wind velocities and the breaking of the mass-loss rate-clumping degeneracy via saturated and unsaturated P Cygni profiles (Vink et al. 2023). This degeneracy has been extensively discussed in literature. Simply spoken, optical wind diagnostics such as Hα or He II λ4686 (in the case of O-supergiants) tend to overestimate the mass-loss rates if wind clumping is neglected (Puls et al. 2008). On the other hand, mass-loss rates that are estimated using only unsaturated P Cygni profiles tend to have very large uncertainties due to intrinsic wind-line variability (Massa et al. 2024) and are subject to degeneracies due to the presence of X-rays generated via shocks in the wind (Puls et al. 2008).

In Section 2, we present a detailed account of the observational data that was used in the study. In Section 3, we give a detailed description of the methods and techniques that were used in the analysis. In Section 4, we present our results, including the values of the physical and wind parameters that were obtained through our pipeline. In Section 5, we compare our results to previous empirical studies and numerical predictions and we discuss the implications of our findings on the bi-stability jump and the effect of metallicity on wind parameters. In Section 6, we summarize the interpretations of our results and discuss our plan for follow up studies.

2. Observations

2.1. Sample

We initially chose a sample of LMC supergiants in the spectral type range O7-B9, the classification of which was obtained from various sources and compiled in Vink et al. (2023). In Table 1, we provide the updated spectral type taken from Bestenlehner et al. (2025), in which the classification was determined using O-star templates from Sota et al. (2011) and B-star templates from Negueruela et al. (2024). In the revised classification, the luminosity class of Sk $-70°$ 16 (Fig. G.14) was changed from a low luminosity supergiant (Ib) to a bright giant (II). During this study, we had to exclude some objects due to signs of binarity or odd features in the morphology of optical wind-lines (Hα and He II λ4686) that could hint toward a circumstellar disks, leaving the sample with objects in the spectral range O9-B8, covering a wide temperature range that includes the bi-stability jump (the-
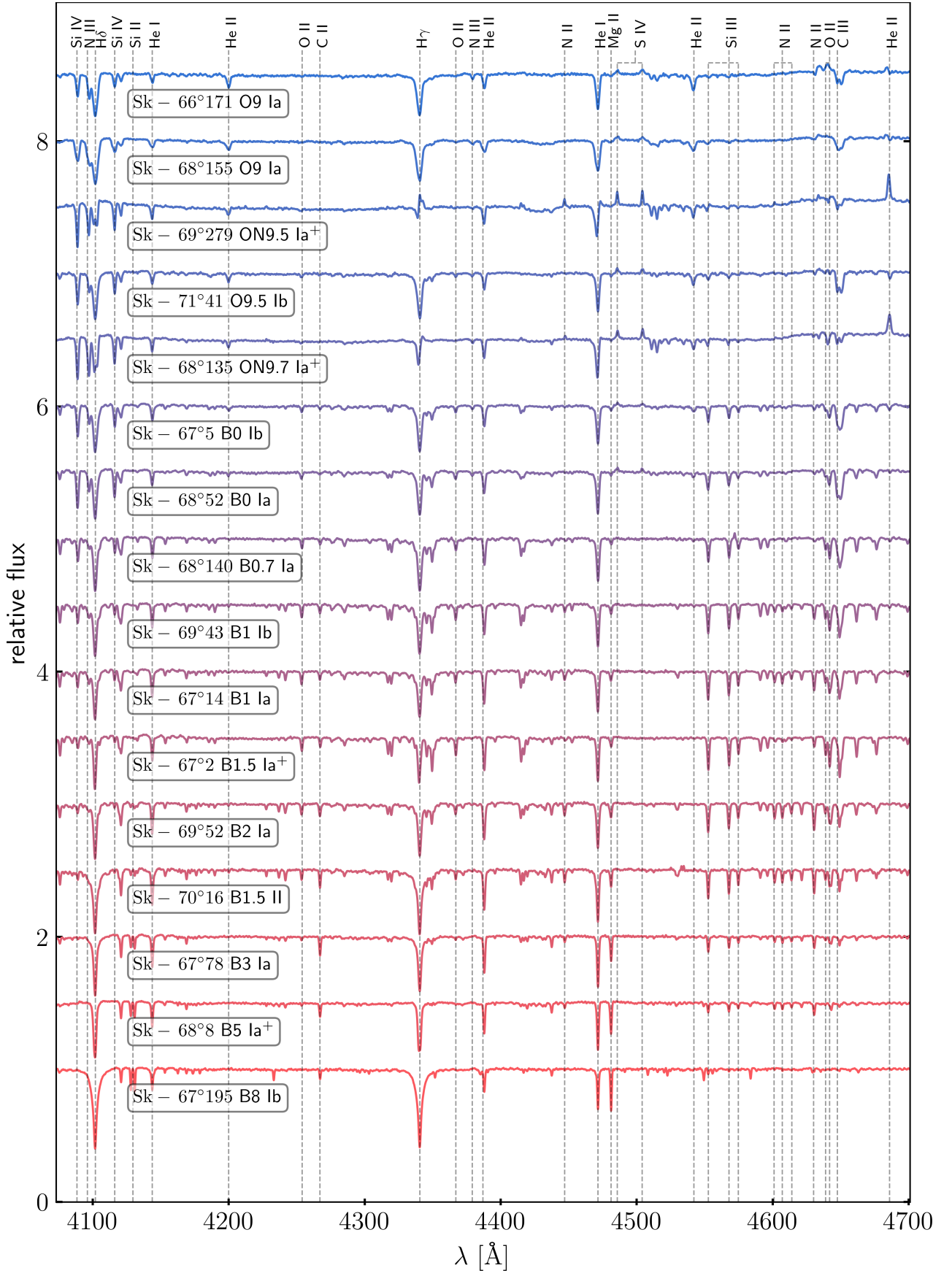
Fig. 1: Normalised XshootU spectra (Sana et al. 2024, DR1) in the blue optical range of the sample analysed in this work with identification for a subset of the optical lines used in the analysis. For illustration purposes an arbitrary offset of 0.5 for each spectrum was added. Fits to the violet, yellow, and red spectra for all stars are included in Appendix H.

oretically predicted to be around B1 spectral type). We briefly discuss the omitted objects in Appendix A.

2.2. UV data (ULLYSES)

The UV data used in this work is a subset of the *HST* ULLYSES sample (Roman-Duval et al. 2025), which obtained moderate-resolution spectra of OB-stars with selected wavelength settings of the Cosmic Origins Spectrograph (COS, Green et al. 2012) G130M/1291, G160M/1611 and G185M/1953 with resolutions $R \approx 12,000 - 16,000$, $R \approx 13,000 - 20,000$, and $R \approx 16,000 - 20,000$ respectively, and the Space Telescope Imaging Spectrograph (STIS, Woodgate et al. 1998) E140M/1425 ($R \approx 45,800$), and E230M/1978 ($R \approx 30,000$) gratings in the far- and near-UV during HST cycles 27 - 29. Those new spectra were combined with suitable existing spectra (previously obtained with *FUSE* and/or *HST*). Far Ultra-violet Spectroscopic Explorer (FUSE) spectra covers the wavelength $\approx 900 - 1160$Å through the $4'' \times 20''$ (MDRS) or $30'' \times 30''$ (LWRS) appertures, with a resolving power of $\approx 15,000$ (Moos et al. 2000).

2.3. Optical data (XShootU)

To complement the UV spectra, high quality optical/NIR spectroscopy was carried out with the X-shooter instrument (Vernet et al. 2011), which is mounted on the Very Large Telescope (VLT). This slit-fed ($11''$ slit length) spectrograph provides simultaneous coverage of the wavelength region between $3000 - 10200$ nm, across two arms; UVB ($300 \leq \lambda \leq 560$ nm), VIS ($560 \leq \lambda \leq 1000$ nm). X-shooter's wide wavelength coverage made it the instrument of choice to build an optical legacy data-set (Vink et al. 2023). The XshootU dataset was observed with the following settings: $0.8''$ slit width for the UBV arm achieving spectra resolution $R \approx 6700$, and $0.7''$ for the VIS arm ($R \approx 11400$). Fig. 1 show the optical spectra used in this work, which were combined, flux calibrated, corrected for Telluric contamination and normalised by Sana et al. (2024, DR).

2.4. Auxiliary data (MIKE)

Another complimentary spectroscopic optical dataset was collected using the Magellan Inamori Kyocera Echelle (MIKE) spectrograph which is mounted on the Magellan Clay Telescope, for known slow rotating ULLYSES stars. The higher spectral resolution ($R \approx 35000 - 40000$) and the wide wavelength coverage ($3350 - 5000$Å blue arm) and ($4900 - 9500$Å red arm) is needed to resolve spectral features and determine their rotation rates using metal lines (Crowther 2024). Four of the stars in our analysed sample are also included in the Magellan/MIKE sample Sk $-67°$ 78, Sk $-70°$ 16, Sk $-68°$ 8, and Sk $-67°$ 195.

2.5. Photometry

The photometric magnitudes utilised in the SED fitting to obtain the bolometric luminosities of the targets were taken from various sources and compiled in Vink et al. (2023). The *UBV* photometry are drawn from Ardeberg et al. (1972); Schmidt-Kaler et al. (1999); Massey (2002).

The infrared JK_S photometry are preferably taken from the *VISTA near-infrared YJK_S survey of the Magellanic System* (VMC, Cioni et al. 2011), with *H*-band photometry taken from the *Two Micron All Sky Survey* (2MASS, Cutri et al. 2003; Skrutskie et al. 2006). For very bright sources that are saturated in

VMC (Cioni et al. 2011) we use the *J* and K_S photometry provided in 2MASS (Skrutskie et al. 2006).

2.6. UV normalization

The UV spectra require normalization, which is challenging due to the iron forest that heavily contaminates the continuum. Fig. 2 shows normalised UV spectra of a subset of our sample. The quality of the fits to the UV lines is highly dependent on the quality of the normalization of the observed spectrum. On average, we obtained very good normalised UV and far UV spectra for the targets by using the SED fitting explained later in Section 3.4.3 to obtain the bolometric luminosities of the targets. In essence, we apply the extinction from Gordon et al. (2003) to the normalised synthetic spectrum of the best-fitting model and scale it to the flux levels of the observed spectrum using the K_S magnitude, then simply divide the observed spectrum by the extinct and scaled continuum of the model to obtain a normalised spectrum with relative flux values.

3. Method

Line blanketed, plane parallel model atmospheres such as TLUSTY (non-LTE, Hubeny & Lanz 1995a) and ATLAS (LTE, Kurucz 1979) coupled to SURFACE/DETAIL (Butler & Giddings 1985) have been widely applied to early-type stars with weak winds, to derive physical parameters and accurate elemental abundances (e.g., Przybilla et al. 2006; Hunter et al. 2007; Przybilla et al. 2008). This combined non-LTE method has been also been recently employed in studies of B-supergiants (e.g., Weßmayer et al. 2022, 2023). For stars with strong stellar winds, it is necessary to employ line blanketed model atmospheres with spherical geometry. Examples include FASTWIND (Puls et al. 2005; Rivero González et al. 2012), PoWR (Gräfener et al. 2002a; Hamann & Gräfener 2003a) and CMFGEN (Hillier 1990; Hillier & Miller 1998). These codes have the advantage of incorporating stellar winds, albeit at the expense of computational resources, such that the determination of physical parameters and elemental abundances are more costly than the plane parallel case.

3.1. Model atmosphere code and grid

In this work, we use CMFGEN (Hillier 1990; Hillier & Miller 1998) which solves the radiative transfer equations in a 1-D non-LTE, spherical geometry with a radial outflow of material (that can also be optically thick in the continuum) in the co-moving frame. We choose to utilise CMFGEN because it accounts for the influence of extreme UV line blanketing on the wind populations and ionization structure, due to thousands of overlapping lines. It does that with a detailed treatment using "super-levels" which was pioneered by Anderson (1985, 1989), in which several levels with similar energies and properties are treated as a single or super level. The idea of super-levels is of tremendous importance for the iron-group elements. An individual ionization stage can have hundreds of levels and line transitions (cf. the iron forest in Fig. 2) that need to be considered in the full model atom, but applying the super-levels method reduces significantly the number of statistical equilibrium equations to be considered in the NLTE treatment. There is also a time-dependent variant of CMFGEN for the simulation of supernovae spectra (e.g., Dessart & Hillier 2010), but the scheme we employ in this work assumes stationary outflows.
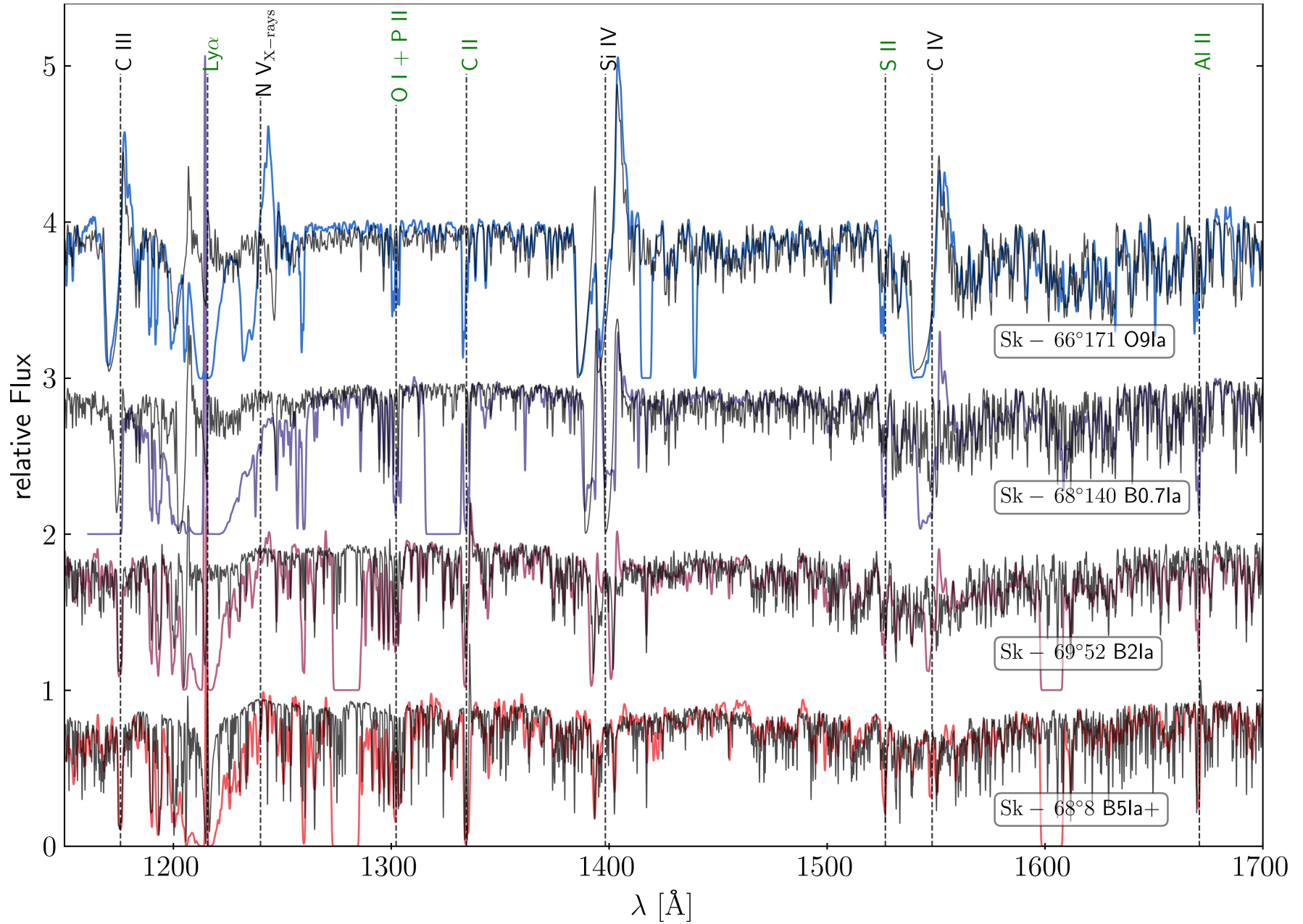
Fig. 2: Normalised UV spectra in the range of the sample analysed in this work with line identification for the UV lines used in the analysis. For illustration purposes an offset of 1 was added. Coloured lines: observations. Black lines: model fits for each of the respective stars. Stellar features are indicated in black line labels, whereas green line labels indicate interstellar features. The HST gap at ≈ 1300 in the spectra of Sk 69° 52, Sk 68° 8 is due to appending observations from COS G130M and COS G160M. The gap at 1600 Å is due to appending observations from COS G160M and COS G185M. Other UV fits are compiled in Appendix H

Table 1: List of the targets in our sample. The last three columns are the wavelengths (in Å) of the UV ranges and the corresponding instruments that were used for observations. The literature spectral types are adopted from Vink et al. (2023). The revised classifications are adopted from Bestenlehner et al. (2025).

| Sk −	HDE	SpT (revised)	SpT (literature)	(900 − 1160)	(1150 − 1700)	(1700 − 2370)
66° 171	269889	O9 Ia	O9 Ia	FUSE	STIS E140M	STIS E230M
68° 155	-	O9 Ia	B0.5 I	FUSE	COS G130M+G160M	STIS E230M
69° 279	-	ON9.5 Ia$^+$	O9.2 Iaf	FUSE	STIS E140M	STIS E230M
71° 41	-	O9.5 Ib	O9.7 Iab	FUSE	STIS E140M	-
68° 135	-	ON9.7 Ia$^+$	ON9.7 Ia$^+$	FUSE	STIS E140M	STIS E230M
67° 5	268605	B0 Ib	O9.7 Ib	FUSE	STIS E140M	STIS E230M
68° 52	269050	B0 Ia	B0 Ia	FUSE	STIS E140M	STIS E230M
69° 43	268809	B1 Ib	B0.5 Ia	FUSE	STIS E140M	STIS E230M
68° 140	-	B0.7 Ia	B0.7 Iab	FUSE	COS G130M+G160M	STIS E230M
67° 2	270754	B1.5 Ia$^+$	B1 Ia$^+$	FUSE	STIS E140M	STIS E230M
67° 14,	268685	B1 Ib	B1.5 Ia	FUSE	COS G130M+G160M	STIS E230M
69° 52,	268867	B2 Ia	B2 Ia	FUSE	COS G130M+G160M	STIS E230M
67° 78,	269371	B3 Ia	B3 Ia	FUSE	COS G130M+G160M	STIS E230M
70° 16	-	B1.5 II	B4 I	-	COS G130M+G160M	COS G185M
68° 8	268729	B5 Ia$^+$	B5 Ia$^+$	-	COS G130M+G160M	STIS E230M
67° 195	-	B8 Ib	B6 I	-	COS G130M+G160M	STIS E230M
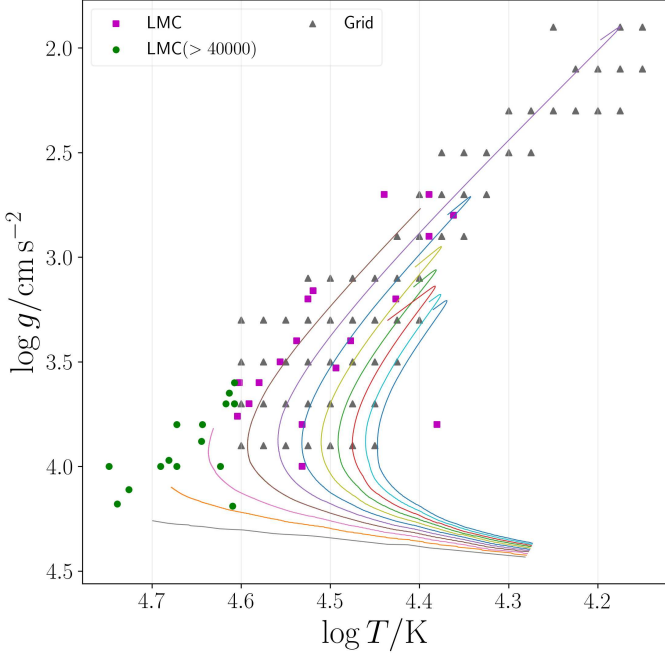
Fig. 3: Grey triangles: model grid, purple squares: LMC targets with temperatures ≤ 40 kK (from literature), green points: LMC targets with temperatures ≥ 40 kK. The overlaid lines are isochrones taken from Brott et al. (2011).

For the initial setup of the (quasi-)hydrostatic layers, a previous CMFGEN model can be used. CMFGEN does not calculate the velocity field stratification with the radiative acceleration. Instead, the density (velocity) structure of the extended atmosphere is set through the continuity equation by a parametrized velocity law $v(r)$ on top of a solution of the hydrostatic equation from a connection velocity to the inner photosphere (e.g., Martins et al. 2012).

In CMFGEN, clumping is treated in the "optically-thin clumping" approximation, also known as "micro-clumping", assuming a void inter-clump medium and a volume filling factor f_{vol}. To solve the radiative transfer equation with the micro-clumping assumption, the size of the clumps is assumed to be

smaller than the mean free path of the photons (Hillier 1996). The treatment of wind inhomogeneities in CMFGEN has been extensively discussed in the literature (Hillier 1997; Hillier & Miller 1998, 1999). In the grid, we adopt a a velocity-dependent clumping law that was introduced for O-stars in Hillier et al. (2003):

$$f(r) = f_{vol,\infty} + (1 - f_{vol,\infty}) \exp\left(-\frac{v(r)}{v_{cl}}\right), \quad (1)$$

where $f_{vol,\infty}$ is the terminal volume-filling factor, v_{cl} is the onset clumping velocity, and $v(r)$ is the velocity of the wind at a given radius r. In its essence, $f_{vol,\infty}$ determines the degree of clumping in the wind, where smaller values of $f_{vol,\infty}$ indicate a more highly clumped wind at $r \to \infty$. v_{cl} determines the location (depth) at which clumping starts. This means that Equation 1, describes winds that become more smooth as $v(r)$ becomes lower approaching the photosphere, and become rapidly more clumped at larger radii. In our grid, we fix $f_{vol,\infty}$ to a value of 0.1. Later in the fine-tuning procedure, $f_{vol,\infty}$ is treated as a free parameter. This is essential for obtaining satisfactory fits for the electron scattering wings of Hα and unsaturated P Cygni resonance lines.

Fig. 3 shows a slice of the grid in T_{eff}-$\log g$ space. We fixed the luminosity in our models to $\log(L/L_\odot) = 5.8$ and varied $\log(T_{eff}/K)$ in the range $\approx [4.15, 4.60]$ and $\log(g/cm\,s^{-2})$ in the range $\approx [1.7, 3.9]$ depending on the temperature, in steps of 0.025 dex for $\log(T_{eff}/K)$ and 0.2 dex for $\log(g/cm\,s^{-2})$. We employed the empirical temperature and metallicity dependent terminal wind velocity recipe from Hawcroft et al. (2024):

$$v_\infty\,(km\,s^{-1}) = [0.092(\pm0.003)T_{eff}\,(K) - 1040(\pm100)]\,Z/Z_\odot^{(0.22\pm0.03)}, \quad (2)$$

where $Z \approx 0.43Z_\odot$ for the LMC (Choudhury et al. 2016). In Hawcroft et al. (2024), Sobolev with Exact Integration (SEI) modelling was employed to measure the terminal wind velocities for objects no later than B1.5 spectral types, using the C IV $\lambda\lambda1548 - 1551$ resonance doublet, with radial velocities adopted from the UV.

In our grid, we utilised a modified β velocity law that was introduced in Hillier et al. (2003):

$$v(r) = v_0 + (v_\infty - v_0)\left(1 - \frac{R_*}{r}\right)^\beta, \quad (3)$$

Table 2: Metal abundances ($\epsilon_X = \log X/H + 12$ by number) adopted in the model grid. Baseline LMC abundances ϵ_X^{LMC} are drawn from the compilation of Vink et al. (2023). $\Delta\epsilon_X$ represents the difference between the LMC baseline values and the values adopted in our grid.

Element	ϵ_X^{LMC}	$\Delta\epsilon_X$	Reference
C	7.03	−0.52	(Hunter et al. 2008)
N	8.01	+0.47	(Hunter et al. 2008)
O	8.40	−0.07	(Hunter et al. 2008)
Ne	7.70	-	-
Mg	7.13	-	-
Al	6.20	-	-
Si	7.06	-	-
P	5.11	-	-
S	6.88	-	-
Ca	6.10	-	-
Fe	7.23	-	-
Ni	5.90	-	-

where v_∞ is the terminal wind velocity, v_0 is the connection velocity, which is estimated as two thirds the speed of sound ≈ 10 km s^{-1}, and $R_{\tau=100}$ is the radius of the star, which is defined at optical depth $\tau = 100$. For our grid we adopt adopt a fixed value of $\beta = 1$. This procedure yielded a 2-D grid in the temperature-gravity parameter space (grid$_{base}$).

In Table 2, we present the values of metal abundances $\log X/H + 12$ (by number) adopted in the model grid. Henceforth, we substitute $\log X/H + 12$ with the notation ϵ_X. Rather than adopting baseline LMC CNO abundance values for metals such as the one compiled in Vink et al. (2023), we chose to adopt processed abundances correlating to low luminosity B-stars in the LMC from Hunter et al. (2008), that show nitrogen enhancement of $\Delta\epsilon_N \approx +0.47$ dex, compared to the LMC baseline in Vink et al. (2023), and at the expense of carbon and oxygen deficiencies of $\Delta\epsilon_C \approx -0.5$ dex and $\Delta\epsilon_O \approx -0.07$ dex. Since Hunter et al. (2008) excludes B-supergiants, we checked the validity of these values for luminous B-supergiants (which might be expected to show the greatest N enhancements) by resorting to the work of McEvoy et al. (2015), in which TLUSTY non-LTE model atmosphere calculations have been used to determine atmospheric parameters and nitrogen abundances for 34 single and 18 binary supergiants. Their analysis shows a nitrogen enrichment value of ≈ 0.5 dex relative to Vink et al. (2023), which is very close to our grid's nitrogen abundance. For other key elements in our grid like silicon, magnesium, and iron, we implemented baseline LMC abundances from Vink et al. (2023). Abundances of metals heavier than oxygen are not modified during the fitting procedure.

Lastly, we covered the temperature-gravity-wind density parameter space. We did that by iterating over the mass-loss rates $\log(\dot{M}/M_\odot$ yr$^{-1})$ in the range $\approx [-5.5, -7.3]$ in steps of 0.3 dex for each of the points from grid$_{base}$. The final grid is a 3-D grid in the temperature-gravity-wind density space.

Since the strength of emission features scales not only with the mass-loss rate but also with the volume-filling factor (f_{vol}), terminal velocity, and radius of the star, it is convenient to compress these parameters into one parameter when compartmentalizing the model grids. To spectroscopically quantify mass-loss rates of hot massive stars using scaling relations, we chose to adopt the transformed radius (Schmutz et al. 1989) originally used for optically thick winds of Wolf-Rayet stars (WR), where

the line equivalent width is preserved:

$$R_t = R_* \left[\frac{v_\infty}{2500 \text{ km s}^{-1}} \middle/ \frac{\dot{M}}{10^{-4} \ M_\odot \text{yr}^{-1} \ \sqrt{f_{vol}}} \right]^{2/3}, \qquad (4)$$

The grid covers a wide range of $\log R_t$ from 1.6 to 3.1, with lower values relating to denser winds. This $\log R_t$ range corresponds to an optical depth-invariant wind-strength parameter $\log Q = \log \dot{M}/(R_* v_\infty)^{3/2}$ (Puls et al. 1996) range of −13.9 to −11.5, where larger values of $\log Q$ correspond to denser winds. We employ R_t to scale $\dot{M}$ to the derived bolometric luminosity of the star.

3.2. Atomic data and X-rays

In our models we include 14 species and 50 different ions. We exclude higher ionization stages for the cooler (< 25 kK) models and include the lower ionization stages. This is of special importance to the iron lines which dominate the UV in the B-star regime. We include our detailed underlying model atom structure in the appendix in Table D.1.

X-rays can be included in CMFGEN using X-ray emissivities from collisional plasma models (Smith et al. 2001), where the source of this emission is assumed to be shocks forming in the winds (Pauldrach et al. 1994). The detailed approach used in CMFGEN is described in Hillier & Miller (1998). The general spectral appearance is not affected by X-rays, although the highest ionization UV lines can be enhanced at the expense of lower ionization lines (Baum et al. 1992) at relatively low stellar temperatures due to Auger processes. We elect to exclude X-rays from our analysis, because the ad hoc addition of X-rays in CMFGEN does not provide phenomenological description of the physical shock parameters and reduces the number of unconstrained parameters in the fitting procedure.

The main drawbacks of excluding X-rays in our models is that, in some cases, it is difficult to obtain satisfactory fits for high ionization UV P Cygni lines. This could potentially lead to over estimating the mass-loss rates. Bernini-Peron et al. (2023), who included X-rays in their CMFGEN models, found that their mass-loss rates for Galactic B-supergiants are lower by a factor of two compared to the mass-loss rates obtained by Crowther et al. (2006) and Searle et al. (2008), who exclude X-rays. In Fig. 2, the discrepancy between the predicted and observed P Cygni N v $\lambda\lambda 1238 - 1242$ line in Sk −66° 171 is due to the lack of X-rays in the model. This is also the case for the P Cygni C iv $\lambda\lambda 1548 - 1551$ profile in Sk −68° 140 and Sk −69° 52.

3.3. Summary of the fitting procedure

Since CMFGEN is time and resource-intensive, we are limited by a small number of models relative to the number of parameters that we have to extract from the stellar spectra. Therefore, as a first-order approximation (initial pinpoint), we use the results of the analysis done using the pipeline that was introduced in Bestenlehner et al. (2024), which is a grid-based χ^2- minimization algorithm, that utilises the entire optical spectrum rather than selected diagnostic lines allowing a wider range of temperature from B to early O-stars to be analysed. This grid of synthetic spectra was computed with the non-LTE stellar atmosphere and radiative transfer code FASTWIND (Puls et al. 2005), which is efficient and quick but lacks a detailed treatment of the iron forest in the UV range. This pipeline provides a first approximation of T_{eff}, $\log g$, $v_{rot} \sin i$ using only the optical XShootU data, which we then can refine using the UV range provided by our

CMFGEN grid, and then produce a fine-tuned model for the entire spectrum based on the best fitting grid model. To summarize, our entire procedure consists of the following steps:

- 1st step: Approximation of T_{eff} and $\log g$ from the optical spectrum using the model de-idealization pipeline introduced in Bestenlehner et al. (2024), which we use to pinpoint the closest fitting model from the grid in T_{eff}-$\log g$-$\dot{M}$ parameter space.
- 2nd step: Fine-tune the values of T_{eff}, $\log g$, v_∞ and the helium abundance of the model from the previous step.
- 3rd step: Fine-tune wind parameters $\dot{M}$, β-law, f_{vol} and clumping on-set velocity v_{cl}.
- 4th step: Refine CNO- surface abundances.

The second, third and fourth steps take on average ten tailored models in total to obtain a satisfactory fit.

3.4. Diagnostics

Underlying systematic errors arise from our grid and fitting procedure. The most notable are the inclusion of a limited number of species and ions, fixing certain parameters like the micro- and macro-turbulent velocities, and fixing the abundances of elements heavier than oxygen. An important part of our analysis is wind clumping, which can vary greatly depending on the treatment utilised in the model (e.g., Brands et al. 2022). Finally, the finite spectral resolution of the observation adds another layer of uncertainty to the overall analysis. We estimate the model uncertainties (parameters with superscript notation 'm') the derived physical parameters and wind properties. By 'model uncertainty' we simply mean the smallest variation in a given input parameter that would produce a noticeable change in the quality of the fit.

3.4.1. Effective temperature and helium abundance

After we derived a rough estimate of the stellar and wind parameters from our grid, we start fine-tuning the model parameters to reproduce the observed spectrum. In order to do that, we first vary the temperature, which has a large impact on the morphology of the spectrum for different spectral classes. Consequently, obtaining an accurate temperature determines the overall quality of the fit and of the other estimated stellar and wind parameters. In our fitting procedure, T_{eff} is derived using the ionization balance of helium (He) and silicon (Si). In practice, lines from successive ions, of the same elements must be observed.

The most reliable lines for O-stars are He II and He I, and historically He II $\lambda4542$ and He I $\lambda4471$ have been used (Martins 2011), which is what we used for the O-stars in our sample as primary diagnostics. Additionally we use He II $\lambda5411$ and He I $\lambda4922$ as a sanity check

For B-stars the main diagnostic is the silicon ionization balance (McErlean et al. 1999; Trundle et al. 2004; Trundle & Lennon 2005). For the earliest B-stars (B0 - B2) spanning a temperature range $T_{eff} \approx 28-21$ kK we use Si IV $\lambda\lambda4089 - 4116$ [1] and Si III $\lambda\lambda\lambda4553 - 4568 - 4575$ as our main diagnostics. For mid B-stars (B3-B5) in the temperature range $T_{eff} \approx 20-14$ kK

---

[1] The Si IV absorption line at $\lambda = 4089$ Å is actually a blend of Si IV and O II (de Burgos et al. 2024b). Considering models with extended O II atomic levels, we find that the O II component contributes $\approx 9\%$, 10%, 62% to the equivalent width of the combined line at $T_{eff} = 30$, 25, 20 kK, respectively, with both lines being very weak in the low T_{eff} case
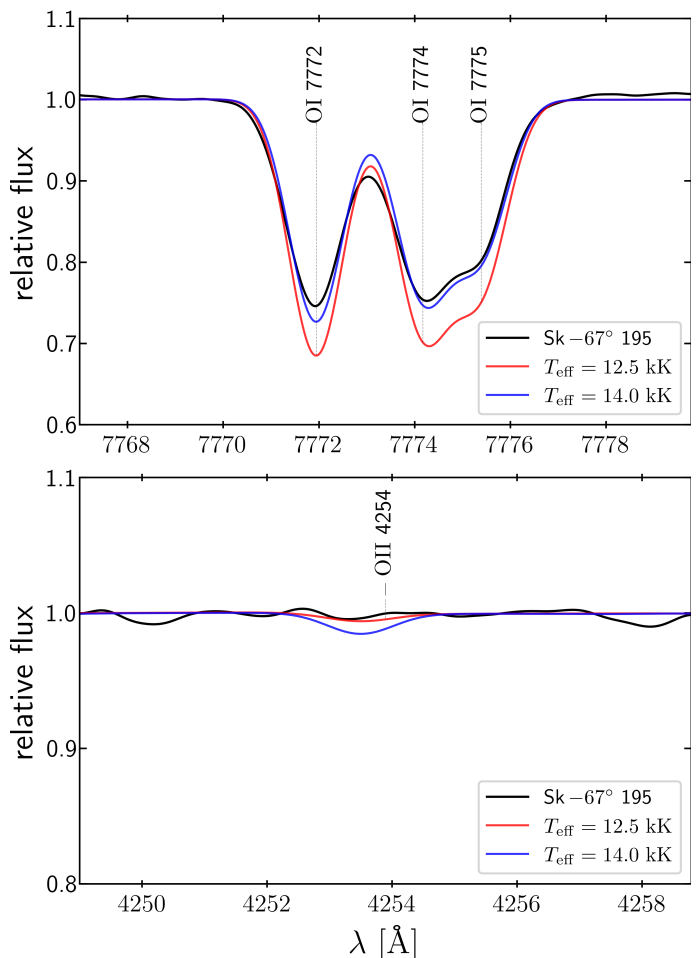
Fig. 4: O I $\lambda\lambda\lambda7772 - 7774 - 7775$ and O II $\lambda4254$ lines of the B8 supergiant Sk $-67°$ 195 (black line). Red line: the preferred model the temperature of which ($T_{eff} = 12.5$ kK) was obtained from fitting He I $\lambda4471$ and Mg II $\lambda4481$, and a comparison with higher $T_{eff} = 14.0$ kK.

Si III $\lambda\lambda\lambda4553 - 4568 - 4575$ and Si II $\lambda\lambda4128 - 4131$ are used. For late B-stars (B6-B8) we resort to fitting He I $\lambda4471$ and Mg II $\lambda4481$, which is not as reliable as fitting consecutive ions of the same species.

An alternative indicator of T_{eff} in late B-stars is the ratio of O II to O I line. By way of example, in Fig. 4 we show the triplet O I $\lambda\lambda\lambda7772 - 7774 - 7775$ (upper panel) and O II $\lambda4254$ (lower panel). The preferred model (red solid line) for the B8 supergiant Sk $-67°$ 195, the temperature of which was obtained from fitting He I $\lambda4471$ and Mg II $\lambda4481$, reproduces the O I $\lambda\lambda\lambda7772-7774-7775$ and O II $\lambda4254$ lines relatively well. For comparison, we display another model that differs from the preferred model only in its temperature with $\Delta T_{eff} = 1500$ K (blue solid line). We select this model as it is the nearest model on the grid to our preferred model in the temperature parameter-space that presents O II lines. This fit implies that decreasing the oxygen abundance in the comparison model could produce a better match to both lines. This could be used either as a primary diagnostic for T_{eff} or as a sanity check in late B-supergiants.

By way of a sanity check, we have compared the predicted Balmer jump strengths to observations (Kudritzki et al. 2008; Urbaneja et al. 2017). We find that, for the most part, the strength of the predicted Balmer jumps – the T_{eff} of which was obtained from line diagnostics – are in good agreement with observations.

Nevertheless, a few hundred K higher temperatures produce a better match for a subset of mid to late B-supergiants, albeit within the quoted uncertainties.

The earliest B-stars (B0-B0.7) in the temperature range $T_{\rm eff} \approx 25-22$ kK show weak He II lines, so we use He I $\lambda4471$ and He II $\lambda4542$ as a sanity check when fine-tuning the temperature for such objects. There is also a temperature range $T_{\rm eff} \approx 20-17$ kK at which silicon lines of all three ionization stages (Si IV, Si III, and Si II) are present. In those cases, we attempted to fit all lines but focused mainly on the stronger consecutive pair.

Since silicon is an alpha-process element, its abundance is primarily determined by the environment, so is not heavily influenced by the evolution of the star in the supergiant phase. Also, Korn et al. (2005) obtains a value of $\epsilon_{\rm Si} = 7.07 \pm 0.3$ from fast rotating B-stars in the LMC, and Hunter et al. (2007) finds a silicon abundance $\epsilon_{\rm Si} = 7.19 \pm 0.07$ from narrow-lined late O and B-stars in the LMC, whereas Dopita et al. (2019) derives a value $\epsilon_{\rm Si} = 7.11 \pm 0.04$ from supernova remnants in the LMC. The low variance between those values is what led us to fixing the silicon abundance. For those reasons, we did not attempt to fit the silicon lines' strength by changing the abundance of silicon at the fine tuning stage. We also do not change the abundance of magnesium during our fine tuning stage. Similar to silicon, this is motivated by the low variance between the magnesium abundance values obtained via different methods in the literature. $\epsilon_{\rm Mg}$ values from the literature are as follows: $\epsilon_{\rm Mg} = 7.15 \pm 0.3$ from Korn et al. (2005), and $\epsilon_{\rm Mg} = 7.06 \pm 0.09$ from Hunter et al. (2007), and $\epsilon_{\rm Mg} = 7.19 \pm 0.09$ from Dopita et al. (2019)

For O-stars, the helium abundance is essential for an accurate temperature estimate. Changing the helium abundance at the expense of hydrogen modifies the ionization structure in the atmosphere which, in turn, affects the shape and strength of Hα especially when it is in emission. This is the case for the majority of the targets in our sample. Hence it is important to also obtain an accurate helium abundance for both O-stars and B-stars. In our fitting procedure, as we are fitting temperature line diagnostics, we simultaneously fine-tune abundances of helium and hydrogen before attempting to fit wind lines such as Hα.

It is important to understand that varying $T_{\rm eff}$ by small amounts can have a different effect on the quality of the fit depending on the temperature range of the model. To illustrate this, we show in Fig. 5 the effect of varying the temperature of the best fitting model (red solid line) by $\Delta T_{\rm eff} = -700$ K with all other parameters fixed. The top panels shows the fits to He II $\lambda4542$ and He I $\lambda4471$ (panels a and b respectively in Fig. 5) for the O9.5 Ib supergiant Sk $-71°$ 41 (Fig. G.4), where the best fitting model has a $T_{\rm eff} = 29.2$ kK and we can see that while the model with lower temperature does not yield a noticeably different fit for He I $\lambda4471$, He II $\lambda4542$ is significantly changed. The equivalent widths (EW) ratio of He I $\lambda4471$ to He II $\lambda4542$ in the observations is $\approx 3.20 \pm 0.05$. our preferred model yield an EW ratio of $\approx 3.15 \pm 0.05$ compared to an EW ratio $\approx 3.45 \pm 0.05$ for the comparison model with the higher $T_{\rm eff}$.

Panels c and d in Fig. 5 show the comparison of the fits of Si IV $\lambda\lambda4088 - 4116$ and Si III $\lambda\lambda\lambda4553 - 4568 - 4575$, respectively, for the B0 Ia supergiant Sk $-68°$ 52 (best fitting model $T_{\rm eff} = 26.0$ kK). In this case lowering the temperature by $\Delta T_{\rm eff} = 700$ K slightly worsens the quality of the fits for both sets of lines. The EW ratio of Si III $\lambda4552$ to Si IV $\lambda4088$ in the observed spectrum of Sk $-68°$ 52 is $\approx 0.55 \pm 0.05$. Our preferred model yields an EW ratio of $\approx 0.51 \pm 0.05$ compared to an EW ratio of 0.45 ± 0.05 for the comparison model with the lower $T_{\rm eff}$.
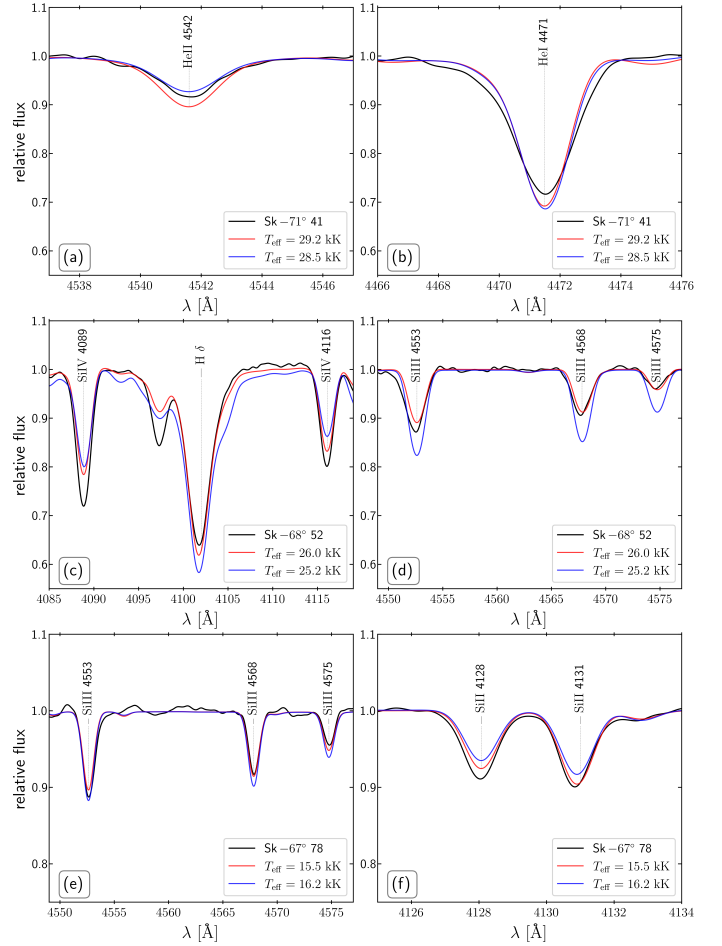

Fig. 5: Examples of the effect of varying $T_{\rm eff}$ on the quality of the fit. Best fitting model: red solid line. Comparison model: blue solid line ($\Delta T_{\rm eff} = 700$ kK). Observed XShootU spectrum: black solid line. a-b: Sk $-71°$ 41 (O9.5 Ib). c-d: Sk $-68°$ 52 (B0 Ia). e-f: Sk $-67°$ 78 (B3 Ia).

In panels e and f of Fig. 5, we show the fits of the B3 Ia supergiant Sk $-67°$ 78 for Si III $\lambda\lambda\lambda4553 - 4568 - 4575$ and Si II $\lambda\lambda4128 - 4131$, respectively, where the best fitting model has $T_{\rm eff} = 15.5$ kK. We can see that raising the temperature of the model by $\Delta T_{\rm eff} = 700$ K noticeably deteriorates the quality of the fit. The EW ratio of Si II $\lambda4128$ to Si IV $\lambda4552$ in the observed spectrum of Sk $-67°$ 78 is $\approx 0.60 \pm 0.05$. Our preferred model yields an EW ratio of $\approx 0.62 \pm 0.05$ compared to an EW ratio 0.53 ± 0.05 for the comparison model with the higher $T_{\rm eff}$.

We estimate the model uncertainty from the spectral fitting as $\Delta T_{\rm eff}^m \approx \pm 500 - 1000$ K depending on the quality of the fit, and we estimate a more conservative and realistic uncertainty as double the model uncertainty in attempt to take into account limitations of the model atmosphere code, giving us $\Delta T_{\rm eff} \approx \pm 1000 - 2000$ K.

3.4.2. Effective surface gravity

The surface gravity ($\log g$) is obtained via fitting the wings of Balmer lines. Balmer lines are broadened by collisional processes and are most sensitive to Stark broadening (linear Stark broadening affects the wings of the H and, to a lesser extent, He II lines; indeed, this effect is mainly used to constrain the surface gravity), which is related to gas pressure, and in turn, gas pres-
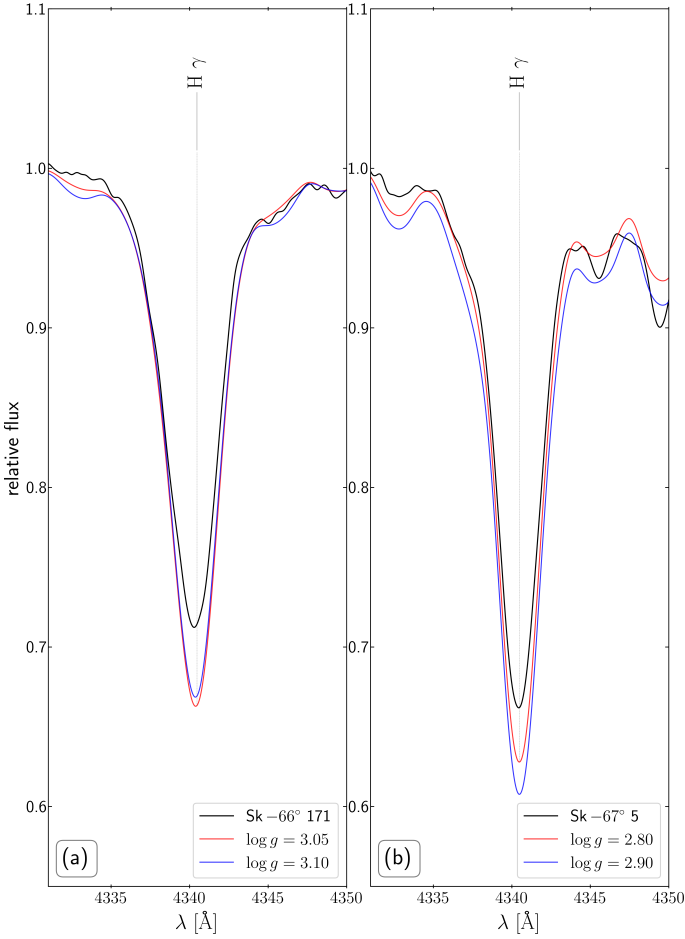
Fig. 6: Examples of the effect of varying $\log g$ on the quality of the fit. Best fitting model: red solid line. Comparison model: blue solid line. Observed XShootU spectrum: black solid line. a: Sk −66° 171 (O9 Ia) ($\Delta \log g = 0.05$). b: Sk −67° 5 (B0 Ib) ($\Delta \log g = 0.1$).

sure is intimately connected to electron pressure ($P_e = N_e KT$) in hot stars. This means that Balmer lines are broader in higher gravity stars. Degeneracies that occur when fitting Balmer lines are alleviated once temperature diagnostic lines are included (fitting $\log g$ and $T_{\rm eff}$ simultaneously and iteratively).

We use Hγ as the main indicator since it is usually in absorption and its wings are mostly not contaminated by wind emission or by blending with other lines. Hη and Hζ are used as a sanity check. These Balmer lines are usually strong and well resolved (Simón-Díaz 2020; Martins 2011), but in the case of the O hypergiants Sk −68° 135 and Sk −69° 279 we resorted to fitting Hη as our primary surface gravity diagnostic due to wind contamination in all the lower Balmer lines.

To show the level of sensitivity of the model to modest changes in $\log g$, we present two cases of fitting Hγ. For the O9 Ia supergiant Sk −66° 171 (panel (a) in Fig. 6), the best fitting model (red solid line) was computed with $\log (g/\mathrm{cm\,s^{-2}}) = 3.05$ dex and the comparison model (blue solid line) with $\log (g/\mathrm{cm\,s^{-2}}) = 3.10$ dex. Both models were computed with the same $T_{\rm eff} = 29.9$ kK and with all other parameters kept the same, and as shown the two fits are very similar. The second case (panel (b) in Fig. 6) is for the B0 Ib supergiant Sk −67° 5, where the best fitting model and the comparison model were

Table 3: Properties of the PYPHOT filter functions (Fouesneau 2025) employed in this study.

filter	$\lambda_{central}$	$\lambda_{\rm pivot}$	$\lambda_{\rm effective}$	Vega
	Å	Å	Å	
B	4347.526	4296.702	4316.312	20.512
V	5504.666	5469.853	5438.689	21.099
K_S	21655.864	21638.169	21521.413	25.921

computed for $\log (g/\mathrm{cm\,s^{-2}}) = 2.8$ dex and 2.9, respectively, and the same $T_{\rm eff} = 25.6$ kK. In contrast to the previous case, a $\Delta \log (g/\mathrm{cm\,s^{-2}}) = 0.1$ dex dramatically changes the quality of the fit.

We estimate the model uncertainty at $\Delta \log g^m = \pm 0.05 - 0.10$ dex and adopt a conservative uncertainty $\Delta \log g_c = \pm 0.2 - 0.25$ dex which takes into account the additional uncertainty of $v_{\rm rot} \sin i$ and R_* and the quality of the normalization (a 1% change in the wings due to normalization can lead to a $\log g$ difference of 0.1 dex).

3.4.3. Luminosity

For the determination of the bolometric luminosities $L_{\rm bol}$ of our stars, we use the flux from the model computations, which was computed for a fixed luminosity of $\log (L_{\rm model}/L_\odot) = 5.8$. We select Vega magnitude systems photometric zero-point. First, we apply suitable filter functions from PYPHOT (Fouesneau 2025) using the effective wavelengths of the filters and we obtain the BVK_S fluxes of the model using the function get_flux, and from the fluxes we calculate magnitudes of the model ($B^{\rm m}$, $V^{\rm m}$ and $K_S^{\rm m}$) as $-2.5 \log F_{BVK_S} - m_{BVK_S}^{\rm vega}$. The filter function properties and Vega magnitudes are presented in Table 3. We then apply the extinction law from Gordon et al. (2003) and fit the relative extinction R_V and other parameters that determine the shape of the UV extinction curve (Fitzpatrick & Massa 1990) to match the shape of the observed SED. The model SED is then scaled to the observed SED using a factor equal to $K_S^{\rm m}/K_S$. Using the model magnitudes, the color excess $E(B-V)$ is calculated as $(B-V) - (B^{\rm m} - V^{\rm m})$. Assuming the distance modulus DM for the LMC is 18.50 ± 0.02 mag (Alves 2004), we calculate the bolometric correction of the visual magnitude of the model $BC_V^{\rm m}$ with the equation $BC_V^{\rm m} = -2.5 \log L_{\rm model} + 4.74 - V^{\rm m}$. Finally, the bolometric luminosity is calculated via $BC_V^{\rm m}$ and the apparent visual magnitude of star m_V as $\log L_{\rm bol} = (DM + A_V - BC_V^{\rm m} - m_V + 4.74)/2.5$, where A_V is the total extinction and is equal to $E(B-V) R_V$. The absolute visual magnitude is calculated as $M_V = m_V - DM - A_V$.

With this procedure we simultaneously obtain the extinction parameter R_V and the color excess $E(B-V)$. This method relies on the relation of the B and V bands to the K_S band, and since the extinction is minimal in the K_S, the obtained bolometric luminosities are highly reliable. The uncertainty of the derived bolometric luminosity is dominated by the uncertainty in the distance to the target, for which we adopt a random error of 0.1 dex. Moreover, the SED fitting method (by eye) also result in an uncertainty in the A_V, which is inherited by the bolometric luminosity. Finally, the 2MASS photometry formal errors range from 0.01 to 0.1, averaging ≈ 0.05. Therefore, we estimate the uncertainty to be $\Delta L_{\rm bol} \approx \pm 0.1 - 0.2$ dex. In Appendix E we present the SED fits for the stars in our sample.

3.4.4. Line-broadening parameters

Out of all parameters that cause spectral line-broadening (macro-turbulent velocity v_{mac}, micro-turbulent velocity v_{mic}, and projected rotational velocity $v_{rot} \sin i$) we elected to include only $v_{rot} \sin i$ as part of the fitting procedure. When calculating the formal integral using CMFFLUX, we fix the v_{mic} in the photosphere to 10 km s^{-1} and the maximum v_{mic} in the wind to 100km s^{-1}.

Changing v_{mic} in the photosphere has little effect on wind lines, but the changes in line opacities do affect photospheric lines (primarily metal but also He $\textsc{i}$ lines). This produces a degeneracy between v_{mic} and chemical abundances. Therefore, increasing v_{mic} could lead to underestimating the abundances and temperatures (Brands et al. 2022), hence our decision to exclude v_{mic} from our fitting procedure. This degeneracy can be alleviated by simultaneously fitting v_{mic} and the abundances using multiplet lines. A common diagnostic of v_{mic} in B-stars is the depth of the components of Si $\textsc{iii}$ $\lambda\lambda\lambda 4553 - 4568 - 4575$, which are sensitive and react differently to changes in v_{mic} (McErlean et al. 1998).

The values of macro-turbulent velocities on OB-stars range from a few km s^{-1} for dwarfs up to a few tens of km s^{-1} for supergiants. We fix v_{mac} at 20 km s^{-1} in our fitting procedure. Fixing v_{mac} is appropriate for our sample, especially when taking into account the velocity resolution of the UBV and VIS arms of X-shooter that $\approx$ 45 and 25 km s^{-1}, respectively. The main diagnostic line for O-stars is O $\textsc{iii}$ 5592. For early B-stars O $\textsc{iii}$ 5592 is also used and as a sanity check we fit C $\textsc{iii}$ $\lambda 4267$ Si $\textsc{iv}$ $\lambda\lambda 4089 - 4116$, Si $\textsc{iii}$ $\lambda\lambda\lambda 4553 - 4568 - 4575$. for mid to late B-stars we fit the Mg $\textsc{ii}$ 4481 line and as a sanity check we use C $\textsc{ii}$ and Si $\textsc{ii}$.

The uncertainty in $v_{rot} \sin i$ measurements is dominated by the velocity resolution of the UBV arm of X-shooter (Vernet et al. 2011) $\Delta v \approx$ 45 km s^{-1}. Later in Section 4.4, we investigate the line-broadening characteristics of a subsample of our stars that have MIKE data by using the IACOB-BROAD tool (Simón-Díaz & Herrero 2014).

3.4.5. Terminal wind velocity (v_∞)

The "black velocity" v_{black} is the velocity measured at the bluest extent of fully saturated P Cygni absorption (Prinja et al. 1990). This is thought to provide a more robust estimate of the wind terminal velocity than the "edge velocity" v_{edge}, which is measured at the point where the blue trough of the P Cygni profile intersects the local continuum (Beckman & Crivellari 1985). The difference $v_{edge} - v_{black}$ arises from the turbulence in the velocity field of the wind.

In this study, we obtained v_{edge} and v_{black} using direct measurements of all the viable P Cygni resonance lines in the range $\approx$ [1200, 2900] Å, with the advantage of accurate radial velocity estimates for each object from optical metal lines. v_{edge} and v_{black} were determined as the mean value of all velocities obtained from the individual resonance lines. The resonance lines used are Si $\textsc{iv}$ $\lambda\lambda 1394 - 1403$, C $\textsc{iv}$ $\lambda\lambda 1548 - 1551$, Al $\textsc{iii}$ $\lambda\lambda 1855 - 1863$, Mg $\textsc{ii}$ $\lambda\lambda 2796 - 2803$.

Stars at low metallicity are well known for having absorption profiles that may not reach zero intensity, consequently it is sometimes not possible to obtain an accurate measurement of v_{black}, and one has to calculate v_∞ as a fraction of v_{edge}. The ratio v_{black}/v_{edge} is obtained from Tables C.1 and C.2.

3.4.6. Wind density parameters

The primary optical diagnostic line used to constrain the wind mass-loss rate is Hα, and in the case of O-supergiants, He $\textsc{ii}$ 4686 is used to a lesser extent. Hα is formed relatively close to the photosphere ($\approx 1 - 2\,R_*$) and since it is a recombination line it is very sensitive to wind density ($\sim \rho^2$). The wind density itself is a function of mass-loss rate and velocity field structure. Therefore the parameters we try to fit that affect the strength and the morphology of Hα within the framework of CMFGEN are wind terminal velocity v_∞, mass-loss rate $\dot{M}$, β and clumping parameters (volume filling factor f_{vol} and the onset clumping velocity v_{cl}). UV lines are used to further constrain the density and to break degeneracies of clumping and mass-loss. The most consistently available lines in our sample which we use to constrain the mass-loss rate and clumping are the unsaturated P Cygni sulphur doublet S $\textsc{iv}$ $1063 - 1073$, plus C $\textsc{iii}$ $\lambda 1176$ and Si $\textsc{iv}$ $\lambda\lambda 1394 - 1403$ if it is not fully saturated. We also use C $\textsc{iv}$ $\lambda\lambda 1548 - 1551$ for O-stars as a sanity check and for late B-stars we use Al $\textsc{iii}$ $\lambda 1856 - 1862$ and Mg $\textsc{ii}$ $\lambda 2796 - 2803$.

In our fine-tuned model, we adopt a value for the on-set clumping velocity v_{cl} equal to double the sound speed of the model, which comes to a value in the range $\approx 25 - 35$ km s^{-1} depending mainly on the temperature and helium abundance. This is a common procedure in the analysis of OB stars (Marcolino et al. 2009; Puebla et al. 2016). Since the connection velocity in our models is set by default to 10 km s^{-1}, the adopted values of v_{cl} indicate that the clumping becomes significant in the base of the super-sonic winds, rather than in the subsonic layers or the photosphere. Although, recent 2-D global simulations of O-stars indicate that wind inhomogeneities could originate from "photospheric turbulence" arising in the iron opacity peak zone due to the unstable nature of convection (Debnath et al. 2024).

Having acquired R_* (from the derived L_{bol} and T_{eff}), v_∞ and model mass-loss rate ($\dot{M}^m$), we derive the luminosity-adjusted mass-loss rate ($\dot{M}$) by scaling $\dot{M}^m$ to the transformed radius R_t via Eq. 4.

We estimate uncertainties of the wind parameters in a way that is suitable for our method of analysis. For v_∞ that is determined as v_{black} we calculate the uncertainty by quadrature of the systematic and stochastic errors. The systematic errors stem from the resolution of the instrument, and the stochastic errors are the combination of the standard deviation of the mean v_∞ and mean radial velocity v_{rad}. For v_∞ that is calculated as a fraction of v_{edge}, other than the resolution and the dispersion of the mean v_{edge} and v_{rad}, we additionally take into account in quadrature the standard deviation of v_∞/v_{edge} of the mean over our sample, which yields relatively higher v_∞ errors for stars that do not show saturated P Cygni profiles in their UV spectra.

It is quite difficult to quantify the uncertainty of β, but by varying beta in our model and adjusting the mass-loss rate accordingly we were able to get a general idea on the range of beta that would reproduce similar quality fit for Hα which is defined by the uncertainty $\Delta\beta = \pm 0.2$. The model uncertainty of the mass-loss rate $\Delta \log \dot{M}^m = \pm 0.05$ to 0.1 dex depending on the quality of the fit. Using Eq. 4 we calculate the uncertainty in the scaled mass-loss rates as:

$$\Delta \log \dot{M} = \sqrt{\left(\frac{4}{3}\frac{\Delta T_{eff}}{T_{eff}}\right)^2 + \dots}$$
$$\sqrt{\left(\frac{2}{\ln 10} \cdot \frac{\Delta \dot{M}^m}{\dot{M}^m}\right)^2 + \left(\cdot \frac{\Delta v_\infty}{v_\infty}\right)^2}. \tag{5}$$

3.4.7. He and CNO abundances

The accurate determination of both the effective temperature and surface gravity depends on the helium abundance in the model, especially for O-stars because of the way the temperature is gauged by He I to He II equivalent widths ratio. To restrict the helium mass fraction (Y) we fix the mass fraction of all included elements except for hydrogen, which means that increasing or decreasing the mass fraction of helium in the model would respectively deplete or enrich the model with hydrogen. We use the following Helium line diagnostics:

He I $\lambda4026$, He I $\lambda4471$, He I $\lambda4922$, (He I $\lambda6678$), (He I $\lambda7065$), (He I $\lambda7281$), He II $\lambda4542$, He II $\lambda5411$.

Recalling Section 3, plane parallel model atmosphere have been very successful at determining metal abundances of early type stars with weak winds (e.g., Hunter et al. 2007; Przybilla et al. 2008), which have included late B-supergiants (Przybilla et al. 2006). Models employing spherical geometry generally require significantly higher resources, hindering abundance determinations, although FASTWIND has been successfully used to obtain CNO abundances in early B-supergiants (Urbaneja et al. 2005b). Since CMFGEN is used for the present study, we acknowledge larger uncertainties in derived CNO abundances with respect to other analyses. Nevertheless, after obtaining the stellar and wind parameters we try to fit multiple lines that adhere to different ionization levels of CNO elements. The lines depend on the spectral type of the star, but the primary lines that we use to refine the CNO abundances are:

–   Carbon:
    O-stars: C IV $\lambda\lambda5801-5811$, C III $\lambda\lambda4647-4650$
    B-stars: C III $\lambda\lambda4647 - 4650$, C III $\lambda5696$, C II $\lambda4070$, C II $\lambda4267$, C II $\lambda\lambda6578 - 6582$, C II $\lambda\lambda\lambda7231 - 7236 - 7237$
–   Nitrogen:
    O-stars: N III $\lambda4097$, N III $\lambda\lambda4510-4515$, N III $\lambda\lambda4634-4641$
    B-stars: N III $\lambda4097$, N II $\lambda3995$, N II $\lambda4447$, N II $\lambda\lambda\lambda4601 - 4607 - 4614$, N II $\lambda4630$
–   Oxygen:
    O-stars: O III $\lambda\lambda3261-3265$, O III $\lambda3760$, O III $\lambda5592$
    B-stars: O II $\lambda4254$, O II $\lambda4367$, O II $\lambda\lambda4415 - 4417$, O II $\lambda\lambda4638 - 4641$, (O I $\lambda\lambda\lambda7772 - 7774 - 7775$).

The triplet N III $\lambda4634 - 4641$ is usually in emission and is notoriously difficult to fit (Rivero González et al. 2011). In some objects C III $\lambda5696$ is also in emission. We leave fitting CNO abundances as the last step in our fitting procedure since it does not effect other diagnostic lines that are used to gauge other parameters. He I and O I lines quoted above in parentheses were not part of the analysis and are only used as supplementary diagnostics.

The CNO abundances we present in Section 4.5 are subject to large uncertainties, for which we adopt a value of $\approx \pm0.3$ dex. This is due to the high sensitivity of metal lines to changes in $T_{\rm eff}$ and $\log g$, in addition to changes in $v_{\rm mic}$. We are more confident in our helium abundances, and we determine our uncertainties based on the way we varied the helium mass fraction in our models (in steps of 10% of the baseline grid abundance), so we adopt a 20% uncertainty in the mass-fraction with translates to 0.09 dex for the helium abundance by number $\epsilon_{\rm He} = \log \frac{\rm He}{\rm H} + 12$.

4. Results

In this section we present an overview of the results and compare them to other theoretical and empirical results that utilise
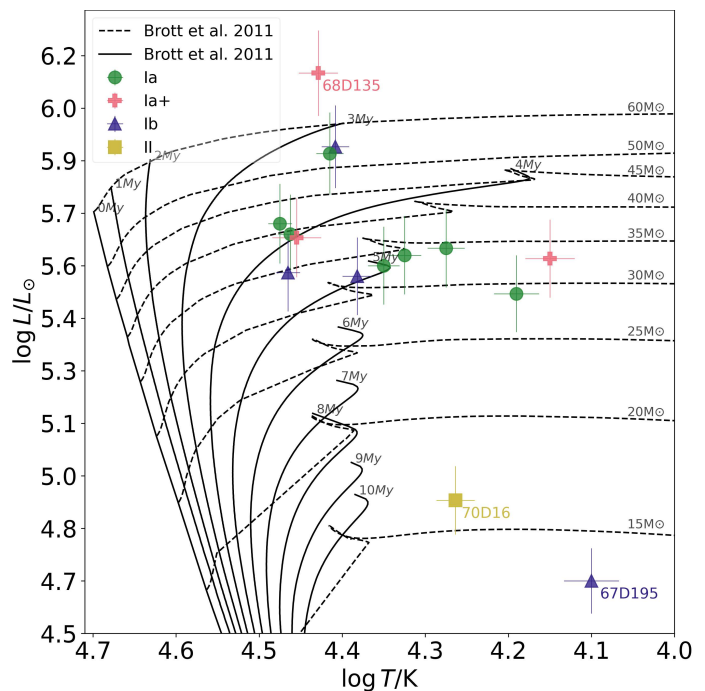
Fig. 7: The Hertzsprung-Russell diagram for our sample. Overlaid in solid black lines are non-rotating isochrones for different ages ($\approx [0 - 10]$ Myr) and dashed black lines are the evolutionary tracks for stellar masses in the range $\approx [10 - 60]\ M_\odot$ with a rotational velocity of 50 km s^{-1}. Both the isochrones and evolutionary tracks are adopted from Brott et al. (2011).

the UV and optical or the optical range exclusively. The quality of our analysis is described for each star individually in the Appendix B. Best fitting physical parameters are presented in Table 4, including inferred evolutionary masses and ages from BONNSAI (Schneider et al. 2014) applied to Brott et al. (2011) rotating single-star evolutionary models for LMC metallicity.

4.1. Hertzsprung-Russell diagram

Fig. 7 shows the location of our targets on a Hertzsprung-Russell diagram (HRD). Our sample spans a range of temperatures $\log(T_{\rm eff}/{\rm K}) \approx 4.1-4.5$, while luminosities cover a broad range of $\log(L_{\rm bol}/L_\odot) \approx 4.50-6.10$ (see Table 4). The extremey luminous star is the hypergiant Sk $-68°$ 135 (Fig. G.5) with $\log(L_{\rm bol}/L_\odot) \approx 6.1$.

The majority of our sample excdeed $\log(L_{\rm bol}/L_\odot) \approx 5.4$ aside from Sk $-70°$ 16, which is a bright giant (II), and Sk $-67°$ 195, which is a B8 Ib supergiant according to Bestenlehner et al. (2025). Overall, the majority of the sample lies between the zero age main sequence (ZAMS) and the terminal age main sequence (TAMS), according to the evolutionary models of Brott et al. (2011), but several targets, assuming a single-star evolutionary scenario, are located beyond the TAMS and would therefore be identified as post-main sequence stars.

Fig. 8 shows the location of our targets on the spectroscopic Hertzsprung-Russell diagram (sHRD) (Langer & Kudritzki 2014), where $\mathcal{L} = T_{\rm eff}^4/g$ and $\mathcal{L}_\odot$ is calculated with solar values $T_{\rm eff} = 5777$ kK and $\log(g/{\rm cm\,s^{-1}}) = 4.44$. The majority of our stars fall in the $\log \mathcal{L}/\mathcal{L}_\odot$ range of $4.0-4.3$. We find that the hypergiants are the closest to the Eddington limit of $\log \mathcal{L}/\mathcal{L}_\odot \approx 4.6$ (assuming a hydrogen mass fraction of 0.73). Also, as expected, the low luminosity supergiant Sk $-67°$ 195

Table 4: Derived stellar parameters based on the best fitting CMFGEN model. M_{init}, M_{evo}, and ages of the stars are derived using an updated Bayesian inference method (Bronner et al. in prep) that is similar to BONNSAI (Schneider et al. 2014) applied to Brott et al. (2011) evolutioanry tracks. Γ_e is calculated using M_{evo}.

Sk −	T_{eff}	Diag.	$\log g_c$	R_*	$\log L_{bol}$	R_V	$E(B-V)$	M_V	BC_V	v_{rad}	$v_{rot} \sin i$	M_{spec}	Γ_e^{spec}	M_{init}	M_{evo}	Age	Γ_e^{evo}
	kK		cm s^{-2}	$R_\odot$	$L_\odot$		mag	mag	mag	km s^{-1}	km s^{-1}	$M_\odot$		$M_\odot$	$M_\odot$	My	
66° 171	29.9±1.0	He I – He II	3.11±0.20	25	5.67±0.11	1.9	0.16	−6.6	−2.83	410	75	31 ±7	0.73	$34.61^{+9.03}_{-4.34}$	$30.04^{+8.14}_{-2.26}$	$5.27^{+0.67}_{-1.03}$	$0.74^{+0.27}_{-0.08}$
68° 155	29.0±1.0	He I – He II	3.06±0.20	26	5.64±0.11	2.9	0.29	−6.6	−2.76	240	80	29 ±6	0.72	$34.21^{+8.41}_{-7.98}$	$29.89^{+8.49}_{-4.59}$	$5.47^{+0.22}_{-0.95}$	$0.70^{+0.29}_{-0.16}$
69° 279	28.5±2.0	He I – He II	2.95±0.25	27	5.63±0.11	2.6	0.34	−6.6	−2.76	230	40	24 ±6	0.90	$33.79^{+7.11}_{-3.21}$	$30.25^{+7.71}_{-1.37}$	$4.23^{+0.60}_{-0.44}$	$0.70^{+0.26}_{-0.08}$
71° 41	29.2±1.0	He I – He II	3.12±0.20	23	5.53±0.11	2.8	0.25	−6.3	−2.77	260	45	25 ±5	0.69	$32.80^{+4.82}_{-3.48}$	$30.30^{+5.30}_{-2.09}$	$4.26^{+0.60}_{-0.31}$	$0.57^{+0.18}_{-0.08}$
68° 135	26.9±1.5	He I – He II	2.82±0.24	51	6.10±0.12	2.8	0.28	−7.9	−2.60	270	45	65 ±16	0.96	$60.74^{+16.54}_{-6.69}$	$52.35^{+14.90}_{-4.63}$	$3.25^{+0.74}_{-0.71}$	$0.89^{+0.2}_{-0.00}$
67° 5	25.6±1.0	He I – He II	2.81±0.20	45	5.89±0.12	2.2	0.17	−7.5	−2.46	295	65	47 ±11	0.76	$44.19^{+9.10}_{-4.57}$	$38.12^{+6.09}_{-0.95}$	$4.79^{+0.28}_{-0.95}$	$0.95^{+0.16}_{-0.10}$
68° 52	26.0±1.0	Si III – Si IV	2.85±0.20	42	5.87±0.12	2.9	0.22	−7.4	−2.51	255	50	46 ±10	0.83	$49.52^{+7.30}_{-8.41}$	$44.97^{+6.72}_{-6.46}$	$3.40^{+0.45}_{-0.34}$	$0.85^{+0.15}_{-0.15}$
69° 43	22.4±1.0	Si III – Si IV	2.71±0.21	40	5.55±0.11	2.5	0.19	−7.0	−2.14	255	50	29 ±6	0.63	$31.94^{+4.11}_{-3.55}$	$29.47^{+4.06}_{-2.30}$	$5.15^{+0.43}_{-0.69}$	$0.62^{+0.14}_{-0.09}$
68° 140	24.1±1.0	Si III – Si IV	2.81±0.21	33	5.52±0.11	3.1	0.34	−6.7	−2.32	260	50	26 ±7	0.67	$30.21^{+4.47}_{-3.23}$	$29.06^{+3.81}_{-3.08}$	$5.21^{+0.61}_{-0.72}$	$0.59^{+0.14}_{-0.11}$
67° 2	18.8±1.0	Si III – Si IV	2.31±0.21	71	5.76±0.12	2.7	0.27	−7.9	−1.73	320	45	38 ±6	0.76	$41.53^{+7.90}_{-3.04}$	$36.64^{+6.16}_{-1.93}$	$4.24^{+0.37}_{-0.49}$	$0.75^{+0.18}_{-0.07}$
67° 14	21.1±1.0	Si III – Si IV	2.51±0.21	46	5.58±0.11	1.6	0.16	−7.2	−2.00	300	50	25 ±10	0.73	$39.98^{+2.50}_{-6.18}$	$35.50^{+2.09}_{-4.06}$	$4.75^{+0.40}_{-0.35}$	$0.53^{+0.08}_{-0.12}$
69° 52	18.8±1.0	Si III – Si IV	2.31±0.21	59	5.60±0.11	1.9	0.28	−7.5	−1.73	260	50	26 ±7	0.72	$40.57^{+5.77}_{-1.92}$	$35.56^{+4.48}_{-1.05}$	$4.44^{+0.26}_{-0.24}$	$0.53^{+0.14}_{-0.06}$
67° 78	15.5±1.0	Si II – Si III	2.10±0.21	75	5.47±0.11	2.2	0.17	−7.6	−1.33	310	30	26 ±7	0.58	$28.56^{+3.61}_{-3.80}$	$27.72^{+2.61}_{-4.02}$	$5.49^{+1.03}_{-0.60}$	$0.55^{+0.11}_{-0.16}$
70° 16	18.4±1.0	Si II – Si III	2.61±0.21	27	4.88±0.10	1.9	0.19	−5.8	−1.70	265	30	11 ±3	0.36	$16.21^{+1.45}_{-1.41}$	$16.02^{+1.45}_{-1.31}$	$10.40^{+1.57}_{-1.12}$	$0.24^{+0.11}_{-0.10}$
68° 8	14.1±1.0	Si II – Si III	1.81±0.21	102	5.57±0.11	2.4	0.25	−8.1	−1.13	250	35	24 ±7	0.74	$31.59^{+4.56}_{-4.25}$	$29.59^{+5.08}_{-4.93}$	$5.20^{+0.74}_{-0.77}$	$0.61^{+0.19}_{-0.18}$
67° 195	12.6±1.0	He I – Mg II	2.11±0.22	44	4.65±0.10	2.9	0.14	−6.1	−0.83	300	25	9 ±3	0.24	$13.23^{+1.24}_{-0.98}$	$13.20^{+1.17}_{-0.10}$	$13.94^{+1.70}_{-1.87}$	$0.17^{+0.12}_{-0.08}$

Presented uncertainties for effective temperatures T_{eff} are double the model uncertainty (see Section 3.4). In the uncertainties of centrifugal force-corrected surface gravity $\log g_c$, we take into account the model uncertainty of $\log g$ and the uncertainty of the projected rotational velocity $v_{rot} \sin i$ and the radius R_*. The uncertainty in radial velocity v_{rad} measurements is dominated by the velocity resolution of the UBV part of the spectrum which is $\Delta v \approx 45$ km s^{-1}. The relative extinction R_V ($\Delta R_V \approx 0.3$ mag), color excess $E(B-V)$ ($\Delta E(B-V) \approx 0.05$ mag), absolute V-band magnitude M_V, and bolometric correction BC_V are produced from the SED fits that are shown in Appendix E. Γ_e^{spec} is subject to uncertainties of $\Delta\Gamma_e^{spec} \approx 0.18$ which takes into account the uncertainties of M_{spec} and $\log L_{bol}$.
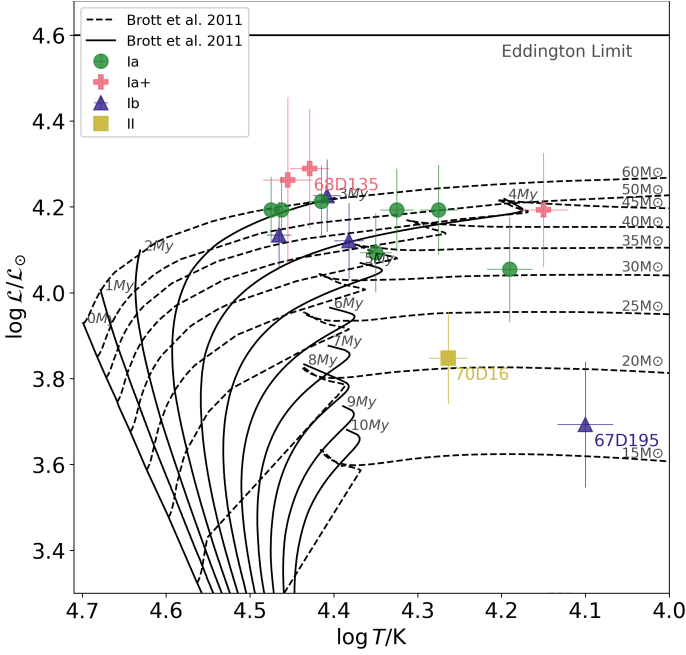
Fig. 8: The spectroscopic Hertzsprung-Russell diagram for our sample. The evolutionary tracks (solid black lines) and the isochrones (dashed black lines) are the same as in Fig. 7, which are taken from Brott et al. (2011). The Encoding of the luminosity classes is the same as in Fig. 7

and the bright giant Sk −70° 16 are the furthest away from the Eddington limit with $\log \mathcal{L}/\mathcal{L}_\odot$ equal to 3.68 and 3.82, respectively.

We also compare a calibration of the bolometric correction in the visual band BC_V versus $T_{\rm eff}$ to the calibration obtained by Lanz & Hubeny (2007) from TLUSTY non-LTE plane-parallel models of B-stars. A simple fit to our dataset reveals:

$$BC_V/\text{mag} = 21.00 - 5.33 \log (T_{\rm eff}/\text{K}), \tag{6}$$

with a standard deviation of $\approx$ 0.1 mag, which support the results of Lanz & Hubeny (2007) for the LMC, who finds:

$$BC_V/\text{mag} = 21.08 - 5.36 \log (T_{\rm eff}/\text{K})$$

As to be expected for a UV-bright sample, extinctions are relatively low with an average color excess $E(B-V) = 0.23 \pm 0.06$ mag, and an average total extinction in the V-band $A_V^{\rm average} = 0.6 \pm 0.4$ mag. This agrees with the findings of Gordon et al. (2003).

4.2. Stellar masses

Evolutionary masses ($M_{\rm evo}$) presented in Table 4 are derived via a Bayesian inference method that is similar to Bonnsai (Schneider et al. 2014) with updated techniques (Bronner et al. in prep) applied to LMC tracks from Brott et al. (2011) with $L_{\rm bol}$, $T_{\rm eff}$, $\log g$, $v_{\rm rot} \sin i$, and $\log \frac{\rm He}{\rm H} + 12$ as input parameters. Our sample spans a wide range range of ($M_{\rm evo}$) of $13.20^{+1.17}_{-0.10}$ $M_\odot$ (Sk −67° 195) to $52.35^{+14.90}_{-4.63}$ $M_\odot$ (Sk −68° 135). Table 4 also includes stellar ages that range from $3.40^{+0.45}_{-0.34}$ Myr (Sk −68° 135) to $13.94^{+1.70}_{-1.87}$ Myr (Sk −67° 195).

In Table 4 we present our values of the true surface effective gravity $\log (g_c/\text{cm s}^{-2}) = \log (g_{\rm model} + v_{\rm rot} \sin i^2/R_*)$, where R_* is
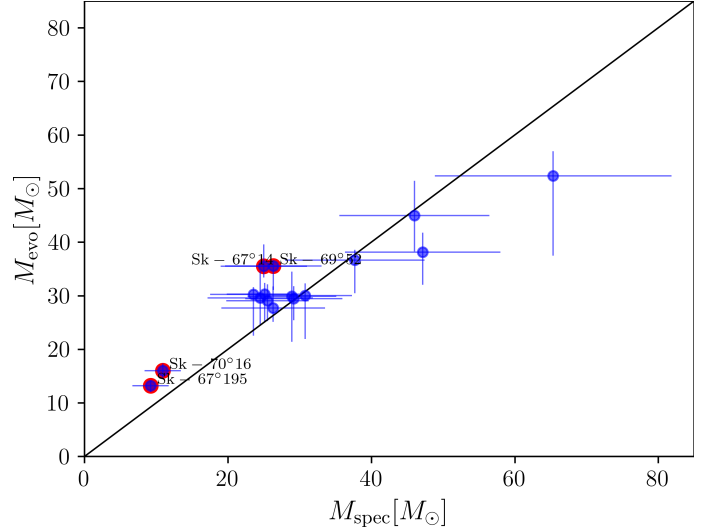

Fig. 9: Blue circles: spectroscopically obtained mass from our analysis $M_{\rm spec}$ versus the mass produced by Bonnsai (Schneider et al. 2014) applied to evolutionary tracks from Brott et al. (2011) $M_{\rm evo}$. Red circles overlaid onto the blue points depicts stars that have a sginificant discrepancy between their $M_{\rm spec}$ and $M_{\rm evo}$.

obtained from Stefan–Boltzmann law. g_c takes into account the centrifugal force due to stellar rotation (Herrero et al. 1992). Our values range from $\log g_c \approx 1.8$ to 3.1 due to the stars possessing large radii ($R_* > 20$ $R_\odot$), which is expected for a sample that consists of evolved OB-stars.

We derive the spectroscopic masses ($M_{\rm spec}$) from the gravities via $g = G M/R_*^2$. Therefore, we derive relative uncertainties of 20% − 30%, which mainly depend on the uncertainties of $\log g$, which is largely affected by quality of normalization. To put this into perspective, a difference in the wings of the Balmer lines of 1% can potentailly lead to a $\log g$ difference up to ≈ 0.1 dex. Such a difference leads to a relative uncertainty of $\Delta M_{\rm spec} \approx 20\%$.

Spectroscopic masses are compared to evolutionary masses in Fig. 9. This shows that, for most of the stars, $M_{\rm spec}$ and $M_{\rm evo}$ are consistent within the uncertainties, similar to what Schneider et al. (2018) finds in a large sample of OB-stars. For some of the stars (red circles in Fig. 9), the mass discrepancy that was established for Galactic O-supergiants by Herrero et al. (1992), and later expanded to SMC O-stars by Trundle et al. (2004) and further to Galactic B-supergiants in Crowther et al. (2006) persists. We find that the spectroscopic masses for these stars are significantly lower than the masses produced by evolutionary models.

The Eddington parameter $\Gamma_e^{\rm evo}$ presented in Table 4 is derived using the evolutionary masses and it ranges from $\Gamma_e = 0.18^{+0.03}_{-0.03}$ (Sk −67° 195) to $0.95^{+0.02}_{-0.12}$ (Sk −67° 5). We note that for the hypergiant Sk −68° 135 we obtain $\Gamma_e = 1.04^{+0.05}_{-0.15}$, which is unphysical, therefore we adopt the value corresponding to the lower limit of $\Gamma_e = 0.89$.

4.3. Wind properties

4.3.1. Terminal wind velocity v_∞

measured wind velocities are presented in Table 5. In Fig. 10 we compare our $v_\infty - (T_{\rm eff})$ to the empirical recipe of Hawcroft et al. (2024), adopting a simple linear fit of the form:

$$v_\infty[\text{km s}^{-1}] = a T_{\rm eff}[\text{K}] - b. \tag{7}$$

Table 5: Wind parameters for our targets. The mass-loss rates of Sk −70° 16 and Sk −67° 195 are upper limits. Escape velocities are adjusted for Γ_e.

Target	L_{bol}	$\log \dot{M}$	v_∞	$v_{esc,(1-\Gamma_e)}$	β	f_{vol}	v_{cl}
Sk −	$L_\odot$	$M_\odot\,yr^{-1}$	km s^{-1}	km s^{-1}			km s^{-1}
66° 171	5.67	−6.07 ±0.33	1775 ±63	680	1.7	0.03	30
68° 155	5.64	−6.19 ±0.25	1520 ±61	650	1.5	0.03	30
69° 279	5.63	−5.70 ±0.39	630 ±62	580	2.7	0.1	30
71° 41	5.53	−6.03 ±0.25	1390 ±112	650	1.2	0.1	35
68° 135	6.10	−5.70 ±0.31	880 ±62	690	2.3	0.1	35
67° 5	5.89	−6.05 ±0.35	1230 ±61	630	1.3	0.1	30
68° 52	5.87	−6.28 ±0.25	1140 ±62	640	2.0	0.03	35
69° 43	5.55	−6.49 ±0.25	825 ±64	530	2.0	0.1	30
68° 140	5.52	−6.46 ±0.25	1000 ±62	540	2.2	0.1	30
67° 2	5.76	−6.21 ±0.26	435 ±61	450	3.0	0.14	30
67° 14	5.58	−6.33 ±0.29	810 ±67	460	2.0	0.1	30
69° 52	5.60	−6.62 ±0.38	465 ±61	410	2.5	0.14	25
67° 78	5.47	−6.70 ±0.40	380 ±75	360	3.0	0.2	30
70° 16	4.88	−7.60 ±0.34	235 ±70	390	1.0	0.1	25
68° 8	5.57	−6.50 ±0.26	210 ±65	300	1.0	0.1	25
67° 195	4.65	−7.50 ±0.35	210 ±62	280	1.0	0.1	25

Table 6: Slopes a, and offsets, b, of the linear fits to the terminal wind velocity equation (Equation 7) of this study, and Hawcroft et al. (2024)

LMC	a	b
	K	km s^{-1}
This study	0.076 ± 0.011	884 ± 260
Hawcroft et al. (2024)	0.085 ± 0.050	1150 ± 170

In Table 6 we present the parametres of the linear fit in Equation 7. We find that our v_∞-T_{eff} relation agrees with the relation obtained by Hawcroft et al. (2024) within the uncertainties. We note that the two outliers are the hypergiants Sk -69° 279 (Fig. G.3) and Sk -68° 135 (Fig. G.5), which have abnormally low v_∞ compared to stars of similar temperatures.

We also compare our results to numerical predictions of wind velocity from Vink & Sander (2021) and Krtička et al. (2024). The velocities calculated using the recipe provided in Vink & Sander (2021), which was obtained using a locally consistent Monte Carlo radiative transfer model (Müller & Vink 2008), agree with our measurements for stars located at the 'cool' side of the bi-stability jump predicted in Vink et al. (2001) (< 25 kK), where as we find large discrepancies in the wind velocities of the objects that are located above the 'hot' edge of the bi-stability jump. As for the velocities calculated by the recipe presented in Krtička et al. (2024), we find that there is a discrepancy in the general trend, but just as in our results, there is a lack of a downward jump in the temperature range $T_{eff} \approx 25-21$ kK.

We also calculate the values of the escape velocity of each star (see Table 5) using the evolutionary mass obtained via Bonn-
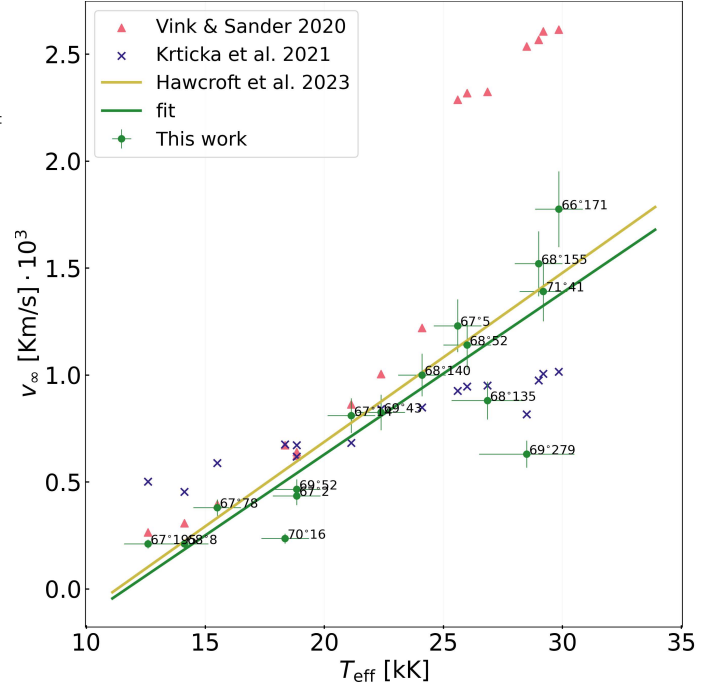

Fig. 10: v_∞ versus T_{eff} for LMC supergiants. Green dots: results from this work, green line: linear fit of our results, yellow line: v_∞-T_{eff} relation from Hawcroft et al. (2024), pink triangles: v_∞ calculated velocities from Vink & Sander (2021) recipe, violet diagonal cross: v_∞ calculated velocities from (Krtička et al. 2021) recipe.

sai as explained in Section 4.2. We discuss the implications of our findings later in Section 5.1.

4.3.2. Mass-loss and clumping

Fig. 11 presents the spectral fits to Hα for all the stars in our sample. Aside from a few peculiar cases, our models well reproduce the overall shape and intensity of the emission feature in Hα as shown in. The results for the true mass-loss rates that are scaled to the transformed radius and volume-filling factor are presented in Table 5.

A good indicator of wind strength is the Eddington ratio ($\Gamma_e = L_{bol}/L_{edd}$), and it is expected that objects with higher Γ_e will have a greater mass-loss rate (Vink et al. 2011; Bestenlehner et al. 2014). In Fig. 12 a correlation between Γ_e and $\dot{M}$ is revealed.

Spectral fits in this study were applied to a single XshootU observation, so we present the Magellan/MIKE (Crowther 2024) Hα spectrum of Sk −67° 78 in Fig. 13. Hα is significantly weaker in MIKE observations with respect to XshootU. This would lead to different $\dot{M}$, β and f_{vol} if we were to apply our fitting to MIKE data. Therefore, we include a factor of 2 in the uncertainties of the model mass-loss rates to take into account the possible variation in Hα and the additional error from having non-simultaneous UV and optical observation. This puts the uncertainty for the derived mass loss rates in the range $\Delta \log \dot{M} \approx \pm 0.2-0.4$ dex.

For Sk −70° 16 (Fig. G.14) and Sk −67° 195 (Fig. G.16) we adopt $\beta = 1.0$ due to Hα being fully in absorption. For the rest of our sample, we find that higher $\beta = 2.0 \pm 0.6$ are preferred to achieve a satisfactory fit for Hα. This is in agreement with Crowther et al. (2006) in which CMFGEN was used to model
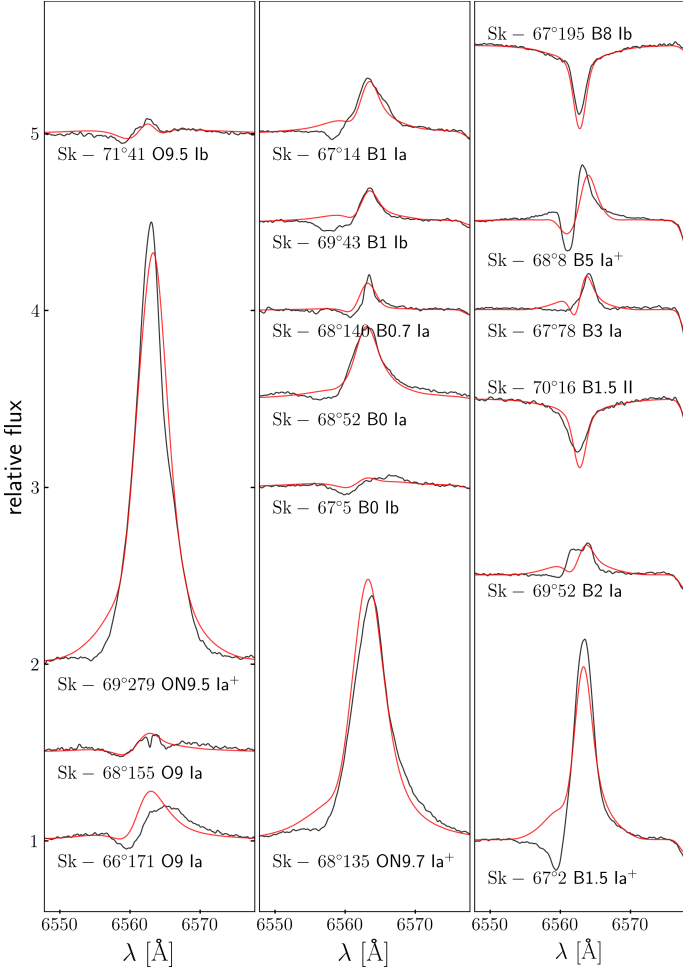
Fig. 11: Spectral fits to Hα for our sample of OB-supergiants. Black line: observations, red line: model fit
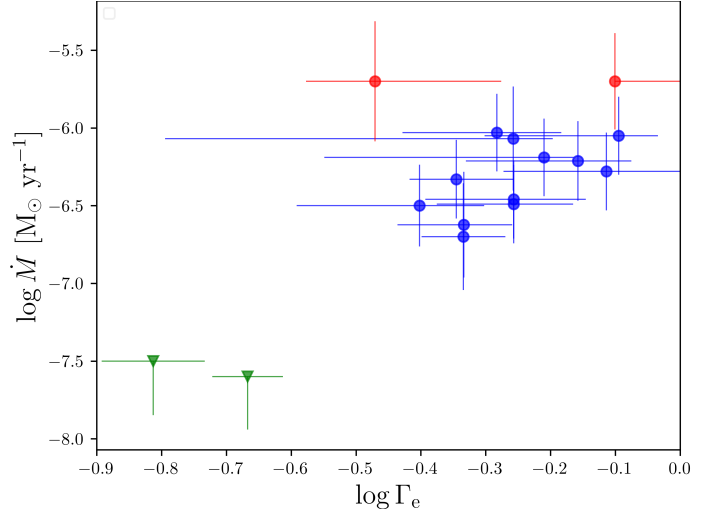

Fig. 12: $\dot{M}$ versus $\Gamma_{\rm e}$. The green triangles indicate the objects Sk $-67°$ 195 and Sk $-70°$ 16, the mass-loss rates of which are considered upper limits. The red points correspond to the hypergiants Sk $-67°$ 279 and Sk $-68°$ 135.

Table 7: Comparison of the broadening paramaters adopted in our analysis to those obtained via IACOB-BROAD (Simón-Díaz & Herrero 2014) applied to high resolution MIKE data.

Sk $-$	XShootU		IACOB-BROAD		MIKE
	$v_{\rm rot} \sin i$	$v_{\rm mac}$	$v_{\rm rot} \sin i$	$v_{\rm mac}$	line
	km s^{-1}	km s^{-1}	km s^{-1}	km s^{-1}	
67° 2	45	20	46^{+10}_{-15}	40^{+17}_{-20}	Si III λ4552
67° 78	30	20	39^{+10}_{-29}	23^{+33}_{-22}	Si III λ4552
70° 16	35	20	40^{+10}_{-25}	35^{+13}_{-17}	Si III λ4552
68° 8	40	20	38^{+7}_{-15}	22^{+22}_{-20}	Si III λ4552
67° 195	30	20	28^{+8}_{-14}	28^{+14}_{-16}	Si II λ6347

cool Galactic B-supergiants and they find an average value of 2.0 for β is necessary to achieve a good fit. This is also in agreement with Haucke et al. (2018), in which they analysed Galactic B-supergiants using FASTWIND and find that the suitable average value for β is also $\approx$ 2.0. We present our β values in Table 5.

Fig. 14 demonstrates the effect of varying β for Sk $-68°$ 140. In the middle panel of Fig. 15, we present the line-formation region of Hα (blue solid line) for Sk $-68°$ 140. The peak is at $\log(r/R_*) \approx 0.2 - 0.4$, which is well into the sonic regime of the atmosphere, and is averaged over a wide range of $v_{\rm wind}$ ($\log(r/R_*) \approx 0.1 - 0.8$). From Equation 3 it is clear that increasing β lowers the acceleration of the wind. This leads to lower wind velocities at Hα line-formation region, where the wind has not yet reached it's terminal velocity, resulting in higher densities at this region. This yields narrower red-shifted emission and blue-shifted absorption in Hα with less extended wings

In Fig. 14, although the model with $\beta = 2.5$ (the blue solid line on Fig. 14) fits the blue shifted absorption better its emission is weaker than the observation, and the model with $\beta = 2.0$ (green solid line) fits the extended red wing of the emission but has an overly extended blue wing and is stronger than the observed emission. Therefore we select the model with $\beta = 2.2$ (red solid line), which matches the observed emission and fits the overall morphology of the line.

4.4. Line-broadening parameters

In Table 4, we include $v_{\rm rot} \sin i$, the values of which are within reasonable agreement with the spectroscopic pipeline results from Bestenlehner et al. (2025). The values of $v_{\rm rot} \sin i$ we obtain for our stars are in the range $\approx 25-80$ km s^{-1}.

In Table 7, we compare our derived $v_{\rm rot} \sin i$, which were obtained with the assumption of $v_{\rm mac} = 20$ km s^{-1}, to the $v_{\rm rot} \sin i$ and $v_{\rm mac}$ that were obtained by applying the IACOB-BROAD (Simón-Díaz & Herrero 2014) tool to a subsample of the stars analysed in this study that has high resolution MIKE data. IACOB-BROAD is a procedure based on a combined fourier transform and goodness of fit approach that allows for the extraction of line-broadening parameters from a single snapshot of OB-type star spectra.

We utilise Si III λ4552 for all stars in the subsample except the for the late supergiant Sk $-67°$ 195, for which we use Si II λ6347. We find that our derived $v_{\rm rot} \sin i$ are in good agreement with those obtained from IACOB-BROAD. On the other hand, we systematically underestimate $v_{\rm mac}$ by $\approx$ 10 km s^{-1}. This implies that we could potentially be underestimating the CNO abundances in our sample, albeit this understimation is well within our adopted uncertainties of 0.3 dex.
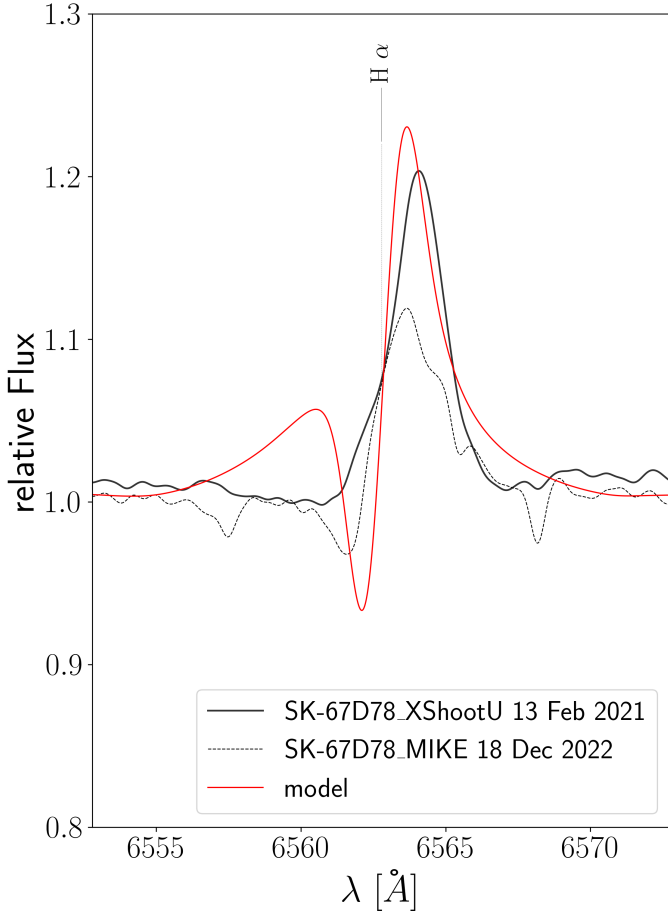
Fig. 13: Hα of Sk −67° 78 from MIKE observations (black dashed line) overlaid onto Hα from XshootU (black solid line) with our best fitting model (red solid line).

4.5. He and CNO abundances

Table 8 presents the results for the chemical abundances of He and CNO elements. The analysis shows an overall boost in helium at the expense of hydrogen relative to the LMC baseline helium mass fraction of $Y = 0.25$ (Brott et al. 2011). This is to be expected for a sample of evolved stars. We would also expect nitrogen enrichment at the expense of oxygen and carbon which get depleted due to CNO-cycle processing. Indeed, nitrogen abundances are significantly higher than the LMC baseline (Fig. 16), with a mean enhancement of 1 dex and a spread of 0.5 dex. We also note that our sample is mostly carbon and oxygen depleted with the exception of Sk −71° 41 (Fig. G.4) and Sk −67° 2 (Fig. G.10) where we find a 0.2 dex enhancement in oxygen.

Recalling Section 3.4.7, it is necessary to use lines of lower ionization stages for B-stars that O-stars. In panels *d-l* of Fig. 17, we use the best fitting models for Sk −66° 171, Sk −68° 140, and Sk −68° 8 (left to right, respectively), which corresponds to temperatures of 29.9, 24.1, and 14.1 kK, respectively, to plot the radial ionization structure of helium, nitrogen and iron. This shows that the atmosphere is dominated by lines of different ionization levels depending on the temperature, which illustrates the reason behind fitting lines of lower ionization stages with lower T_{eff}.

In Fig. 15, we show the line formation regions of different lines versus radius v_{wind}, and we can see that photospheric lines like He I λ4471 (red solid lines), N III λ4097, and N II λ4447
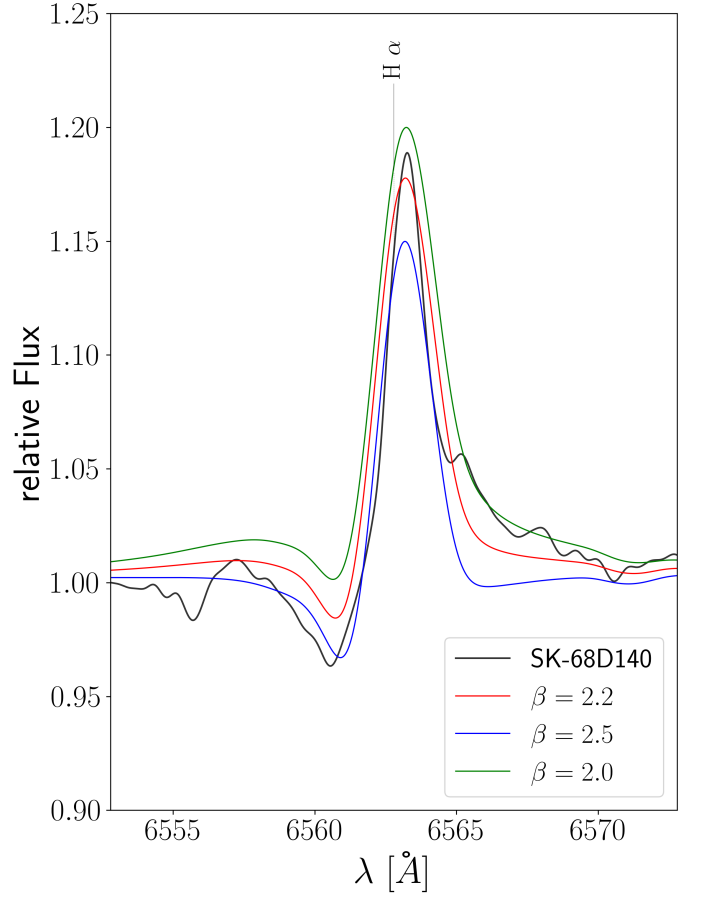
Fig. 14: Best fitting model $\beta = 2.2$ (red solid line) versus two other models with $\beta = 2.5$ (blue solid line) and $\beta = 2.0$ (green solid line) for Hα of Sk −68° 140 (black solid line)

Table 8: Best fitting photospheric abundances $\epsilon_X = \log X/H + 12$. The final two columns are the cumulative CNO abundances relative to LMC baseline (Vink et al. 2023) and solar (Asplund et al. 2005), respectively. The adopted uncertainty on CNO abundances is ±0.3

| Sk −	Y	ϵ_C	ϵ_N	ϵ_O	$\frac{\Sigma CNO}{\Sigma CNO_{LMC}}$	$\frac{\Sigma CNO}{\Sigma CNO_\odot}$
66° 171	0.43 ± 0.085	8.05	8.19	8.42	1.2	0.5
68° 155	0.43 ± 0.085	7.53	8.25	8.42	1.1	0.5
69° 279	0.36 ± 0.073	7.53	8.02	8.07	0.6	0.3
71° 41	0.30 ± 0.061	7.79	7.50	8.70	1.7	0.8
68° 135	0.36 ± 0.073	7.53	8.24	8.17	0.9	0.4
67° 5	0.47 ± 0.094	7.61	7.62	8.45	0.8	0.4
68° 52	0.30 ± 0.061	7.49	7.50	8.33	0.8	0.4
69° 43	0.30 ± 0.061	7.49	7.50	8.33	0.8	0.4
68° 140	0.30 ± 0.061	7.19	8.10	8.33	1.0	0.5
67° 2	0.43 ± 0.085	7.32	8.40	8.34	1.1	0.5
67° 14	0.36 ± 0.073	7.53	7.72	8.67	1.4	0.7
69° 52	0.43 ± 0.085	7.53	8.36	8.42	1.2	0.5
70° 16	0.30 ± 0.061	7.39	8.24	8.33	1.1	0.5
67° 78	0.30 ± 0.061	7.65	7.98	8.33	1.0	0.5
68° 8	0.40 ± 0.079	7.85	8.47	8.39	1.4	0.7
67° 195	0.36 ± 0.073	7.71	8.02	8.37	1.0	0.5
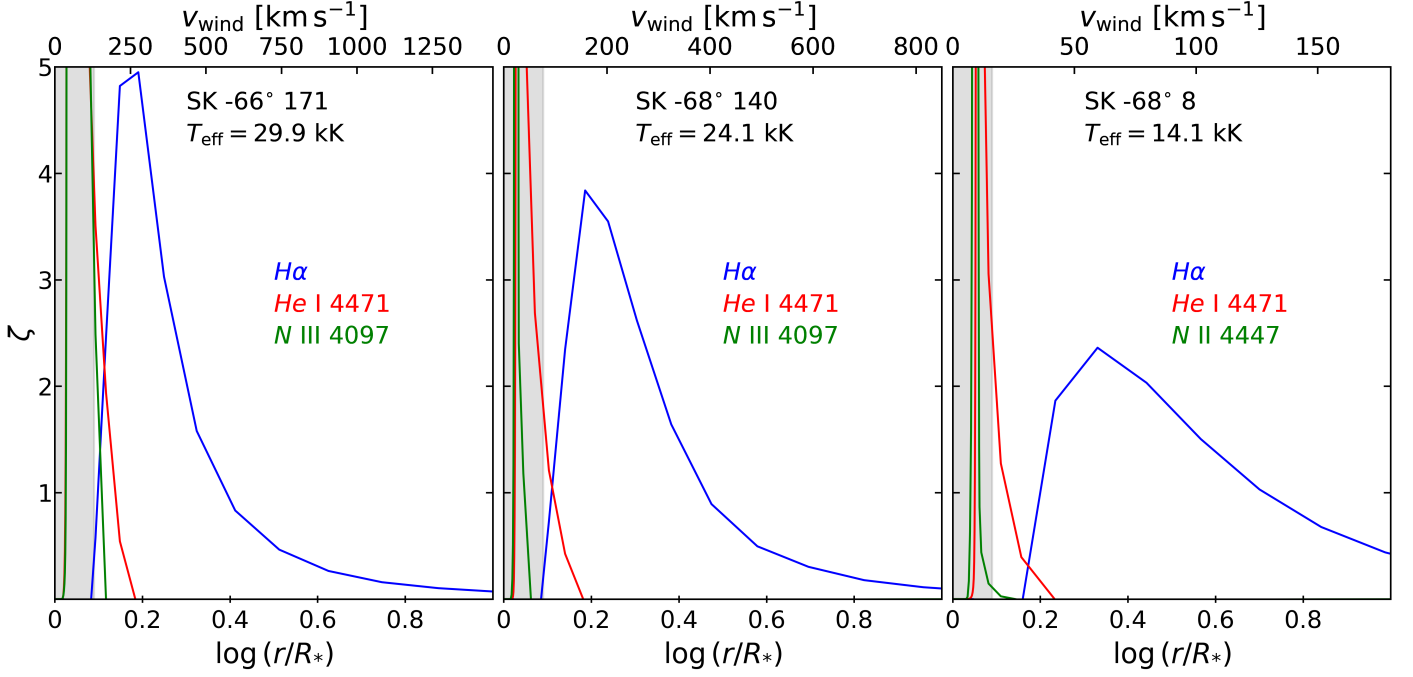
Fig. 15: Line formation region (ζ versus $\log(r/R_*)$) of Hα (blue solid line), He I λ4471 (red solid line), and a line from the dominating nitrogen ion (green solid line), for Sk $-66°$ 171 ($T_{\rm eff}$ = 29.9 kK, left panel), Sk $-68°$ 140 ($T_{\rm eff}$ = 24.1 kK, middle panel), and Sk $-68°$ 8 ($T_{\rm eff}$ = 14.1 kK, right panel). The grey shaded region indicates the photosphere.
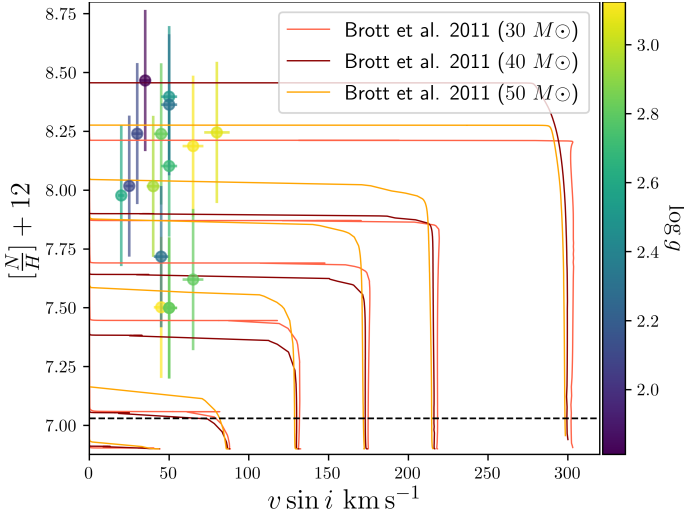

Fig. 16: Nitrogen abundance (by number) versus $v_{\rm rot}\sin i$. The colour scheme corresponds to the value of $\log g$, and the evolutionary tracks are computed for initial masses of 30 $M_\odot$, 40 $M_\odot$ and 50 $M_\odot$ (red, brown, and orange solid lines respectively) for initial rotational velocities of 50, 110, 170, 220, 270 380 km s^{-1} (Brott et al. 2011), which we multiplied by a factor of $\pi/4$ to take into account the inclination of the rotation axis (Hunter et al. 2008). The black dashed line represents the LMC baseline nitrogen abundance.

(green solid lines) form around $v_{\rm wind} \approx 10-15$ km s^{-1}, which coincides with the transition point between the subsonic and supersonic regimes, connecting the photosphere to the inner region of the stellar winds. On the topmost panels of Fig. 17, the transition point is where the velocity jumps from 0 km s^{-1} to ≈ 15 km s^{-1}.

From Fig. 16, we see that one could reproduce the overall distribution of our sample's observed nitrogen enhancement via evolutionary tracks that include rotational mixing (Brott et al. 2011). However, extremely high initial rotational velocities do not agree with what is observed for O-stars and the findings of Ramírez-Agudelo et al. (2013), who obtained the rotational properties of a large sample of LMC O-stars (216 stars), and concluded that the distribution of $v_{\rm rot}\sin i$ peaks at ≈ 80 km s^{-1}. We also do not find a clear positive correlation between rotation rates and nitrogen enhancement which is similar to the findings of Hunter et al. (2008).

In Fig. 18, we present the logarithm number ratios N/C and N/O of our sample (blue circles). Maeder et al. (2014) analytically obtains the upper and lower bounds (black dashed lines) from nuclear constaints (^{12}C is turned immediately into ^{14}N and the number of carbon atoms is constant throughout the CNO cycle) on the the changes of N/C versus N/O ratios during the CNO cycle. We find that the majority of our stars are within those bounds. The exception are the stars Sk $-71°$ 41, Sk $-67°$ 5, Sk $-68°$ 52, Sk $-68°$ 140, which fall outside of the boundaries, but are within the uncertainties. In Fig. 18, we divide the stars into groups following the criteria introduced by Menon et al. (2024), who obtains the CNO abundances of 59 early B-supergiants in the LMC using FASTWIND. We find that only Sk $-71°$ 41 is part of *Group 1*, which is the group whose number ratios can be explained by a single star evolutionary scenario. *Group 2*, whose number ratios can be obtained via blue loop models, fast rotating ($v_{\rm init,rot}$ = 220km s^{-1}) TAMS models, or merger models. The rest of the sample falls within *Group 3*, the number ratios of which can only be explained by merger scenarios.

Although it is expected for the combined mass fraction of CNO elements of any given star in our sample to stay constant throughout its evolution and to be similar to that of the LMC,
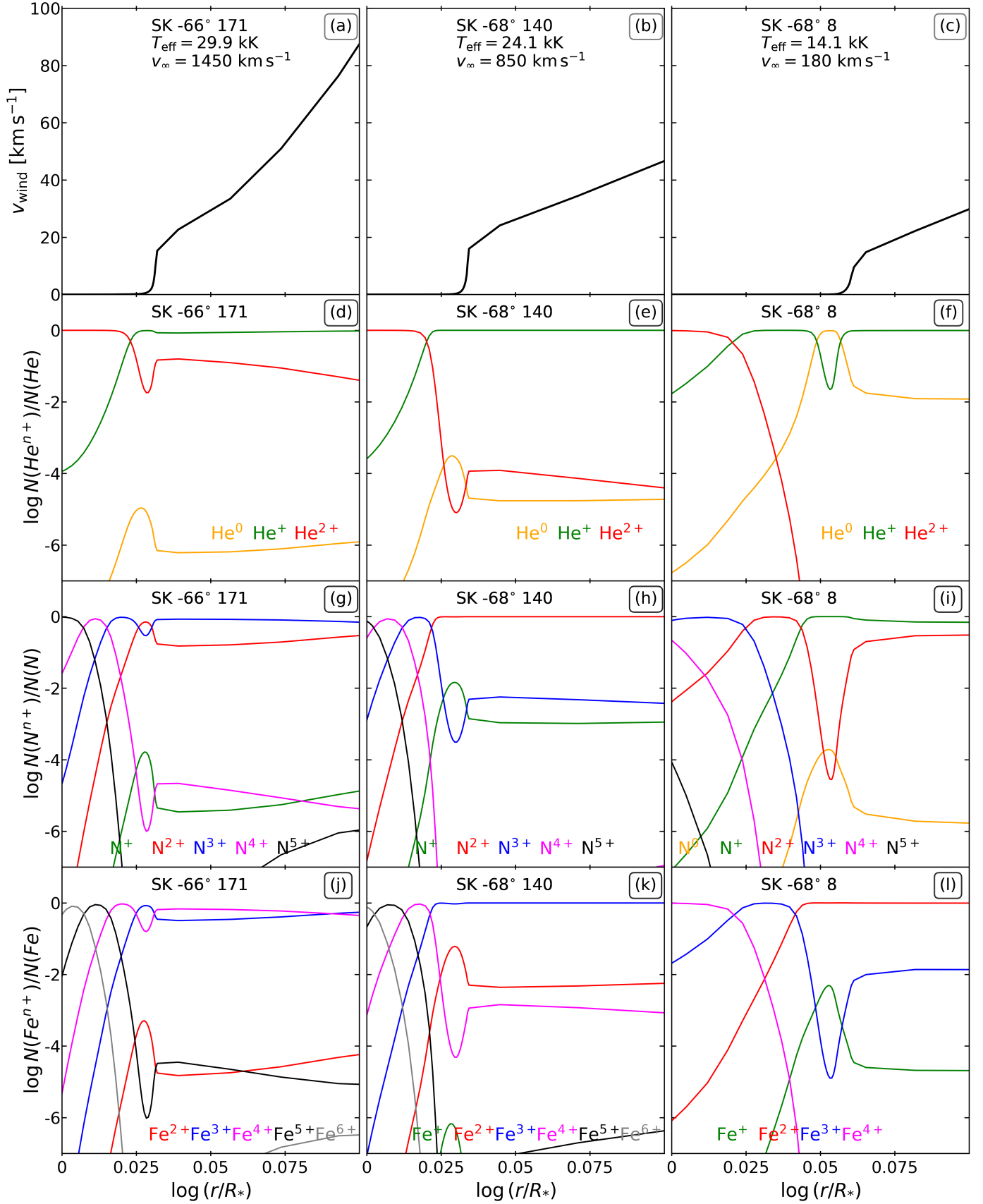
Fig. 17: Each column, from left to right, adheres to Sk −66° 171 ($T_{\rm eff}$ = 29.9 kK), Sk −68° 140 ($T_{\rm eff}$ = 24.1 kK), and Sk −68° 8 ($T_{\rm eff}$ = 14.1 kK), respectively. *a*, *b*, and *c*: Wind verlocity as a fucntion of radius in stellar radii units $\log(r/R_*)$. *d*, *e*, and *f*: ionization structure (relative ionic density $\log(N(i^{n+})/N(i_{\rm tot}))$ versus $\log(r/R_*)$) of helium. *g*, *h*, *i*: Ionization structure of nitrogen. *j*, *k*, and *l*: Ionization structure of iron. i^0 (orange), i^+ (green), i^{2+} (red), i^{3+} (blue), i^{4+} (magenta), i^{5+} (black), i^{6+} (grey) where i is the element.
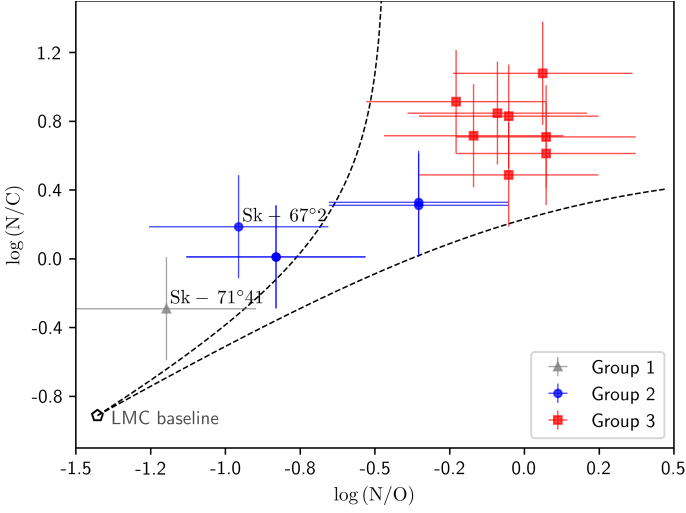
Fig. 18: log N/C versus log N/O of our sample (grey triangles, blue circles, and red squares). The upper and lower boundry (dashed black lines) are adopted from Maeder et al. (2014). The sample is divided into three groups depending on their N/C and N/O values similar to Menon et al. (2024).

we do find that, in some cases, the aggregate CNO mass fraction required to obtain a satisfactory fit to the designated CNO lines significantly diverges from the baseline CNO mass fraction of the LMC (ΣCNO/ΣCNO$_{LMC}$ in Table 8). The most extreme examples of this are Sk −71° 41 and Sk −69° 279, with ratios of summed CNO mass fraction to LMC CNO mass fraction of $\approx$ 1.7 and 0.6, respectively, indicating that these objects have a respectively higher and lower cumulative CNO mass fraction. This likely arises from the sensitivity of abundances to other parameters, mainly $T_{\rm eff}$, log g. Fixing $v_{\rm mic}$, as explained in Section 3.4.4, could be a contributing factor to this discrepancy.

5. Discussion

In Section 5.1 we discuss the existence of the bi-stability jump in our sample. In Section 5.2 we compare our results to previous empirical studies. In Section 5.3, we compare our results to various numerical predictions. Finally, in Section 5.4 we explore the dependence of wind properties on metallicity.

5.1. Do we spot a bi-stability jump?

The main goal of this study is to explore the existence of the numerical mass-loss rate jump-like increase when going from the 'hot' regime to the 'cool' regime around $T_{\rm eff}$ = 25 kK. We attempted to alleviate the degeneracy of mass-loss and clumping that plagues the recombination line emission in Hα by utilising the appropriate unsaturated P Cygni lines in the UV as previously mentioned. Fig. 19 shows our derived wind efficiency parameter ($\eta = \frac{\dot{M}v_\infty}{L_{\rm bol}/c}$) vs $T_{\rm eff}$. We see a clear downward trend in the overall sample. This is in agreement with Benaglia et al. (2007), who derive the mass-loss rates for a sample of Galactic OB-stars from thermal radio emission and find a similar monotonic downward trend in wind efficiency with lower temperatures.

In Fig. 20, we compare the distribution of $v_\infty/v_{\rm esc}$ versus $T_{\rm eff}$ to empirical predictions from Lamers et al. (1995) (MW) and Hawcroft et al. (2024) (LMC), plus the $v_{\rm esc}$-$T_{\rm eff}$ prediction from Krtička et al. (2021) which does not assume a bi-stability jump,
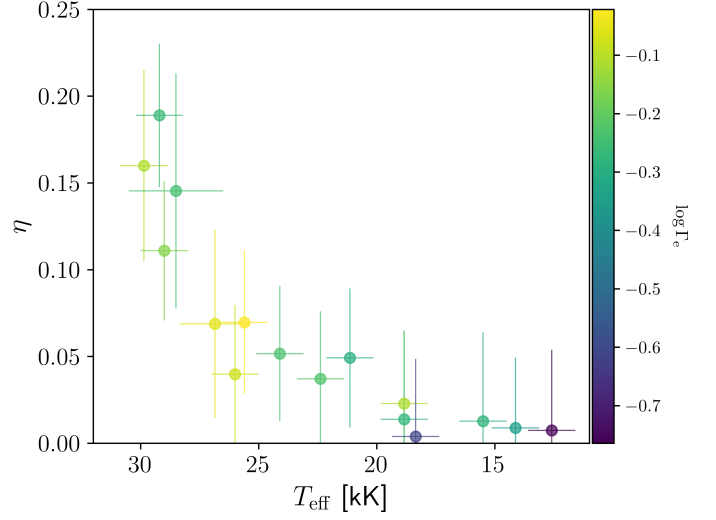

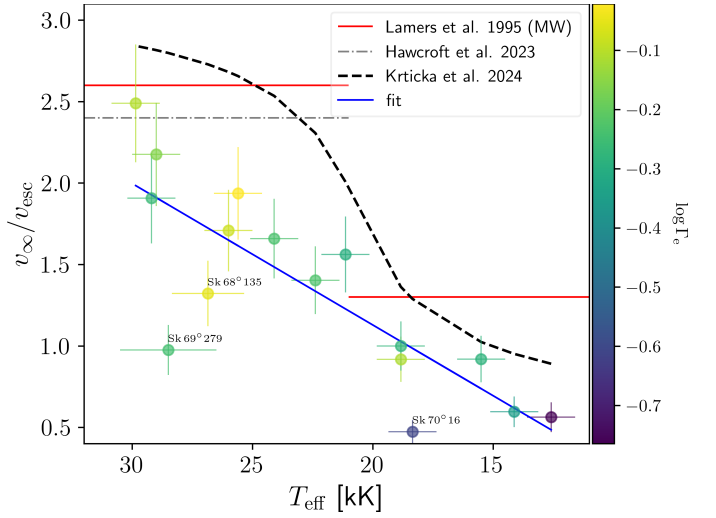Fig. 19: wind efficiency ($\eta = \frac{\dot{M}v_\infty}{L_{\rm bol}/c}$) in terms of effective temperature.

Fig. 20: The ratio ($v_\infty/v_{\rm esc}$) as a function of temperature. The yellow dashed line is the relation presented in Krtička et al. (2021). The filled red lines represent the ratios from Lamers et al. (1995). The green filled line is the average relation for stars of spectral type earlier than B1 from Hawcroft et al. (2024). The color gradient correlates to the value of Γ_e.

but rather a smooth transition from high to low ratios. For our sample, we see a smooth decline in $v_\infty/v_{\rm esc}$ with lower temperatures and do not see any signs of a bi-stability jump around the proposed $T_{\rm eff}$ $\approx$ 25−21 kK. Although the Krtička et al. (2021) recipe produces a smooth decrease in $v_\infty/v_{\rm esc}$, our results do not match their prediction. The outliers are the hypergiants Sk −68° 135 and Sk −69° 279, which have low $v_\infty/v_{\rm esc}$. This is due to abnormally slow winds relative to other objects with similar temperatures.

The vertical error bars in Fig. 20 include the uncertainties of v_∞ and the $v_{\rm esc}$. With a simple linear fit we obtain the relation:

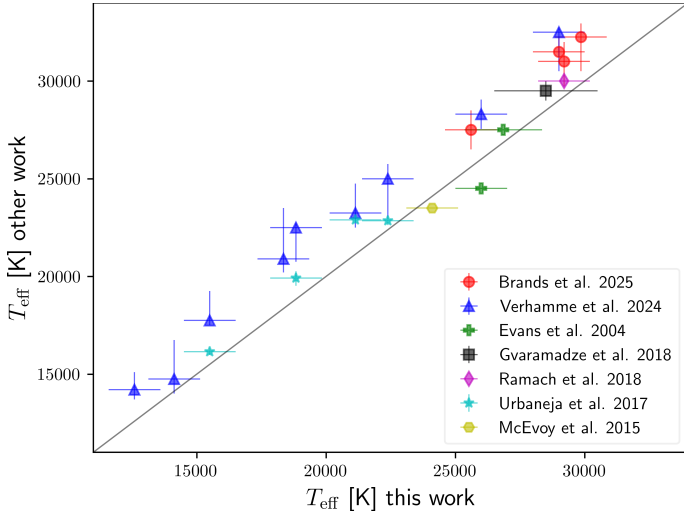$$v_\infty/v_{\rm esc} = 4.1(\pm0.8)\log(T_{\rm eff}/{\rm K}) - 16.3(\pm3.5). \quad (8)$$

Fig. 21: Comparison of our obtained $T_{\rm eff}$ to previous studies. on the x-axis we present our effective temperature for each star and on the y-axis is the the comparison $T_{\rm eff}$ from previous analysis. Blue triangles: Comparison to values obtained by Verhamme et al. (2024), Red circles: Comparison to values obtained by Brands et al. (2025). Green filled crosses: Comparison to values obtained by Evans et al. (2004). Black square: Comparison to values obtained by Gvaramadze et al. (2018). Magenta diamond: Comparison to values obtained by Ramachandran et al. (2018). Cyan star: Our $T_{\rm eff}$ to the effective temperatures from Urbaneja et al. (2017). Yellow hexagon: Comparison to values obtained by McEvoy et al. (2015).
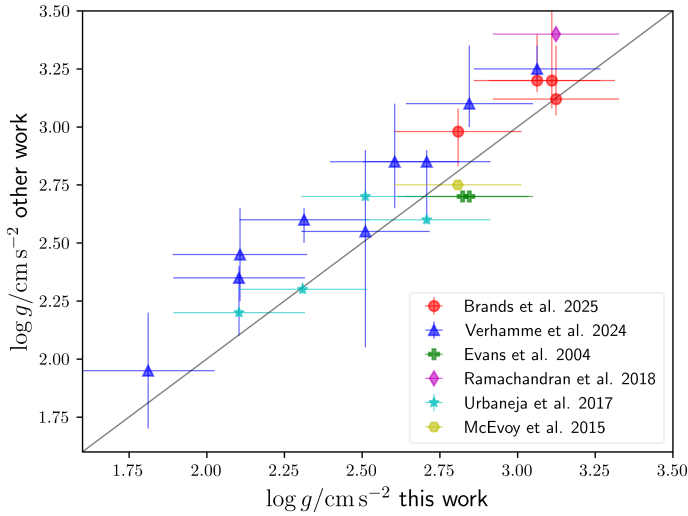
Fig. 22: Comparison of our obtained $\log g$ to previous studies. The symbols follow the same encoding as in Fig. 21.

5.2. Comparison to previous empirical studies

Due to differences in radiative transfer codes, in analysis methods and in observational datasets, and above all the lack of a clear unified methodology for calculating model and true uncertainties, we are not comparing like-for-like. The reason for the comparison is to check if the collection of those comparison studies produce an observable bi-stability jump.

Sander et al. (2024) concludes that an average maximum spread in $T_{\rm eff}$, $\log g$, and $\log \dot{M}$ obtained with different methods applied to ULYSSES/XshootU data is $\Delta T_{\rm eff} \approx 3000$ kK,
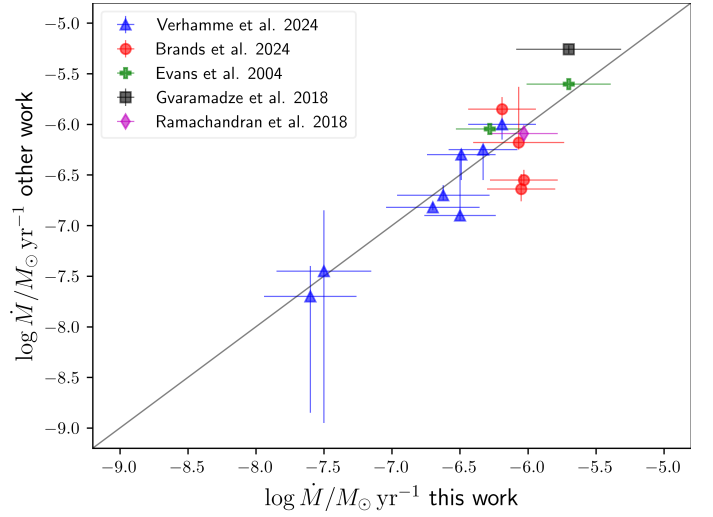

Fig. 23: Comparison of our derived $\dot{M}$ to previous studies. The symbols follow the same encoding as in Fig. 21.
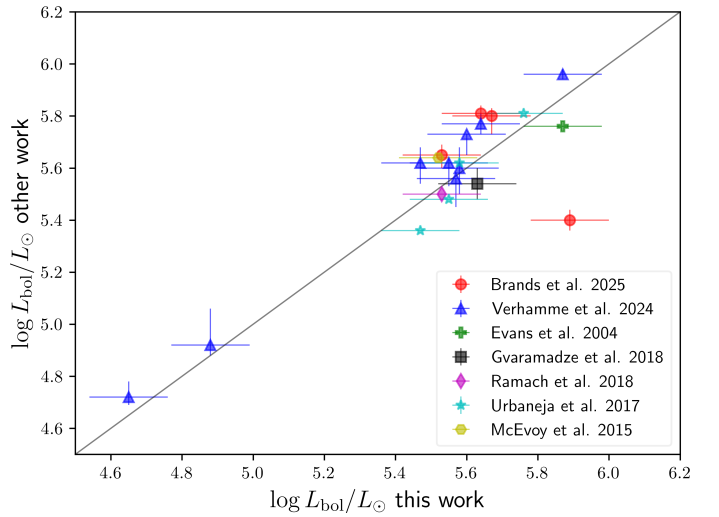

Fig. 24: Comparison of our derived $\log L_{\rm bol}$ to previous studies. The symbols follow the same encoding as in Fig. 21.

$\Delta \log (g/{\rm cm\,s^{-2}}) \approx 0.2$ and $\Delta \log (\dot{M}/{\rm M_\odot\,yr^{-1}}) \approx 0.4$. While the analysis conducted by Sander et al. (2024) is very revealing of the discrepancies between the different radiative transfer codes and a great attempt at parametrizing the spread that could be expected when comparing results obtained by these codes, the sample was limited to two LMC and one SMC O-type stars. Therefore, the spread of parameters obtained in that study is not significant from a statistical point of view.

In this section, we focus on comparing $T_{\rm eff}$, $\log g$, and $\log \dot{M}$. in Sections 5.2.1 and 5.2.2, when comparing the mass-loss rates, we do not adjust the values to the equivalent "smoothed wind" values (for $f_{\rm vol} = 1$).

Fig. 21-24 compare our derived values of $T_{\rm eff}$, $\log g$, $\dot{M}$, and $\log L_{\rm bol}$ respectively, versus values derived in previous studies. We compile our derived $T_{\rm eff}$, $\log g$, $\log \dot{M}$, $\log L_{\rm bol}$, β, and $f_{\rm vol}$ alongside the results of various previous empirical studies in Table F.1 in Appendix F.

5.2.1. UV + Optical studies

Evans et al. (2004) has two targets in common with the present study, also employed CMFGEN. Their T_{eff} for the hypergiant Sk −68° 135 is 1500 K lower than ours and a T_{eff} for Sk −68° 52 is 800 K higher than our estimate, whereas their $\log g$ is lower than ours by 0.15 dex and 0.12 dex respectively. They provide two mass-loss rates for each object, one with the assumption of a smooth wind, and the other with the assumption of a generic volume filling factor of 0.1, and we compare our mass-loss rates to the latter and we find that their mass-loss rates are higher by 0.23 dex and 0.10 dex for Sk −68° 52 and Sk −68° 135 respectively. This can be attributed to the difference in photospheric parameters, the difference in β-law, which they assume is 2.75 and 3.50 respectively for Sk −68° 52 and Sk −68° 135, versus our β that we estimate at 2 and 2.3, and most significantly the large difference in the terminal wind velocity estimates, as we determine the wind velocities at 1140 km s^{-1} and 880 km s^{-1}, versus their v_∞ of 1400 km s^{-1} and 1350 km s^{-1} for Sk −68° 52 and Sk −68° 135, respectively, which they measure from the N III λ991 doublet in the FUV FUSE range. The luminosities obtained by Evans et al. (2004) are consistent within 0.1 dex of our luminosities.

We share Sk −71° 41 in common with Ramachandran et al. (2018), who analysed a large sample of OB-stars in the LMC N206 superbubble using the Potsdam Wolf–Rayet (PoWR) code (Gräfener et al. 2002b; Hamann & Gräfener 2003b; Sander et al. 2015). Their T_{eff} is slightly higher than ours (see Table F.1), but we do find a large discrepancy in $\log g$, where they estimate it to be $\approx$ 0.3 dex higher than ours. The source of this observed discrepancy is unclear but could be the due to the difference in datasets. The mass-loss rate obtained by them is consistent with our mass-loss rates, albeit slightly lower.

We have seven targets in common with Verhamme et al. (2024) and four targets with Brands et al. (2025), who conducted a UV+optical analysis for B-supergiants and hot O-supergiants, respectively, using the genetic algorithm Kiwi-GA, which utilises FASTWIND non-LTE radiative transfer models. Both of these studies used the same spectroscopic dataset as this study (ULLYSES/XShootU dataset). We find that our effective temperatures is systematically lower than those of Verhamme et al. (2024) and Brands et al. (2025) by 1000 − 4000 K (see Fig. 21). This could be attributed to the differences between CMFGEN and FASTWIND in the treatment of helium and silicon lines (Massey et al. 2013), and the different analysis methods (genetic algorithm vs manual by-eye fitting).

For the coolest star Sk −67° 195, Verhamme et al. (2024) obtained the temperature through the He I and Si II lines, whereas we obtain our temperature from fitting the He I and Mg II lines. FASTWIND suffferce from known convergence problems below 15 kK (Lorenzo et al. 2025), therefore CMFGEN is more reliable. The higher temperatures of Verhamme et al. (2024) and Brands et al. (2025) lead to higher $\log g$ in comparison to our work. We find that that our effective surface gravities are 0.1 − 0.25 dex lower than theirs (see Fig. 22). The luminosities obtained by Verhamme et al. (2024) and Brands et al. (2025) are systematically higher than ours by $\Delta L_{bol} = 0.02 − 0.12$ dex, albeit they are consistent within the uncertainties. The sole outlier is Sk −67° 5, for which the lumiosity derived by Brands et al. (2025) is lower than ours by approximately $\Delta \log L_{bol} = 0.5$ dex. This arises from adopting incorrect UBV photometry by Brands et al. (2025). The use of the correct photometry yields $\log L_{bol} = 6.00^{+0.04}_{-0.04}$ for Sk −67° 5 (Brands et al. 2025, priv. comm.), which is in better agreement with our derived luminos-

ity of $\log L_{bol} = 5.89$. We do not notice any trend in the difference between our mass-loss rates and those obtained by Verhamme et al. (2024) and Brands et al. (2025) despite the different clumping parametrization. We do note that mass-loss rates from Verhamme et al. (2024) and Brands et al. (2025) are consistent with our mass-loss rates within the uncertainties.

The advantages of our analysis methods compared to Verhamme et al. (2024) are the detailed treatment of line blanketing in the UV provided in CMFGEN (see Fig. 2 and Appendix H), the robust velocity measurements from P Cygni profiles in the UV, and the employment of Mg II 4481 when measuring the temperature of the coolest B-supergiants where Si III lines are no longer present. The main disadvantages of our method are the lack of robust calculations of statistical model errors. Also, unlike FASTWIND, the treatment of clumping in CMFGEN is limited to micro-clumping, which, in some cases, yields poor fits to the red emission in P Cygni profiles, and requires unrealialisticly low volume-filling factors (or high clumping factors) to obtain good fits for the blue absorption. Muijres et al. (2011) describes how optically-thin clumps increase the predicted mass-loss rates, while the optically-thick clumps can display an opposite effect. This might have a differential effect on object at either side of the bi-stability jump. This effect was recently explored by de Burgos et al. (2024a) in a large sample of Galactic OB-stars, and they report a lack of evidence for a bi-stability jump. In this study, as in Verhamme et al. (2024) and Brands et al. (2025), we do not find a correlation between the mass-loss rate and the clumping parameters.

5.2.2. Optical only studies

Sk −68° 140 is in common with McEvoy et al. (2015), who obtained the atmospheric parameters and nitrogen abundances for a B-supergiants in the LMC using TLUSTY and SYNSPEC codes (Hubeny & Lanz 1995b). We find that our T_{eff} and $\log g$ are slightly higher compared to theirs (500 K and 0.05 dex respectively), which falls well within our uncertainties. The model grids they use are plane-parallel and do not provide a measure of the mass-loss rate.

We share 4 targets in common with Urbaneja et al. (2017), which is a photometric and spectroscopic (optical only) study for LMC OB-supergiants using FASTWIND. We find that, the effective temperatures are systematically larger than ours by 500 − 1500 K, whereas for $\log g$ we do not identify any systematic trend. Since Urbaneja et al. (2017) conducted their study to specifically explore the gravity–luminosity relationship, mass-loss rates are not investigated. We find that our T_{eff} and $\log g$ are consistent with theirs within the uncertainties. We calculate $\log L_{bol}$ from the total extinction values, bolometric corrections and apparent magnitudes provided in Urbaneja et al. (2017). We find that they are in agreement with our derived $\log L_{bol}$ within the uncertainties.

Gvaramadze et al. (2018) performed a detailed optical only spectroscopic analysis using CMFGEN for the hypergiant Sk −69° 279. In comparison to our effective temperature and mass-loss rate, theirs are larger by 700 K and 0.4 dex, respectively. The difference in mass-loss is due to the difference in wind clumping, as they estimate f_{vol} at 0.5 versus 0.1 in our analysis and β-law, which they fix at a value of 3, whereas we estimate a value of $\beta = 2.7$. The different observational data used in Gvaramadze et al. (2018) and the variable nature of this object, which ressembles a dormant Luminous Blue Variable (LBV, Weis et al. 1997), could also be a contributing factor to this discrepancy. Gvaramadze et al. (2018) do not provide the effective surface
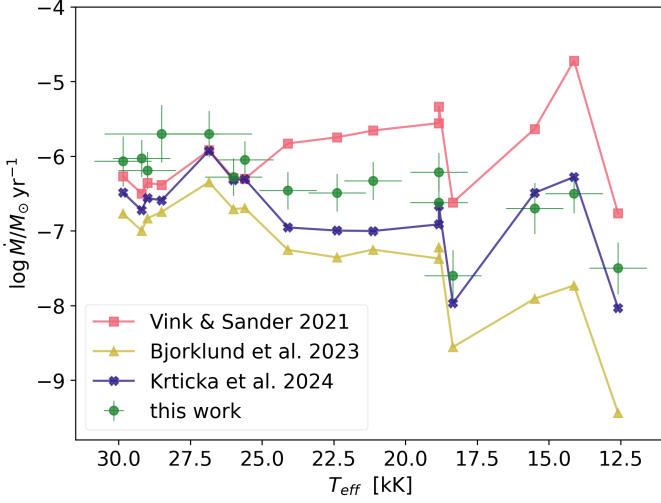
Fig. 25: Mass-loss rates as a function of T_{eff}, comparing our derived $\dot{M}$ (green circles) to mass-loss rates which we calculated via various numerical recipes. Pink squares: $\dot{M}$ from Vink et al. (2001) recipe. Yellow triangles: $\dot{M}$ from Björklund et al. (2023). Violet crosses: $\dot{M}$ from Krtička et al. (2024).
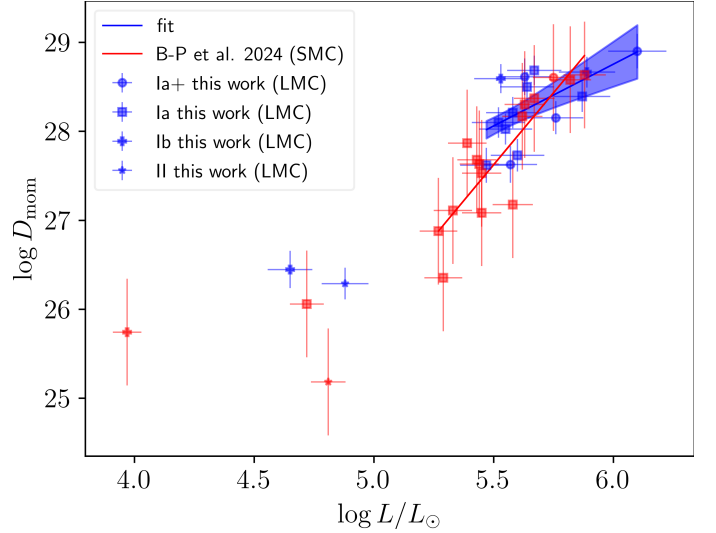
Fig. 26: Modified wind momentum-luminosity distribution of LMC (blue symbols) supergiants from this work and SMC (red symbols) supergiants from Bernini-Peron et al. (2024). Objects with $\log (L_{bol}/L_\odot) < 5$ are excluded from the linear fits for both the LMC and SMC samples. The symbols for the SMC sample (red) follow the same encoding of the LMC sample (blue), where each luminosity class is given a unique symbol.

gravity used in their models therefore we cannot compare our results.

Comparing our results to Bestenlehner et al. (2025), we find that there is a good agreement in the T_{eff} and $\log g$. The exception to this are the late-O hypergiants Sk $-68°$ 135 and Sk $-69°$ 279, where we find large differences in temperature and gravity. The discrepancy in T_{eff} is likely due the weak He II $\lambda 4686$ line, the region of which is clearly offset from the continuum (see Fig. H.3). Additionally, all Balmer lines utilised by the pipeline in Bestenlehner et al. (2025) present heavy wind contamination (fully or partially in emission), making $\log g$ hard to constrain. Subsequently, all the parameters obtained from fitting those lines are not reliable. Unlike other FASTWIND based studies, we do not notice a clear offset in T_{eff} and $\log g$. We find no major discrepancies in the luminosities. Despite the constant $\beta = 1$ and $f_{vol} = 0.1$ in the grid that was utilised by the pipeline of Bestenlehner et al. (2025), their derived mass-loss rates are consistent with ours within the uncertainties.

5.3. Comparison to numerical mass-loss rate recipes

Here, we compare our derived mass-loss rates to those predicted by numerical recipes presented in Vink et al. (2001), Björklund et al. (2023), and Krtička et al. (2024). The mass-loss rate recipe produced by Vink et al. (2001) is based on predictions from unified Monte-Carlo models with consistency between radiative acceleration and mechanical acceleration in the overall structure of the wind. The prediction of the bi-stability jump and the mass-loss rates around $T_{eff} = 25 - 21$ kK in those simulations is due to the recombination of Fe IV into Fe III which has significantly more spectral lines resulting in a "boost" in line-driving. In the bottommost row of Fig. 17, it is clear the dominant iron ions at the connection point marking the photosphere in Sk $-66°$ 171, Sk $-68°$ 140, and Sk $-68°$ 8 are Fe V, Fe IV, and Fe III, respectively. This means that the shift from Fe IV to Fe III is indeed reflected in our results, with Fe III providing the majority of line-driving (Petrov et al. 2016), but as we discuss later, this is not accompanied by an increase in empirical mass-loss rates. Petrov

et al. (2016) explore another bi-stability jump at $T_{eff} \approx 10-8$ kK, which was discussed by Lamers et al. (1995) and Vink et al. (1999). This bi-stability jump is due to the change in ionization balance between Fe III and Fe II, with Fe II becoming the source of most of the line acceleration.

An important element in the calculation routine is the ratio of terminal velocity to escape velocity (v_∞/v_{esc}). For this, we adopt the v_∞ introduced in later study (Vink & Sander 2021). In Björklund et al. (2021, 2023), a locally self-consistent wind model FASTWIND that solves the radiative transfer equation in the co-moving frame is used. In this case, no sudden increase in the mass-loss rate is produced with decreasing T_{eff}. In this recipe, the mass-loss rates decrease as a smooth function of stellar parameters. Finally, in Krtička et al. (2024) the mass-loss rates are derived using global stellar atmosphere code METUJE that was introduced in Krtička & Kubát (2017), which calculates the velocity stratification with the radiative acceleration. This recipe predicts a much more moderate increase in the mass-loss rates compared to what is predicted by Vink et al. (2001) in the regime bellow $T_{eff} = 20$ kK.

Fig. 25 compares our derived mass-loss rates with the predicted mass-loss rates calculated by numerical recipes assuming $Z/Z_\odot = 0.5$. We notice that for stars with temperatures above 25 kK, the Vink et al. (2001) and Krtička et al. (2024) mass-loss rate predictions are relatively consistent with our derived mass-loss rates. For stars cooler that 25 kK our derived mass-loss rates are situated between Vink et al. (2001) and Krtička et al. (2024) favouring the latter in values and overall trend. Predictions from Björklund et al. (2023) have a similar trend to those from Krtička et al. (2024), but are consistently lower by ≈ 1 dex. The dip in the mass-loss rates in our results and in all predictions between $T_{eff} = 18 - 15$ kK is due to the object Sk $-70°$ 16 not being a B4 blue supergiant (Ib), but rather a lower luminosity bright giant.

Table 9: Slopes x, and offsets, $\log D_0$, of the linear fits to modified wind momentum equation (Equation 9) of this study, Mokiem et al. (2007), and Backs et al. (2024)

LMC	x	$\log D_0$
This study	1.39 ± 0.54	20.4 ± 3.0
Mokiem et al. (2007)	1.49 ± 0.18	20.4 ± 1.0
Backs et al. (2024)	1.87 ± 0.11	18.03 ± 1.2

5.4. Metallicity effect

To explore the metallicity dependence of wind properties, we derive the modified wind momentum D_{mom}-L_{bol} relation ($D_{\mathrm{mom}} = \dot{M} v_\infty R_*/R_\odot$) (Kudritzki et al. 1995; Kudritzki & Puls 2000), and we limit our fit to stars with $\log(L_{\mathrm{bol}}/L_\odot) > 5$. For lower luminosity stars the mass-loss rates we obtain are less reliable and can be considered upper limits due to Hα being fully in absorption and due to the lack of reliable P Cygni profiles for wind velocity measurements. We fit our derived values using a D_{mom}-L_{bol} relation of the form:

$$\log D_{\mathrm{mom}}^{\mathrm{LMC}} = x \log(L_{\mathrm{bol}}/L_\odot) + \log D_0 \qquad (9)$$

From Table 9, we find that our derive relation in good alignment with the clumping-scaled relationship derived by Mokiem et al. (2007) for LMC OB-stars. Our D_{mom}-L_{bol} relation is consistent with the findings of Backs et al. (2024) within the uncertainties, however they obtain a steeper relation from an LMC sample that consists mostly of O giants and bright giants, and incorporates results from Brands et al. (2025).

We also compare our results to those of Bernini-Peron et al. (2024), the latest detailed ULLYSES/XshootU spectroscopic analysis of an SMC B-supergiant sample using CMFGEN. The main differences between our results and those of Bernini-Peron et al. (2024) is that, whereas we include late O-stars, their sample is composed from B-stars exclusively. Their method differs from ours in that X-rays are included and v_{mic} is a free parameter that is determined in their fitting procedure, which could lead to different temperature determination due to the change in opacity, which effects the depth of silicon lines. Higher v_{mic} at larger radii in the wind could potentially also lead to underestimating v_∞.

In Fig. 26, we compare our derived D_{mom}-L_{bol} relation to that of Bernini-Peron et al. (2024). When fitting the results of their SMC sample we obtain:

$$\log D_{\mathrm{mom}}^{\mathrm{SMC}} = 3.24(\pm0.50) \log(L_{\mathrm{bol}}/L_\odot) + 9.8(\pm2.8).$$

There is a clear difference in the slope and vertical offset between the linear fit of the two samples, but unlike the findings of Mokiem et al. (2007), the two fits greatly vary, which is not something predicted by previous studies exploring the metallicity dependence of wind properties in the LMC and SMC for neither O or B-stars (e.g. Crowther et al. (2006); Mokiem et al. (2007); Backs et al. (2024)). Excluding low luminosity objects, the sample of Bernini-Peron et al. (2024) spans a range of $\log L_{\mathrm{bol}}/L_\odot \approx 5.2 - 5.9$, compared to the range of our sample $\log L_{\mathrm{bol}}/L_\odot \approx 5.5 - 6.1$. Also, the sample of Bernini-Peron et al. (2024) is composed of almost exclusively Ia supergiants, inferring a selection bias to strong winds, whereas our sample contains supergiants spanning Ib to Ia$^+$. Those differences in the samples could be a major contributing factor to the difference in the dependence of the slope on metallicity compared to previous studies.

6. Summary and conclusions

In this paper, we have applied a quantatative analysis using CMFGEN models to LMC late-O- and B-supergiants, which we will also use in future analysis of SMC (ULLYSES/XshootU) and Milky Way samples. We have also compared our results to previous works, and we found that when taking into account the differences in analysis methods and quality of data, our parameters are mostly consistent with those previously derived within expected systematic variance, which is discuseed in Sander et al. (2024).

We found that our sample consists of evolved stars. The majority of the sample are main-sequence stars with a few post-main sequence stars, according to the rotating single-star evolutionary models of Brott et al. (2011). We find that some of the stars in our sample apear to be evolved and in the post main sequence stage. Our derived spectroscopic masses are broadly consistent with the evolutionary masses obtained from Bonnsai (Schneider et al. 2014) within the uncertainties. Our results did not show the large mass discrepancy that was reported in previous studies (e.g., Herrero et al. 1992; Trundle et al. 2004; Crowther et al. 2006) (Schneider et al. 2018).

We obtained a velocity-temperature relation:

$$v_\infty/\mathrm{km\,s^{-1}} = 0.076(\pm0.011)T_{\mathrm{eff}}/\mathrm{K} - 884(\pm260),$$

which is in agreement with the relation obtinaed by Hawcroft et al. (2024). We also derived a wind momentum-luminosity relation:

$$\log D_{\mathrm{mom}}^{\mathrm{LMC}} = 1.39(\pm0.54) \log(L_{\mathrm{bol}}/L_\odot) + 20.4(\pm3.0),$$

which is very similar to the relation obtained for OB-stars in the LMC by Mokiem et al. (2007).

We investigated the existence of the bi-stability jump, and we found that there is a lack of observational evidence in our sample that would support such a boost in line-driving, hence mass-loss and momentum, despite the shift from Fe IV to Fe III. This is in agreement with the analysis of Verhamme et al. (2024), who conducted an analysis of a ULLUSES/XShootU LMC sample. This also agrees with the results of de Burgos et al. (2024a), who did not find an increase in the mass-loss rates over the bi-stability region in a large sample of Galactic blue supergiants. Our findings also support the results of Bernini-Peron et al. (2024), who did not detect a bi-stability jump in their sample of SMC blue supergiants.

Our results showed a strong correlation between $v_\infty/v_{\mathrm{esc}}$ and T_{eff}, and we obtained the relation:

$$v_\infty/v_{\mathrm{esc}} = 4.1(\pm0.8) \log(T_{\mathrm{eff}}/\mathrm{K}) - 16.3(\pm3.5).$$

We did not find evidence of a sharp drop in $v_\infty/v_{\mathrm{esc}}$, which could be attributed to the shift from the low density and high velocity wind regime to the high density and low velocity regime associated with the bi-stability jump (Pauldrach & Puls 1990; Lamers et al. 1995; Vink et al. 2001; Petrov et al. 2016)

By comparing our results to a similar CMFGEN-based analysis of SMC BSGs (Bernini-Peron et al. 2024), we found strong evidence of a Z-dependence of wind momentum. This supports previous findings and line-driving wind theory predictions. In this paper, we did not establish metallicity dependent mass-loss or momentum recipes. We elected to produce those empirical recipes in a future paper where we will conduct our own analysis of SMC and MW OB-supergiants.

In future studies we will include stars of the same spectral range and analysis methods. This is to ensure that we are comparing like-for-like across different environments and that the results for each sample can be compared to the others without inherent differences in methodology. Our goal is to produce an empirical recipe for the mass-loss rates for blue supergiants, which connects the mass-loss rates to other environmental (metallicity) and intrinsic (temperature, mass, etc,..) parameters of the star. This, in turn, can be added as input for evolutionary models (Yoon et al. 2006) and population synthesis models (Leitherer et al. 1999) that currently rely on numerical mass-loss rate recipes such as the one proposed in Vink et al. (2001). Such an empirical mass-loss recipe would provide an important counterpart gauged by observations. Moreover, since the recipe would be produced by applying the same ethods of analysis to samples in different enviroments, the obtained Z-dependence would be more robust.

References

Alves, D. R. 2004, New A Rev., 48, 659
Anderson, L. S. 1985, ApJ, 298, 848
Anderson, L. S. 1989, ApJ, 339, 558
Ardeberg, A., Brunet, J. P., Maurice, E., & Prevot, L. 1972, A&AS, 6, 249
Asplund, M., Grevesse, N., & Sauval, A. J. 2005, in Astronomical Society of the Pacific Conference Series, Vol. 336, Cosmic Abundances as Records of Stellar Evolution and Nucleosynthesis, ed. T. G. Barnes, III & F. N. Bash, 25
Backs, F., Brands, S. A., de Koter, A., et al. 2024, A&A, 692, A88
Baum, E., Hamann, W. R., Koesterke, L., & Wessolowski, U. 1992, A&A, 266, 402
Beckman, J. E. & Crivellari, L. 1985, Science, 230, 835
Benaglia, P., Vink, J. S., Martí, J., et al. 2007, A&A, 467, 1265
Bernini-Peron, M., Marcolino, W. L. F., Sander, A. A. C., et al. 2023, A&A, 677, A50
Bernini-Peron, M., Sander, A. A. C., Ramachandran, V., et al. 2024, A&A, 692, A89
Bestenlehner, J. M., Crowther, P. A., Caballero-Nieves, S. M., et al. 2020, MNRAS, 499, 1918
Bestenlehner, J. M., Crowther, P. A., Hawcroft, C., et al. 2025, A&A, 695, A198
Bestenlehner, J. M., Enßlin, T., Bergemann, M., et al. 2024, MNRAS, 528, 6735
Bestenlehner, J. M., Gräfener, G., Vink, J. S., et al. 2014, A&A, 570, A38
Björklund, R., Sundqvist, J. O., Puls, J., & Najarro, F. 2021, A&A, 648, A36
Björklund, R., Sundqvist, J. O., Singh, S. M., Puls, J., & Najarro, F. 2023, A&A, 676, A109
Brands, S. A., Backs, F., de Koter, A., et al. 2025, A&A, 697, A54
Brands, S. A., de Koter, A., Bestenlehner, J. M., et al. 2022, A&A, 663, A36
Bresolin, F., Kudritzki, R.-P., Mendez, R. H., & Przybilla, N. 2001, ApJ, 548, L159
Brott, I., de Mink, S. E., Cantiello, M., et al. 2011, A&A, 530, A115
Butler, K. & Giddings, J. 1985, University of London
Choudhury, S., Subramaniam, A., & Cole, A. A. 2016, MNRAS, 455, 1855
Cioni, M. R., Clementini, G., Girardi, L., et al. 2011, The Messenger, 144, 25
Crowther, P. A. 2019, Galaxies, 7, 88
Crowther, P. A. 2024, in IAU Symposium, Vol. 361, IAU Symposium, ed. J. Mackey, J. S. Vink, & N. St-Louis, 15–25
Crowther, P. A., Hillier, D. J., Evans, C. J., et al. 2002, ApJ, 579, 774
Crowther, P. A., Lennon, D. J., & Walborn, N. R. 2006, A&A, 446, 279
Cutri, R. M., Skrutskie, M. F., van Dyk, S., et al. 2003, VizieR Online Data Catalog: 2MASS All-Sky Catalog of Point Sources (Cutri+ 2003), VizieR On-line Data Catalog: II/246. Originally published in: University of Massachusetts and Infrared Processing and Analysis Center, (IPAC/California Institute of Technology) (2003)
de Burgos, A., Keszthelyi, Z., Simón-Díaz, S., & Urbaneja, M. A. 2024a, A&A, 687, L16
de Burgos, A., Simón-Díaz, S., Urbaneja, M. A., & Negueruela, I. 2023, A&A, 674, A212
de Burgos, A., Simón-Díaz, S., Urbaneja, M. A., & Puls, J. 2024b, A&A, 687, A228
Debnath, D., Sundqvist, J. O., Moens, N., et al. 2024, A&A, 684, A177
Dessart, L. & Hillier, D. J. 2010, MNRAS, 405, 2141
Dopita, M. A., Seitenzahl, I. R., Sutherland, R. S., et al. 2019, AJ, 157, 50
Evans, C. J., Crowther, P. A., Fullerton, A. W., & Hillier, D. J. 2004, ApJ, 610, 1021
Fitzpatrick, E. L. 1985, ApJ, 299, 219
Fitzpatrick, E. L. & Massa, D. 1990, ApJS, 72, 163
Fouesneau, M. 2025, pyphot
Geen, S., Agrawal, P., Crowther, P. A., et al. 2023, PASP, 135, 021001
Gordon, K. D., Clayton, G. C., Misselt, K. A., Landolt, A. U., & Wolff, M. J. 2003, ApJ, 594, 279
Gräfener, G., Koesterke, L., & Hamann, W. R. 2002a, A&A, 387, 244
Gräfener, G., Koesterke, L., & Hamann, W. R. 2002b, A&A, 387, 244
Green, J. C., Froning, C. S., Osterman, S., et al. 2012, ApJ, 744, 60
Gvaramadze, V. V., Kniazev, A. Y., Maryeva, O. V., & Berdnikov, L. N. 2018, MNRAS, 474, 1412
Haiman, Z. & Loeb, A. 1997, ApJ, 483, 21
Hamann, W. R. & Gräfener, G. 2003a, A&A, 410, 993
Hamann, W. R. & Gräfener, G. 2003b, A&A, 410, 993
Haucke, M., Cidale, L. S., Venero, R. O. J., et al. 2018, A&A, 614, A91
Hawcroft, C., Sana, H., Mahy, L., et al. 2024, A&A, 688, A105
Herrero, A., Kudritzki, R. P., Vilchez, J. M., et al. 1992, A&A, 261, 209
Herrero, A., Puls, J., & Najarro, F. 2002, A&A, 396, 949
Hillier, D. J. 1990, A&A, 231, 116
Hillier, D. J. 1996, in Liege International Astrophysical Colloquia, Vol. 33, Liege International Astrophysical Colloquia, ed. J. M. Vreux, A. Detal, D. Fraipont-Caro, E. Gosset, & G. Rauw, 509
Hillier, D. J. 1997, in IAU Symposium, Vol. 189, IAU Symposium, ed. T. R. Bedding, A. J. Booth, & J. Davis, 209–216
Hillier, D. J., Lanz, T., Heap, S. R., et al. 2003, ApJ, 588, 1039
Hillier, D. J. & Miller, D. L. 1998, ApJ, 496, 407
Hillier, D. J. & Miller, D. L. 1999, ApJ, 519, 354
Hubeny, I. & Lanz, T. 1995a, ApJ, 439, 875
Hubeny, I. & Lanz, T. 1995b, ApJ, 439, 875
Hunter, I., Brott, I., Lennon, D. J., et al. 2008, ApJ, 676, L29
Hunter, I., Dufton, P. L., Smartt, S. J., et al. 2007, A&A, 466, 277
Korn, A. J., Nieva, M. F., Daflon, S., & Cunha, K. 2005, ApJ, 633, 899
Krtička, J. & Kubát, J. 2017, A&A, 606, A31
Krtička, J., Kubát, J., & Krtičková, I. 2021, A&A, 647, A28
Krtička, J., Kubát, J., & Krtičková, I. 2024, A&A, 681, A29
Kudritzki, R. P., Bresolin, F., & Przybilla, N. 2003, ApJ, 582, L83
Kudritzki, R. P., Lennon, D. J., & Puls, J. 1995, in Science with the VLT, ed. J. R. Walsh & I. J. Danziger, 246
Kudritzki, R.-P. & Puls, J. 2000, ARA&A, 38, 613
Kudritzki, R.-P., Urbaneja, M. A., Bresolin, F., et al. 2024, ApJ, 977, 217
Kudritzki, R.-P., Urbaneja, M. A., Bresolin, F., et al. 2008, ApJ, 681, 269
Kurucz, R. L. 1979, ApJS, 40, 1
Lamers, H. J. G. L. M., Snow, T. P., & Lindholm, D. M. 1995, ApJ, 455, 269
Langer, N. 2012, Annual Review of Astronomy and Astrophysics, 50, 107
Langer, N. & Kudritzki, R. P. 2014, A&A, 564, A52
Lanz, T. & Hubeny, I. 2007, ApJS, 169, 83
Leitherer, C., Schaerer, D., Goldader, J. D., et al. 1999, ApJS, 123, 3
Lorenzo, M., Garcia, M., Castro, N., et al. 2025, MNRAS, 537, 1197
Maeder, A., Przybilla, N., Nieva, M.-F., et al. 2014, A&A, 565, A39
Marcolino, W. L. F., Bouret, J. C., Martins, F., et al. 2009, A&A, 498, 837
Markova, N., Puls, J., Scuderi, S., & Markov, H. 2005, A&A, 440, 1133
Martins, F. 2011, Bulletin de la Societe Royale des Sciences de Liege, 80, 29
Martins, F., Mahy, L., Hillier, D. J., & Rauw, G. 2012, A&A, 538, A39
Massa, D., Prinja, R. K., & Oskinova, L. M. 2024, ApJ, 971, 166
Massey, P. 2002, ApJS, 141, 81
Massey, P., Neugent, K. F., Hillier, D. J., & Puls, J. 2013, ApJ, 768, 6
McErlean, N. D., Lennon, D. J., & Dufton, P. L. 1998, A&A, 329, 613
McErlean, N. D., Lennon, D. J., & Dufton, P. L. 1999, A&A, 349, 553
McEvoy, C. M., Dufton, P. L., Evans, C. J., et al. 2015, A&A, 575, A70
Menon, A., Ercolino, A., Urbaneja, M. A., et al. 2024, ApJ, 963, L42
Mokiem, M. R., de Koter, A., Vink, J. S., et al. 2007, A&A, 473, 603
Moos, H. W., Cash, W. C., Cowie, L. L., et al. 2000, ApJ, 538, L1
Muijres, L. E., de Koter, A., Vink, J. S., et al. 2011, A&A, 526, A32
Müller, P. E. & Vink, J. S. 2008, A&A, 492, 493

Negueruela, I., Simón-Díaz, S., de Burgos, A., Casasbuenas, A., & Beck, P. G. 2024, A&A, 690, A176

Pauldrach, A. W. A., Kudritzki, R. P., Puls, J., Butler, K., & Hunsinger, J. 1994, A&A, 283, 525

Pauldrach, A. W. A. & Puls, J. 1990, A&A, 237, 409

Petrov, B., Vink, J. S., & Gräfener, G. 2016, MNRAS, 458, 1999

Prinja, R. K., Barlow, M. J., & Howarth, I. D. 1990, ApJ, 361, 607

Przybilla, N., Butler, K., Becker, S. R., & Kudritzki, R. P. 2006, A&A, 445, 1099

Przybilla, N., Nieva, M.-F., & Butler, K. 2008, ApJ, 688, L103

Puebla, R. E., Hillier, D. J., Zsargó, J., Cohen, D. H., & Leutenegger, M. A. 2016, MNRAS, 456, 2907

Puls, J., Kudritzki, R. P., Herrero, A., et al. 1996, A&A, 305, 171

Puls, J., Urbaneja, M. A., Venero, R., et al. 2005, A&A, 435, 669

Puls, J., Vink, J. S., & Najarro, F. 2008, A&A Rev., 16, 209

Ramachandran, V., Hamann, W. R., Hainich, R., et al. 2018, A&A, 615, A40

Ramírez-Agudelo, O. H., Simón-Díaz, S., Sana, H., et al. 2013, A&A, 560, A29

Repolust, T., Puls, J., & Herrero, A. 2004, A&A, 415, 349

Rivero González, J. G., Puls, J., & Najarro, F. 2011, A&A, 536, A58

Rivero González, J. G., Puls, J., Najarro, F., & Brott, I. 2012, A&A, 537, A79

Roman-Duval, J., Fischer, W. J., Fullerton, A. W., et al. 2025, arXiv e-prints, arXiv:2504.05446

Sana, H., Tramper, F., Abdul-Masih, M., et al. 2024, A&A, 688, A104

Sander, A., Shenar, T., Hainich, R., et al. 2015, A&A, 577, A13

Sander, A. A. C., Bouret, J. C., Bernini-Peron, M., et al. 2024, A&A, 689, A30

Schmidt-Kaler, T., Gochermann, J., Oestreicher, M. O., et al. 1999, MNRAS, 306, 279

Schmutz, W., Hamann, W. R., & Wessolowski, U. 1989, A&A, 210, 236

Schneider, F. R. N., Langer, N., de Koter, A., et al. 2014, A&A, 570, A66

Schneider, F. R. N., Ramírez-Agudelo, O. H., Tramper, F., et al. 2018, A&A, 618, A73

Searle, S. C., Prinja, R. K., Massa, D., & Ryans, R. 2008, A&A, 481, 777

Simón-Díaz, S. 2020, in Reviews in Frontiers of Modern Astrophysics; From Space Debris to Cosmology, 155–187

Simón-Díaz, S. & Herrero, A. 2014, A&A, 562, A135

Skrutskie, M. F., Cutri, R. M., Stiening, R., et al. 2006, AJ, 131, 1163

Smartt, S. J. 2009, ARA&A, 47, 63

Smith, N. 2014, ARA&A, 52, 487

Smith, R. K., Brickhouse, N. S., Liedahl, D. A., & Raymond, J. C. 2001, ApJ, 556, L91

Sota, A., Maíz Apellániz, J., Walborn, N. R., et al. 2011, ApJS, 193, 24

Stanway, E. R. & Eldridge, J. J. 2018, MNRAS, 479, 75

Trundle, C. & Lennon, D. J. 2005, A&A, 434, 677

Trundle, C., Lennon, D. J., Puls, J., & Dufton, P. L. 2004, A&A, 417, 217

Urbaneja, M. A., Herrero, A., Bresolin, F., et al. 2005a, ApJ, 622, 862

Urbaneja, M. A., Herrero, A., Kudritzki, R. P., et al. 2005b, ApJ, 635, 311

Urbaneja, M. A., Kudritzki, R. P., Gieren, W., et al. 2017, AJ, 154, 102

Verhamme, O., Sundqvist, J., de Koter, A., et al. 2024, A&A, 692, A91

Vernet, J., Dekker, H., D'Odorico, S., et al. 2011, A&A, 536, A105

Vink, J. S., de Koter, A., & Lamers, H. J. G. L. M. 1999, A&A, 350, 181

Vink, J. S., de Koter, A., & Lamers, H. J. G. L. M. 2000, A&A, 362, 295

Vink, J. S., de Koter, A., & Lamers, H. J. G. L. M. 2001, A&A, 369, 574

Vink, J. S., Mehner, A., Crowther, P. A., et al. 2023, A&A, 675, A154

Vink, J. S., Muijres, L. E., Anthonisse, B., et al. 2011, A&A, 531, A132

Vink, J. S. & Sander, A. A. C. 2021, MNRAS, 504, 2051

Weis, K., Chu, Y. H., Duschl, W. J., & Bomans, D. J. 1997, A&A, 325, 1157

Weßmayer, D., Przybilla, N., & Butler, K. 2022, A&A, 668, A92

Weßmayer, D., Przybilla, N., Ebenbichler, A., Aschenbrenner, P., & Butler, K. 2023, A&A, 677, A175

Woodgate, B. E., Kimble, R. A., Bowers, C. W., et al. 1998, PASP, 110, 1183

Yoon, S. C., Langer, N., & Norman, C. 2006, A&A, 460, 199

Appendix A: Omitted objects

Sk −69° 83   For this star, we find a sign of binarity in He II $\lambda4686$, where it is blue shifted relative to all the other lines, indicating the existence of an emission from a primary hotter object combined with the emission of a cooler object. We also find signs of two components in He II $\lambda5411$ and Hγ

Sk −67° 197, Sk −66° 152, Sk −67° 168, Sk −70° 50   These objects were omitted from the analysis due to Hα and He II $\lambda4686$ having two symmetrical emission peaks with a narrow absorption feature in the line center which is indicative of a non-spherically symmetric geometry such as a circumstellar disk.

Sk −66° 50   The spectrum of this object showed clear binary signatures in the form of double peaked absorption in Hβ, Hϵ and Hγ in addition to the odd morphology of Hα.

Appendix B: Comments on individual stars

Sk −66° 171, Fig. G.1, Fig. H.1   When considering helium lines other than He I $\lambda4471$ He II $\lambda4542$, one might prefer a model with a slightly higher temperature. The other glaring issue is with the Hα, although the morphology of the model line is similar to the observation, we do find that the centre of the emission in the observation is slightly red shifted relative to all other lines. In the UV and FUV the model fits the observations very well. Fig. H.1 shows the fit for the entire spectrum, where for this object include a fit for the absorption profiles for $Ly\alpha$ through $Ly\eta$, which were calculated using H I column density log $N(HI) = 20.7$ cm^{-2} (Fitzpatrick 1985). The observed He II $\lambda4686$ emission is predicted in absorption.

Sk −68° 155, Fig. G.2, Fig. H.2   This star with $v \sin i$ = 80 km/s is the fastest rotator in our sample, which is reflected in the relatively broad metal and helium lines. The small dip in the centre of the emission in Hα could be an indication of an optically thick disk forming around the star, other than that the overall quality of the fit is very good. The model overpredicts the He II $\lambda4686$ absoprtion.

Sk −69° 279, Fig. G.3, Fig. H.3   This is one of two hypergiants in our sample, which is classified as such by the extremely strong emission in Hα and the P Cygni shape in higher Balmer lines and in He I $\lambda4471$, therefore, we use Hη for estimating log g, as all other Balmer lines are contaminated by winds and take He I $\lambda4026$ and He II $\lambda5411$ as primary diagnostics to obtain the temperature. The overall fit is quite good considering all the challenges that come with fitting the spectra of emission line objects, with the exception of He II $\lambda4686$ line, where the predicted emission is weaker than the observed.

Sk −71° 41, Fig. G.4, Fig. H.4   For this object, we were not able to reproduce the observed unsaturated silicon lines Si IV $\lambda\lambda1393 − 1403$ even with models with extremely clumped winds $f_{vol} = 0.03 − 0.02$. We note two other peculiarities, first of which is the large discrepancy between v_∞ obtained from the C IV $\lambda\lambda1548 − 1551$ (≈ 1500 km s^{-1})and Si IV $\lambda\lambda1394 − 1403$ (≈ 1300 km s^{-1}). The other peculiarity is the unexplicably broad O III $\lambda5592$ line.

Sk −68° 135, Fig. G.5, Fig. H.5   This is second hypergiant in our sample. Just as for Sk −69° 279, we estimate log g from Hη. But unlike the other hypergiant, we obtain a more reliable value for T_{eff} because the helium lines do are less contaminated by the extreme winds. We obtain decent fits for most lines, with the exception of the strong He II $\lambda4686$ emission, which is predicted in absorption in the model.

Sk −67° 5, Fig. G.6, Fig. H.6   For this object, we were not able to replicate the morphology of Hα. The most glaring issue in this fit is the helium abundance, and therefore the hydrogen abundance as well.

Sk −68° 52, Fig. G.7, Fig. H.7   This is one of the early B0 supergiants that shows weak He II lines. We chose not to fit He II lines, as increasing the temperature of the model by a mere 500 K does indeed give a better fit for He II lines but drastically weakens S III lines. Overall, we obtain an excellent fit for most lines.

Sk −69° 43, Fig. G.8, Fig. H.8   In the case of this object, as for Sk −67° 2, we were able to accurately reproduce the emission in Hα but not the braod, blueshifted absorption.

Sk −68° 140, Fig. G.9, Fig. H.9   The unsaturated Si IV $\lambda\lambda1393−1403$ lines, which suggests clumpier winds, were not reproduced by our models even with much smaller volum filling factors. The fit for this stars serves as a good example of the consequences of excluding X-rays from our models, as seen on Fig. H.9, the strong P Cygni C IV $\lambda1550$ in the observations is much weaker in the model, this is because in this temeperature range C III dominates the ionization structure, but due to X-rays generated by shocks, we observe the enhanced C IV line.

Sk −67° 2, Fig. G.10, Fig. H.10   The overall fit for this object is very good. In this case, we obtain a good fit for Hα emission, but we were unable to fit the blueshifted absorption.

Sk −67° 14, Fig. G.11, Fig. H.11   We notice on this object that Si IV $\lambda\lambda1393 − 1403$ would suggest less emissive winds (higher volume f_{vol}), whereas Al III $\lambda\lambda1856 − 1860$ would suggest more emissive winds (lower volume f_{vol}).

Sk −69° 52, Fig. G.12, Fig. H.12   For this star, we were not able to reproduce the odd morphology of Hα, which seem to have a sudden cut-off and the peak of the emission.

Sk −67° 78, Fig. G.13, Fig. H.13   The most noticeable issue with the fit of this object is the extended wings and the blue shifted absorption of the model Hα, which we could not eliminate. Although, we were able to obtain a good match to the emission in Hα.

Sk −70° 16, Fig. G.14, Fig. H.14   For this object we obtain a very good fit, except for Hα, where we could not reproduce the weak, but broad absorption.

Sk −68° 8, Fig. G.15, Fig. H.15   For this object, we were able to obtain a good fit for Hα emission and to the general morphology.

We do note the infilling of the Hγ line core, which could be due to nebular contamination. The Si II $\lambda\lambda6347 - 6371$ lines in the model match the observations quite well. This can be used as a sanity check for determining the effective temperature for mid and late B-supergiants.

Sk $-67°$ 195, Fig. G.16, Fig. H.16   For this low luminosity late B-supergiant we do not find any vaiable oxygen lines, therefore we do not change the oxygen mass fraction when applying our pipline to this star. We consider the mass-loss rate of this object to be an upper limit due to Hα being fully in absorption. We note that the predicted Si II $\lambda\lambda6347 - 6371$ lines excellently match the observed, albeit we did not use them as diagnostics.

Appendix C: v_{black} and v_{edge}

In Table C.1 we present the measured v_{black} from each line for all our sample. Similarly, in Table C.1 we present the measured v_{edge}.

Table C.1: v_{black} for the stars in our sample from all the available saturated P Cygni lines in the UV. Single velocity measurement from each line is subject to an uncertainty $\Delta v_{\text{black}} = 30\ \text{km s}^{-1}$ which take into acount the velocity resolution of the UV spectra and the uncertainty in the radial velocity correction which were added in quadrature.

Target	Si IV 1393	Si IV 1403	C IV 1548	Al III 1855	Al III 1863	Mg II 2796	Mg II 2803	$\overline{v_{\text{black}}}$
Sk −66° 171	1704	-	1846	-	-	-	-	1775±63
Sk −68° 155	-	1485	1482	-	-	-	-	1520±61
Sk −69° 279	613	640	-	-	-	-	-	630±62
Sk −71° 41	-	-	-	-	-	-	-	-
Sk −68° 135	855	909	-	-	-	-	-	880±62
Sk −67° 5	1231	-	1237	-	-	-	-	1230±61
Sk −68° 52	1050	1097	-	-	-	-	-	1150±61
Sk −69° 43	790	-	914	-	-	-	-	825±64
Sk −68° 140	1005	984	1016	-	-	-	-	1000±62
Sk −67° 2	377	361	-	384	381	-	-	380±61
Sk −67° 14	796	796	839	-	-	-	-	810±67
Sk −69° 52	473	457	-	-	-	-	-	465±61
Sk −67° 78	-	-	-	-	-	-	-	-
Sk −70° 16	-	-	-	-	-	-	-	-
Sk −68° 8	-	-	-	-	-	-	-	-
Sk −67° 195	-	-	-	-	-	218	211	215±62

Table C.2: v_{edge} for the stars in our sample from all the available P Cygni line profiles in the UV. Single velocity measurement from each line is subject to an uncertainty $\Delta v_{\text{edge}} = 30\ \text{km s}^{-1}$ which take into acount the velocity resolution of the UV spectra and the uncertainty in the radial velocity correction which were added in quadrature.

Target	Si IV 1393	Si IV 1403	C IV 1548	Al III 1855	Al III 1863	Mg II 2796	Mg II 2803	$\overline{v_{\text{black}}}/\overline{v_{\text{edge}}}$
Sk −66° 171	2135	-	2119	-	-	-	-	0.83
Sk −68° 155	1860	-	1799	-	-	-	-	0.81
Sk −69° 279	866	-	-	-	-	-	-	0.72
Sk −71° 41	1729	-	1737	-	-	-	-	-
Sk −68° 135	1247	-	1226	-	-	-	-	0.71
Sk −67° 5	1651	-	1629	-	-	-	-	0.75
Sk −68° 52	1583	1441	1581	-	-	-	-	0.75
Sk −69° 43	1059	1075	-	-	-	-	-	0.80
Sk −68° 140	1333	1419	1328	-	-	-	-	0.74
Sk −67° 2	-	505	-	465	464	-	-	0.79
Sk −67° 14	1005	1059	1081	-	-	-	-	0.77
Sk −69° 52	608	570	613	-	-	-	-	0.78
Sk −67° 78	473	-	441	-	-	-	-	-
Sk −70° 16	304	-	275	-	-	-	-	-
Sk −68° 8	256	258	262	255	257	-	-	-
Sk −67° 195	-	-	-	-	-	263	261	0.82

Appendix D: Atomic data

In Table D.1 we list the ions, number of important levels, super-levels, full levels, and transitions considered per ion, which constitutes the atomic model used in our CMFGEN model grid to synthesize the spectrum. The grid is split into two groups, with the boundry between the two is set at ≈ 25 kK.

Table D.1: Ions and number of important levels, super-levels, full levels, and transitions considered per ion, which constitutes the atomic model used by the code to synthesize the spectrum. We divide our model grid into a 'cool' ($< 25\,kK$) and a 'hot' ($> 25\,kK$) sections which correspond to different ions. "all" in the models column means that this ion has was included in both the hot and cool sections of our grid

Ion	important levels	super-levels	full levels	Transitions	models
H I	20	20	30	435	all
He I	45	45	69	905	all
He II	22	22	30	435	all
C I	52	52	100	10204	$< 25\,kK$
C II	40	40	92	8017	all
C III	51	51	84	5528	all
C IV	64	64	64	1446	all
C V	0	35	67	2196	$> 25\,kK$
N I	44	44	104	855	$< 25\,kK$
N II	45	45	85	7879	all
N III	104	104	164	6710	all
N IV	107	107	202	6943	all
N V	45	45	67	1664	$> 25\,kK$
O I	53	53	133	2138	$< 25\,kK$
O II	54	54	123	8937	all
O III	788	88	170	6561	all
O IV	78	78	154	7599	all
O V	32	32	56	2324	all
O VI	25	25	31	1475	$> 25\,kK$
Mg I	36	36	56	3511	$< 25\,kK$
Mg II	27	27	60	1993	all
Mg III	0	39	175	3052	all
Mg IV	0	36	169	5706	$> 25\,kK$
Ca I	0	66	88	3976	$< 25\,kK$
Ca II	0	39	46	1736	$< 25\,kK$
Ca III	0	29	88	3497	$< 25\,kK$
Ca IV	0	30	123	8532	$< 25\,kK$
Al I	54	54	82	4985	$< 25\,kK$
Al II	0	40	67	3490	$< 25\,kK$
Al III	0	37	60	2011	all
Al IV	0	56	163	3052	$> 25\,kK$
Si II	22	22	43	2294	all
Si III	33	33	33	1639	all
Si IV	22	22	33	1090	all
P III	0	59	128	5576	$> 25\,kK$
P IV	0	30	90	2537	$> 25\,kK$
P V	0	16	62	561	$> 25\,kK$
S II	0	21	65	8208	all
S III	0	24	44	6193	all
S IV	0	51	142	3598	all
S V	0	31	98	3462	all
Fe I	100	100	297	141821	$< 25\,kK$
Fe II	0	318	2430	21544	$< 25\,kK$
Fe III	104	104	1433	136060	all
Fe IV	74	74	540	72223	all
Fe V	50	50	220	71983	$> 25\,kK$
Fe VI	44	44	433	185392	$> 25\,kK$
Fe VII	29	29	153	86504	$> 25\,kK$
Ni II	0	42	433	51707	$< 25\,kK$
Ni III	0	46	849	66486	all
Ni IV	0	36	200	72898	all
Ni V	0	69	305	75541	$> 25\,kK$
Ni VI	0	65	314	79169	$> 25\,kK$

Appendix E: Spectral energy distribution (SED)

In Fig. E.1 we present the SED fits for the entire sample.
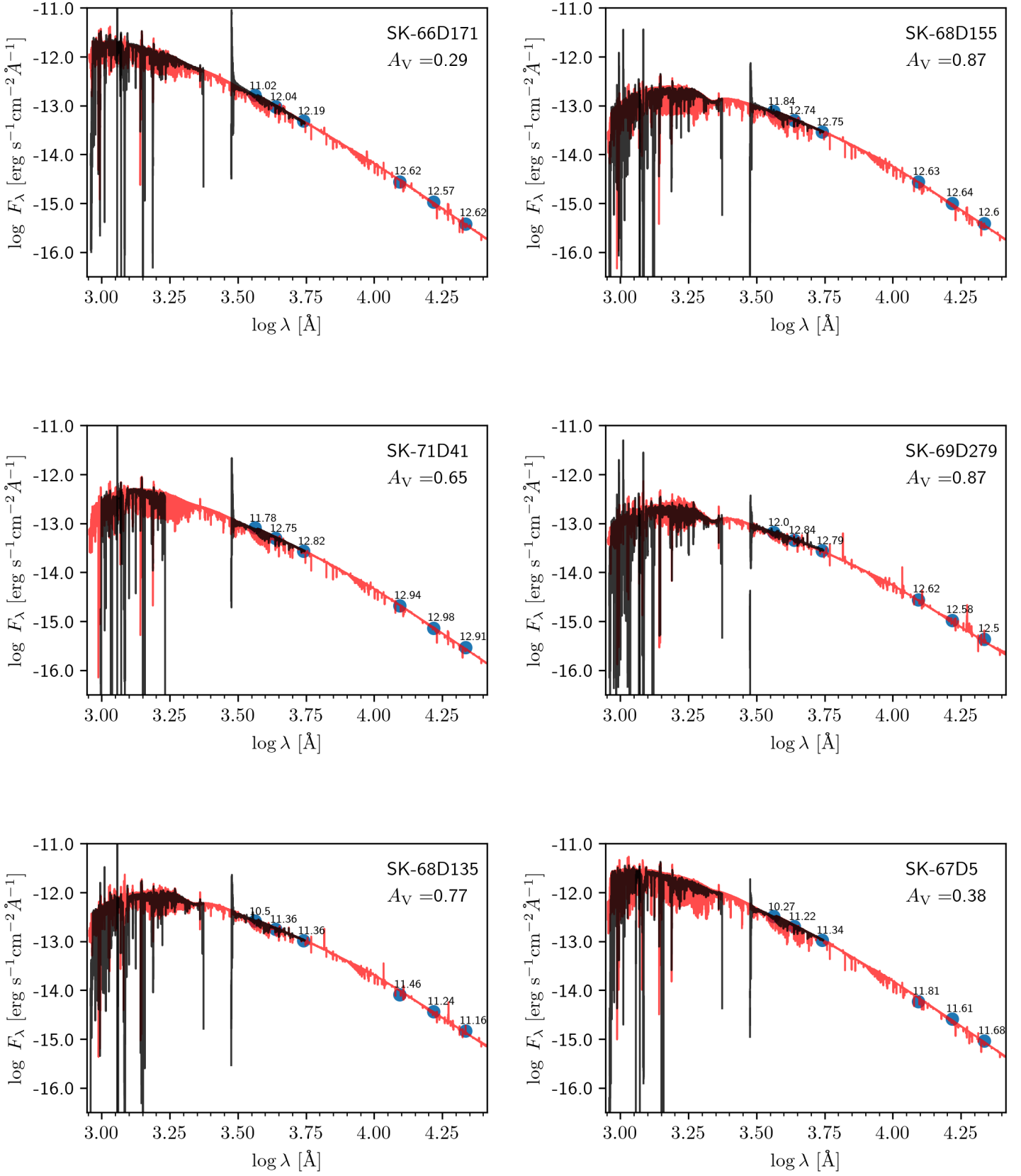
Fig. E.1: Spectral energy distribution for all the stars in our sample. Red solid line: model SED, Black solid line: observed SED. The photometric points are indicated as blue circles.
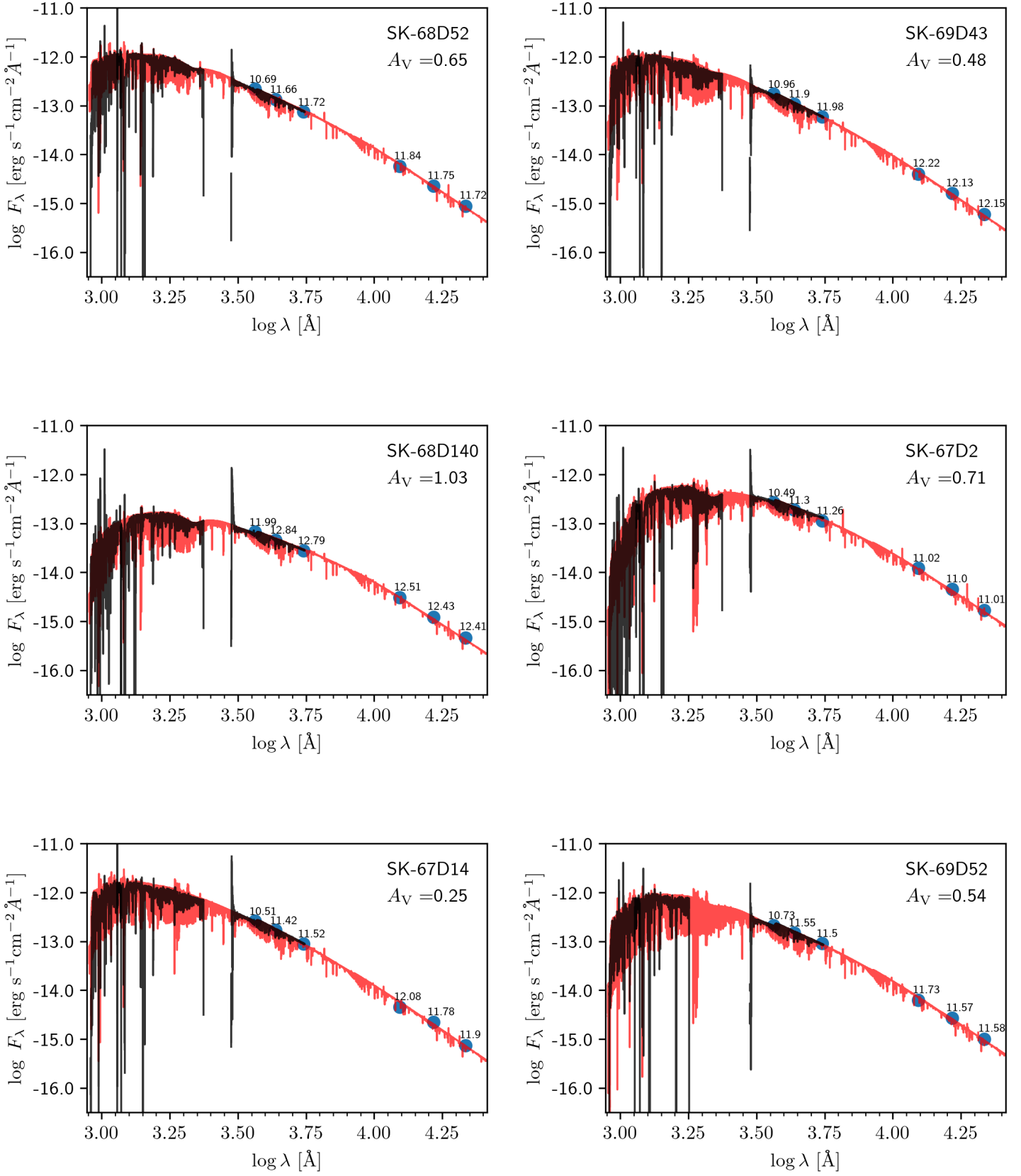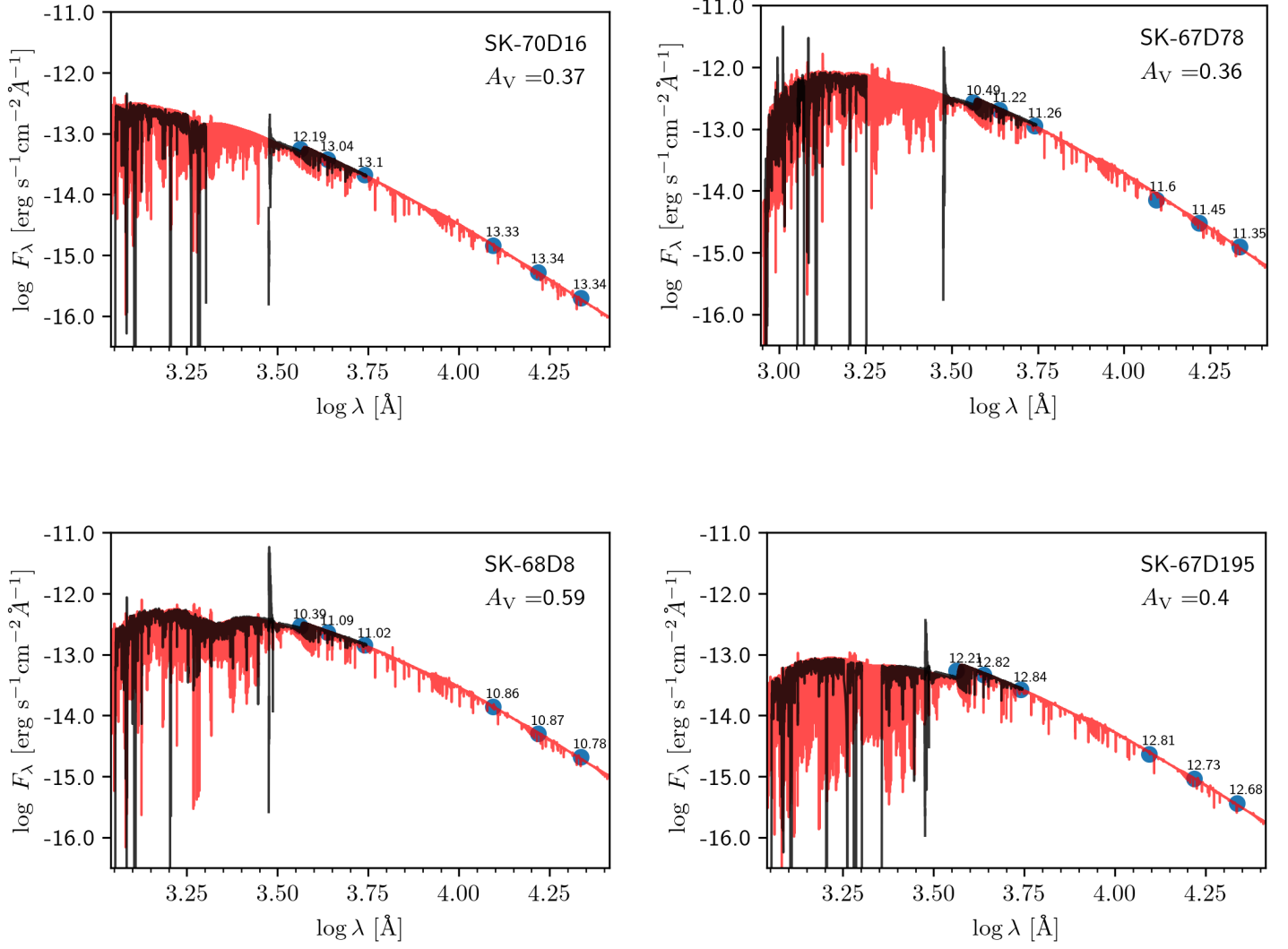
Fig. E.1: continued

Fig. E.1: continued

Appendix F: Comparison to literature

In this section, we include Table F.1, in which we present our obtained values for T_{eff}, $\log g$, $\log \dot{M}$, f_{vol}, and β in comparison to values presented in other previous studies. The volume filling factor for studies that utilise the optically-thick clumping is calculated from the equation introduced in Sander et al. (2024):

$$f_{\mathrm{vol}} = \frac{(1 - f_{\mathrm{ic}})^2}{f_{\mathrm{cl}} - 2 f_{\mathrm{ic}} + f_{\mathrm{ic}}^2}, \tag{F.1}$$

where $f_{\mathrm{cl}} = \langle \rho^2 \rangle / \langle \rho \rangle^2$ describes the contrast between the density in the clump and the mean density, and f_{ic} describes the contrast between the clump density and the density of the inter-clump medium.

Table F.1: Comparison of derived parameters to previous studies. Obtained using F: FASTWIND, P: PoWR, C: CMFGEN, T: TLUSTY. The mass-loss rates are not corrected for clumping.

Target Sk −	T_{eff} kK	$\log g$ cm s^{-1}	$\log L$ $L_\odot$	$\log \dot{M}$ $M_\odot\,\mathrm{yr}^{-1}$	f_{vol}	β	Ref.	wavelength	Code
66° 171	$29.9^{+1.2}_{-1.2}$	$3.12^{+0.14}_{-0.19}$	$5.66^{+0.08}_{-0.08}$	$-5.99^{+0.85}_{-0.23}$	0.1	1.00	JB25	Opt	F
	$32.3^{+0.70}_{-1.75}$	$3.20^{+0.47}_{-0.12}$	$5.80^{+0.03}_{-0.07}$	$-6.18^{+0.55}_{-0.07}$	0.0207	1.60	SB25	UV+Opt	F
	$29.9^{+1.0}_{-1.0}$	$3.11^{+0.20}_{-0.20}$	$5.67^{+0.11}_{-0.11}$	$-6.07^{+0.33}_{-0.33}$	0.03	1.70	This study	UV+Opt	C
68° 155	$29.9^{+1.2}_{-1.2}$	$3.12^{+0.14}_{-0.19}$	$5.70^{+0.08}_{-0.08}$	$-6.19^{+0.23}_{-0.23}$	0.1	1.00	JB25	Opt	F
	$31.5^{+0.75}_{-0.25}$	$3.20^{+0.20}_{-0.05}$	$5.81^{+0.03}_{-0.02}$	$-5.85^{+0.12}_{-0.10}$	0.0366	1.65	SB25	UV+Opt	F
	$32.5^{+0.25}_{-2.00}$	$3.25^{+0.10}_{-0.05}$	$5.77^{+0.04}_{-0.04}$	$-6.00^{+0.05}_{-0.15}$	0.0016	1.35	V24	UV+Opt	F
	$29.0^{+1.0}_{-1.0}$	$3.06^{+0.2}_{-0.2}$	$5.64^{+0.11}_{-0.11}$	$-6.19^{+0.25}_{-0.25}$	0.03	1.50	This study	UV+Opt	C
69° 279	$(15.1^{+0.4}_{-0.8})$	$(1.50^{+0.10}_{-0.00})$	$(2.37^{+0.07}_{-0.10})$	$(-7.75^{+0.30}_{-0.22})$	0.1	1.00	JB25	Opt	F
	$29.5^{+0.5}_{-0.5}$	-	$5.54^{+0.06}_{-0.06}$	$-5.26^{+0.04}_{-0.04}$	0.5	3.00	G18	UV+Opt	C
	$28.5^{+2.0}_{-2.0}$	$2.95^{+0.22}_{-0.22}$	$5.63^{+0.11}_{-0.11}$	$-5.70^{+0.39}_{-0.39}$	0.10	2.70	This study	UV+Opt	C
71° 41	$29.9^{+1.2}_{-1.2}$	$3.31^{+0.14}_{-0.14}$	$5.60^{+0.08}_{-0.08}$	$-6.22^{+0.23}_{-0.23}$	0.1	1.00	JB25	Opt	F
	$31.0^{+1.00}_{-1.25}$	$3.12^{+0.23}_{-0.07}$	$5.65^{+0.04}_{-0.05}$	$-6.55^{+0.10}_{-0.05}$	0.0190	2.90	SB25	UV+Opt	F
	$30.0^{+2.0}_{-2.0}$	$3.40^{+0.20}_{-0.20}$	$5.50^{+0.10}_{-0.10}$	$-6.09^{+0.10}_{-0.10}$	0.10	1.00	R18	UV+Opt	P
	$29.2^{+1.0}_{-1.0}$	$3.12^{+0.20}_{-0.20}$	$5.53^{+0.11}_{-0.11}$	$-6.03^{+0.25}_{-0.25}$	0.10	1.20	This work	UV+Opt	C
68° 135	$(22.3^{+0.8}_{-1.2})$	$(2.31^{+0.14}_{-0.14})$	$(5.09^{+0.08}_{-0.10})$	$(-5.94^{+0.30}_{-0.23})$	0.1	1.00	JB25	Opt	F
	27.5	2.70	6.97	-5.12	-	3.50	E04	UV+Opt	C
	$26.9^{+1.5}_{-1.5}$	$2.82^{+0.21}_{-0.21}$	$6.10^{+0.12}_{-0.12}$	$-5.70^{+0.31}_{-0.31}$	0.10	2.30	This study	UV+Opt	C
67° 5	$26.8^{+1.2}_{-1.2}$	$3.22^{+0.14}_{-0.33}$	$5.96^{+0.09}_{-0.15}$	$-5.95^{+0.23}_{-0.23}$	0.1	1.00	JB25	Opt	F
	$27.5^{+1.00}_{-1.00}$	$2.98^{+0.10}_{-0.15}$	$5.40^{+0.04}_{-0.04}$	$-6.64^{+0.15}_{-0.12}$	0.0200	2.25	SB25	UV+Opt	F
	$25.6^{+1.0}_{-1.0}$	$2.81^{+0.20}_{-0.20}$	$5.89^{+0.12}_{-0.12}$	$-6.05^{+0.14}_{-0.14}$	0.10	1.30	This study	UV+Opt	C
68° 52	$25.2^{+1.2}_{-1.2}$	$2.88^{+0.19}_{-0.14}$	$5.86^{+0.09}_{-0.09}$	$-6.03^{+0.23}_{-0.23}$	0.1	1.00	JB25	Opt	F
	$28.3^{+0.75}_{-0.75}$	$3.10^{+0.25}_{-0.10}$	$5.96^{+0.02}_{-0.02}$	$-6.28^{+0.25}_{-0.25}$	0.0836	1.95	V24	UV+Opt	F
	24.5	2.70	5.76	-5.49	-	2.75	E04	UV+Opt	C
	$26.0^{+1.0}_{-1.0}$	$2.85^{+0.20}_{-0.20}$	$5.87^{+0.12}_{-0.12}$	$-6.28^{+0.25}_{-0.25}$	0.03	2.00	This study	UV+Opt	C
69° 43	$23.7^{+1.2}_{-3.5}$	$2.69^{+0.14}_{-0.33}$	$5.62^{+0.10}_{-0.23}$	$-6.34^{+0.23}_{-0.23}$	0.1	1.00	JB25	Opt	F
	$25.0^{+0.75}_{-2.00}$	$2.85^{+0.05}_{-0.25}$	$5.62^{+0.02}_{-0.09}$	$-6.30^{+0.05}_{-0.25}$	0.2350	2.45	V24	UV+Opt	F
	$22.8^{+0.25}_{-0.22}$	$2.60^{+0.02}_{-0.02}$	5.48	-	-	-	U17	Opt	F
	$22.4^{+1.0}_{-1.0}$	$2.71^{+0.21}_{-0.21}$	$5.55^{+0.11}_{-0.11}$	$-6.49^{+0.25}_{-0.25}$	0.10	2.00	This study	UV+Opt	C
68° 140	$23.7^{+1.2}_{-2.0}$	$3.12^{+0.19}_{-0.29}$	$5.29^{+0.10}_{-0.27}$	$-6.18^{+0.23}_{-0.52}$	0.1	1.00	JB25	Opt	F
	$23.5^{+1.00}_{-1.00}$	$2.75^{+0.10}_{-0.10}$	$5.64^{+0.10}_{-0.10}$	-	-	-	M15	Opt	T
	$24.1^{+1.0}_{-1.0}$	$2.81^{+0.21}_{-0.21}$	$5.52^{+0.11}_{-0.11}$	$-6.46^{+0.25}_{-0.25}$	0.10	2.20	This study	UV+Opt	C
67° 2	$21.3^{+0.8}_{-1.2}$	$2.50^{+0.14}_{-0.14}$	$5.96^{+0.06}_{-0.09}$	$-6.03^{+0.85}_{-0.23}$	0.1	1.00	JB25	Opt	F
	$19.9^{+0.36}_{-0.39}$	$2.30^{+0.03}_{-0.02}$	5.81	-	-	-	U17	Opt	F
	$18.8^{+1.0}_{-1.0}$	$2.31^{+0.21}_{-0.21}$	$5.76^{+0.12}_{-0.12}$	$-6.21^{+0.26}_{-0.26}$	0.14	3.00	This study	UV+Opt	C

U17: (Urbaneja et al. 2017), G18: (Gvaramadze et al. 2018), R18: (Ramachandran et al. 2018), E04: (Evans et al. 2004), M15: (McEvoy et al. 2015), V24: (Verhamme et al. 2024), SB25: (Brands et al. 2025), JB25: (Bestenlehner et al. 2025).

Table F.1: Continued

Target	$T_{\rm eff}$	$\log g$	$\log L$	$\log \dot{M}$	$f_{\rm vol}$	β	Ref.	wavelength	Code
Sk $-$	kK	cm s^{-2}	$L_\odot$	$M_\odot$ yr^{-1}					
67° 14	$22.5^{+0.8}_{-1.2}$	$2.50^{+0.14}_{-0.14}$	$5.60^{+0.08}_{-0.10}$	$-6.24^{+0.23}_{-0.24}$	0.1	1.00	JB25	Opt	F
	$23.3^{+1.50}_{-0.75}$	$2.55^{+0.35}_{-0.50}$	$5.53^{+0.06}_{-0.03}$	$-6.25^{+0.05}_{-0.30}$	0.0028	1.65	V24	UV+Opt	F
	$22.9^{+0.12}_{-0.13}$	$2.70^{+0.01}_{-0.01}$	5.62	-	-	-	U17	Opt	F
	$21.1^{+1.0}_{-1.0}$	$2.51^{+0.21}_{-0.21}$	$5.58^{+0.11}_{-0.11}$	$-6.33^{+0.29}_{-0.29}$	0.10	2.00	This study	UV+Opt	C
69° 52	$20.1^{+3.5}_{-1.2}$	$2.31^{+0.38}_{-0.48}$	$5.58^{+0.26}_{-0.11}$	$-6.89^{+0.34}_{-0.30}$	0.1	1.00	JB25	Opt	F
	$22.5^{+0.25}_{1.75}$	$2.60^{+0.05}_{-0.10}$	$5.73^{+0.00}_{-0.08}$	$-6.70^{+0.10}_{-0.05}$	0.0002	2.60	V24	UV+Opt	F
	$18.8^{+1.0}_{-1.0}$	$2.31^{+0.21}_{-0.21}$	$5.60^{+0.11}_{-0.11}$	$-6.62^{+0.38}_{-0.38}$	0.14	2.50	This study	UV+Opt	C
67° 78	$16.6^{+0.8}_{-1.2}$	$2.31^{+0.14}_{-0.33}$	$5.45^{+0.09}_{-0.13}$	$-6.72^{+0.23}_{-0.51}$	0.1	1.00	JB25	Opt	F
	$17.8^{+1.50}_{-0.25}$	$2.35^{+0.05}_{-0.25}$	$5.62^{+0.06}_{-0.08}$	$-6.82^{+0.05}_{-0.03}$	0.0362	3.45	V24	UV+Opt	F
	$16.2^{+0.98}_{-0.18}$	$2.20^{+0.01}_{-0.02}$	5.36	-	-	-	U17	Opt	F
	$15.5^{+1.0}_{-1.0}$	$2.10^{+0.21}_{-0.21}$	$5.47^{+0.11}_{-0.11}$	$-6.70^{+0.40}_{-0.40}$	0.20	3.00	This study	UV+Opt	C
70° 16	$20.1^{+0.5}_{-1.6}$	$2.69^{+0.14}_{-0.24}$	$4.93^{+0.06}_{-0.14}$	$-8.15^{+1.06}_{-0.73}$	0.1	1.00	JB25	Opt	F
	$20.9^{+2.60}_{+0.70}$	$2.85^{+0.25}_{-0.20}$	$4.92^{+0.14}_{-0.04}$	$-7.70^{+0.3}_{-1.150}$	0.0305	2.90	V24	UV+Opt	F
	$18.4^{+1.0}_{-1.0}$	$2.61^{+0.21}_{-0.21}$	$4.88^{+0.10}_{-0.10}$	$-7.60^{+0.34}_{-0.34}$	0.10	1.00	This study	UV+Opt	C
68° 8	$13.5^{+1.2}_{-0.8}$	$1.50^{+0.29}_{-0.00}$	$5.23^{+0.13}_{-0.10}$	$-6.85^{+0.24}_{-0.37}$	0.1	1.00	JB25	Opt	F
	$14.8^{+2.00}_{-0.75}$	$1.95^{+0.25}_{-0.25}$	$5.56^{+0.00}_{-0.11}$	$-6.90^{+0.60}_{-0.05}$	0.0055	2.00	V24	UV+Opt	F
	$14.1^{+1.0}_{-1.0}$	$1.81^{+0.21}_{-0.21}$	$5.57^{+0.11}_{-0.11}$	$-6.50^{+0.26}_{-0.26}$	0.10	1.00	This study	UV+Opt	C
67° 195	$12.0^{+0.4}_{-0.4}$	$1.88^{+0.19}_{-0.14}$	$4.55^{+0.08}_{-0.08}$	$-7.58^{+0.36}_{-0.29}$	0.1	1.00	JB25	Opt	F
	$14.2^{+0.90}_{-0.50}$	$2.45^{+0.20}_{-0.20}$	$4.72^{+0.06}_{-0.03}$	$-7.45^{+0.60}_{-1.50}$	0.0267	0.65	V24	UV+Opt	F
	$12.6^{+1.0}_{-1.0}$	$2.11^{+0.22}_{-0.22}$	$4.65^{+0.10}_{-0.10}$	$-7.50^{+0.35}_{-0.35}$	0.10	1.00	This study	UV+Opt	C

U17: (Urbaneja et al. 2017), G18: (Gvaramadze et al. 2018), R18: (Ramachandran et al. 2018), E04: (Evans et al. 2004), M15: (McEvoy et al. 2015), V24: (Verhamme et al. 2024), SB25: (Brands et al. 2025), JB25: (Bestenlehner et al. 2025).

Appendix G: Line fitting for individual stars

Fig. G.1-G.16 are the individual diagnostic line fits for each star in our sample. On each row, from top to bottom, are the diagnostic lines used to determine the effective temperature, the effective surface gravity, the wind density paramaters (mass-loss rate, β, clumping paramters), the helium abundance, the nitrogen abundace, the carbon abundance, and the oxygen abundance, respectively.
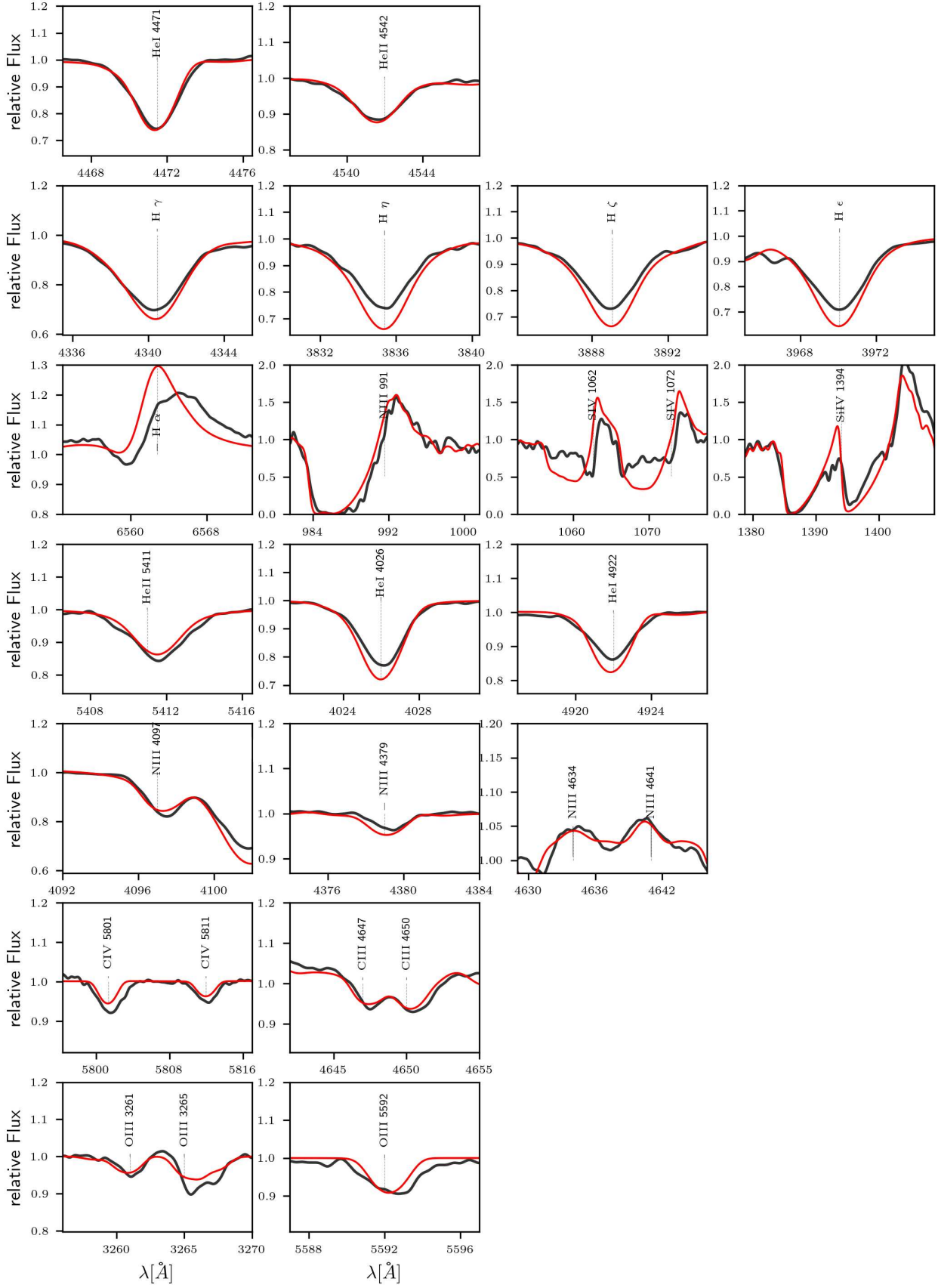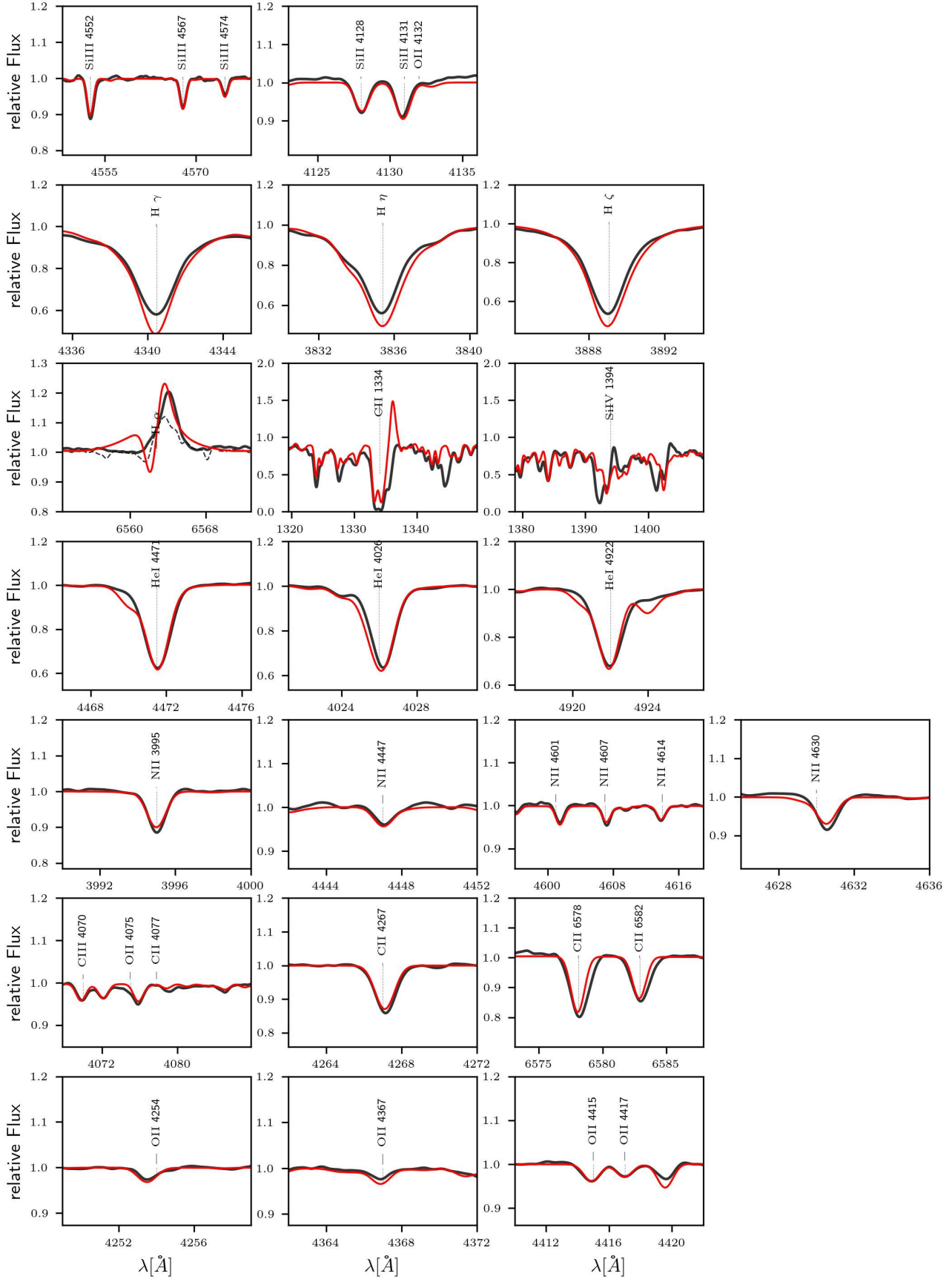
Fig. G.1: Individual line fits for Sk −66° 171. Black solid line: observed spectrum. Red solid line: spectrum of the best fitting model. The observed spectrum is corrected for $v_{\rm rad} = 410 {\rm km\,s^{-1}}$
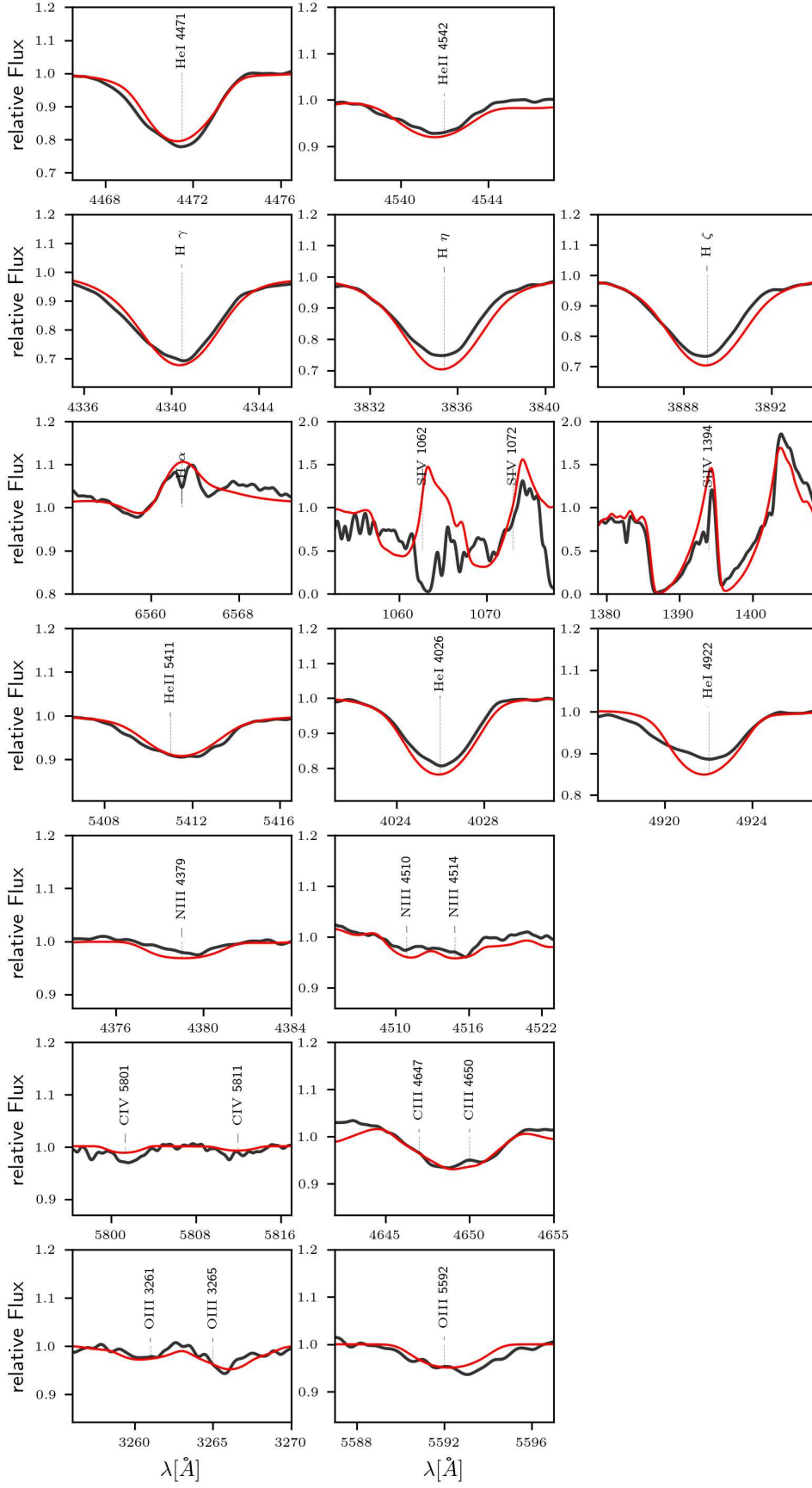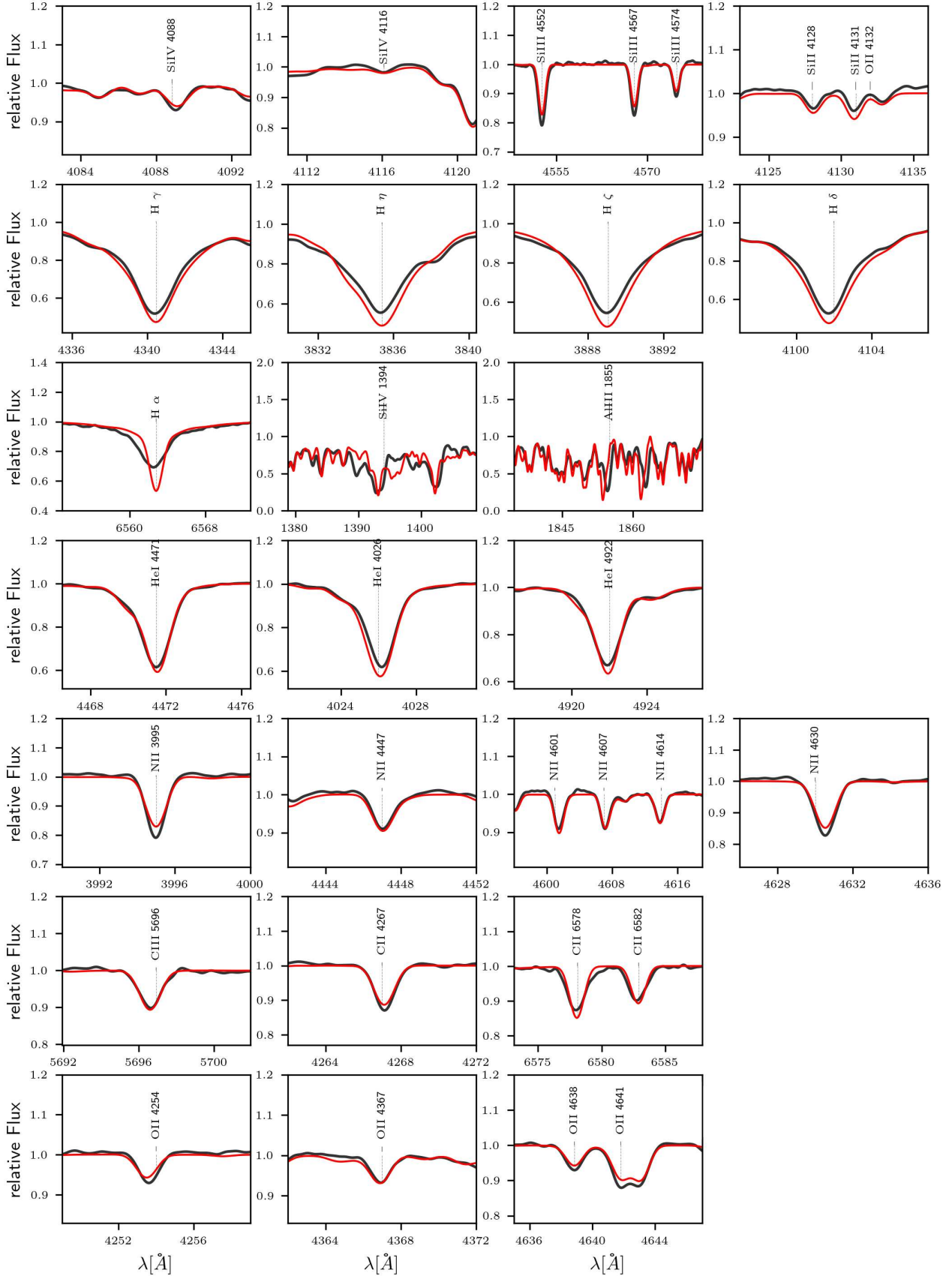
Fig. G.2: Individual line fits for Sk −68° 155. Black solid line: observed spectrum. Red solid line: spectrum of the best fitting model. The observed spectrum is corrected for $v_{\rm rad} = 240 {\rm km\, s^{-1}}$
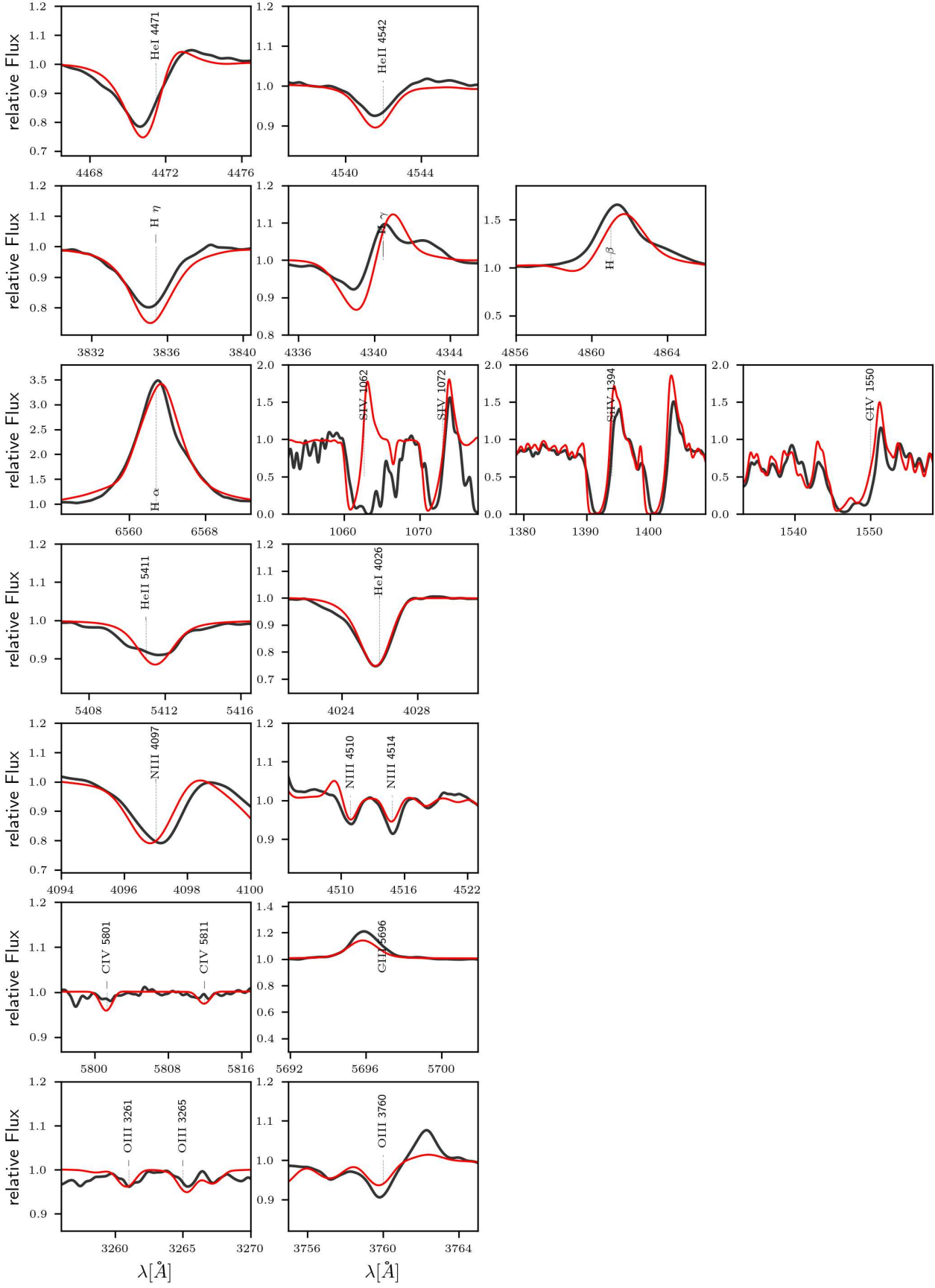
Fig. G.3: Individual line fits for Sk −69° 279. Black solid line: observed spectrum. Red solid line: spectrum of the best fitting model. The observed spectrum is corrected for $v_{\rm rad} = 230{\rm km\,s}^{-1}$
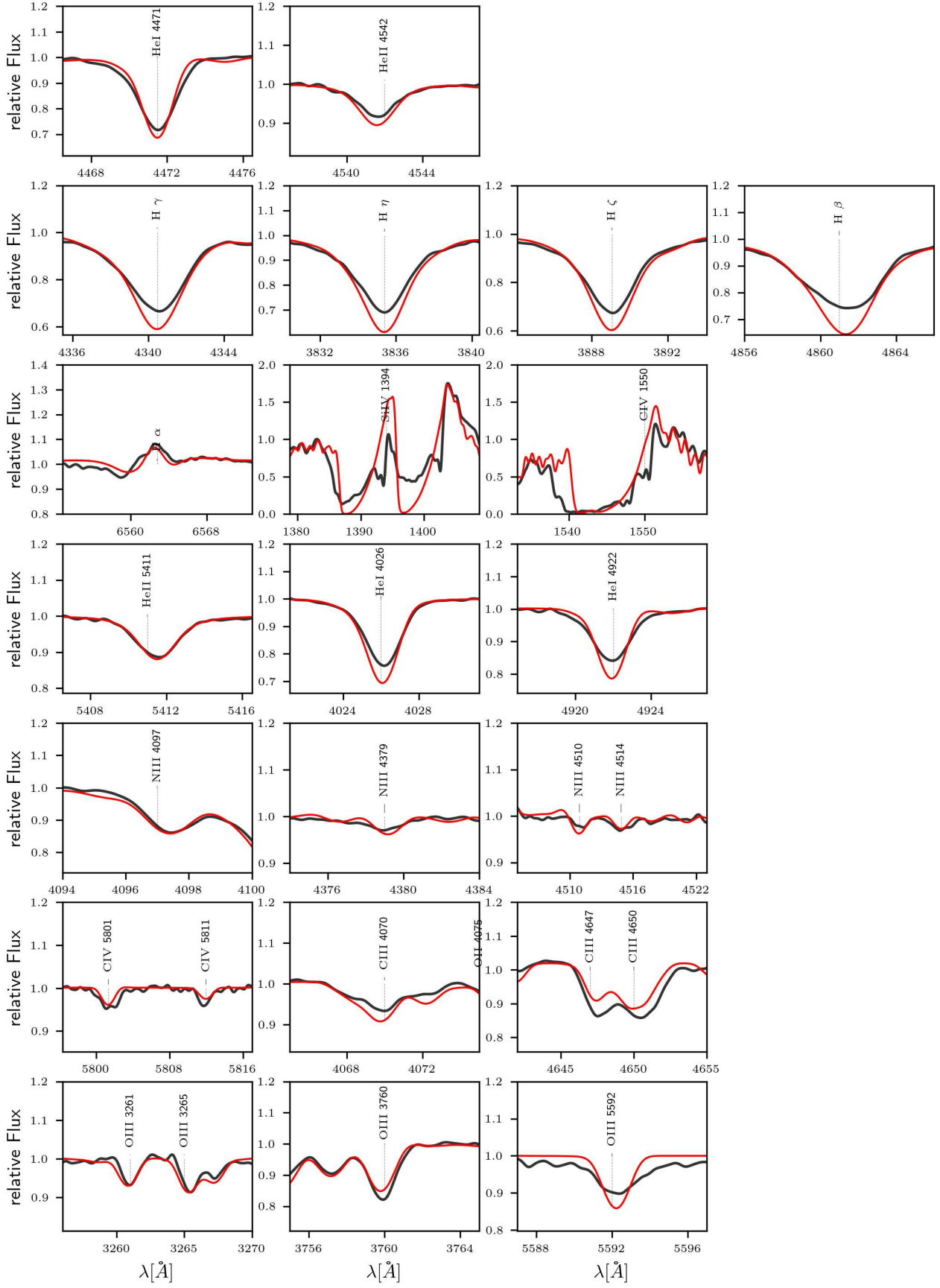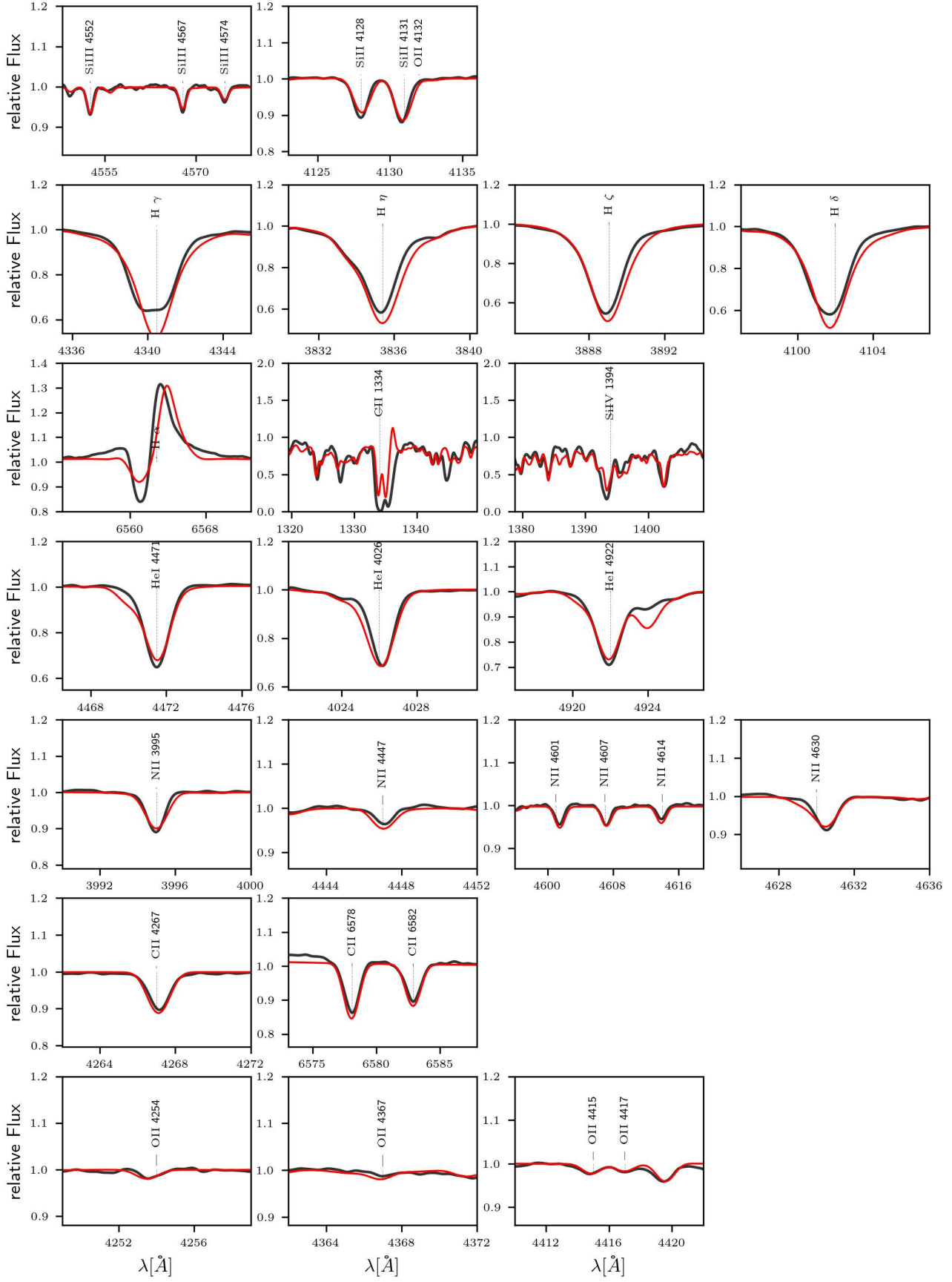
Fig. G.4: Individual line fits for Sk −71° 41. Black solid line: observed spectrum. Red solid line: spectrum of the best fitting model. The observed spectrum is corrected for $v_{\rm rad} = 260\,\mathrm{km\,s^{-1}}$
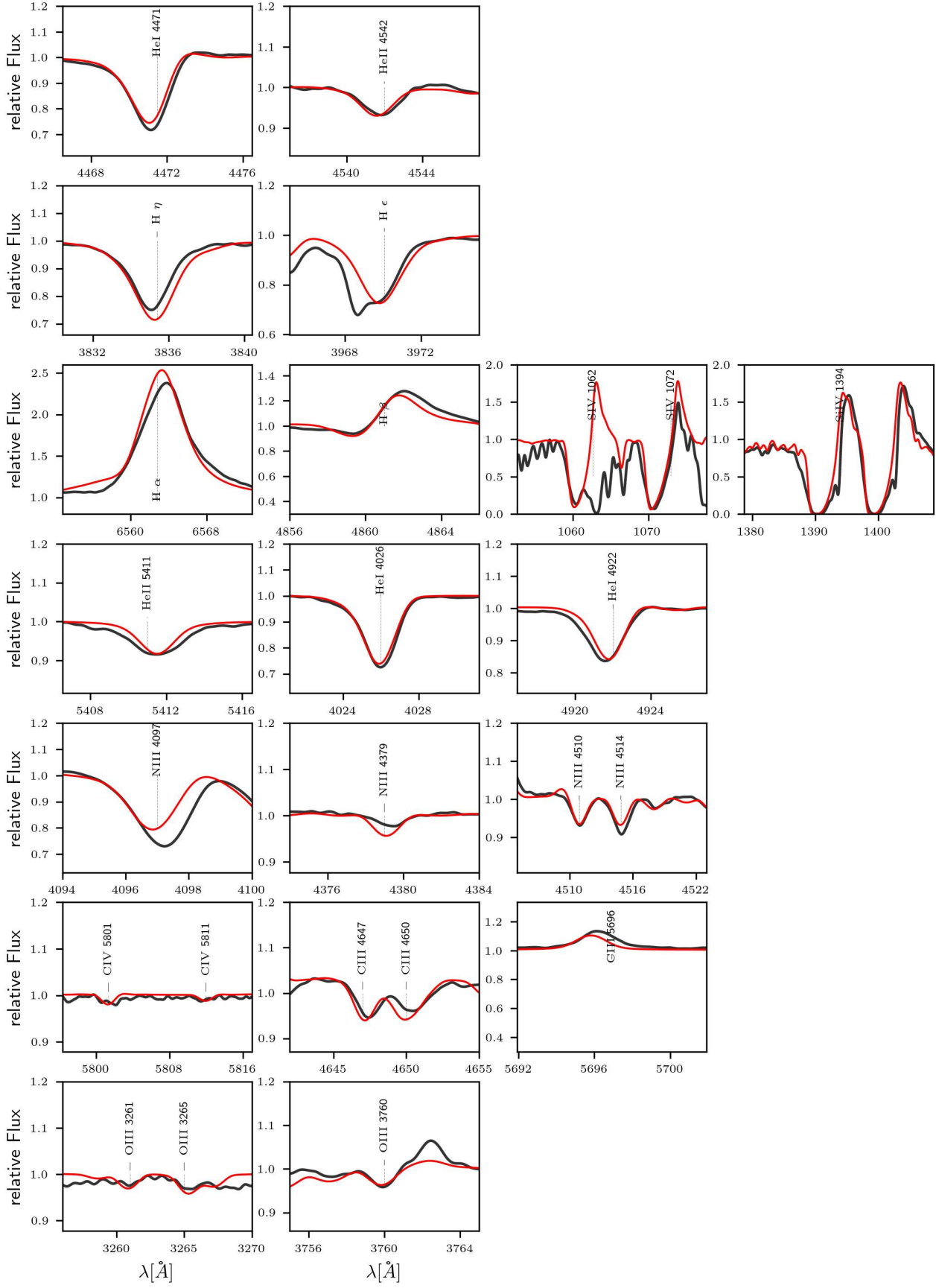
Fig. G.5: Individual line fits for Sk $-68°$ 135. Black solid line: observed spectrum. Red solid line: spectrum of the best fitting model. The observed spectrum is corrected for $v_{\mathrm{rad}} = 270 \mathrm{km\,s}^{-1}$
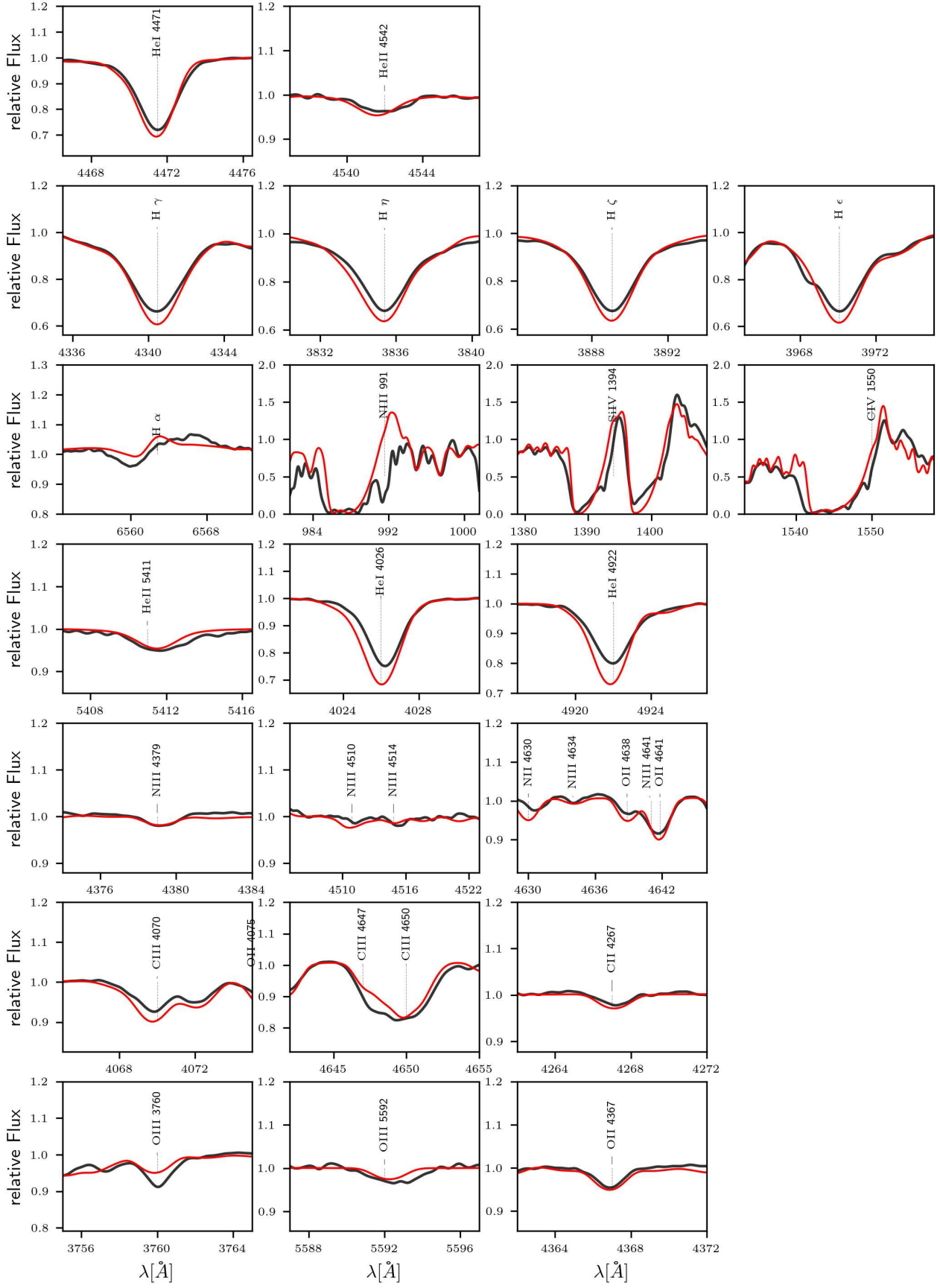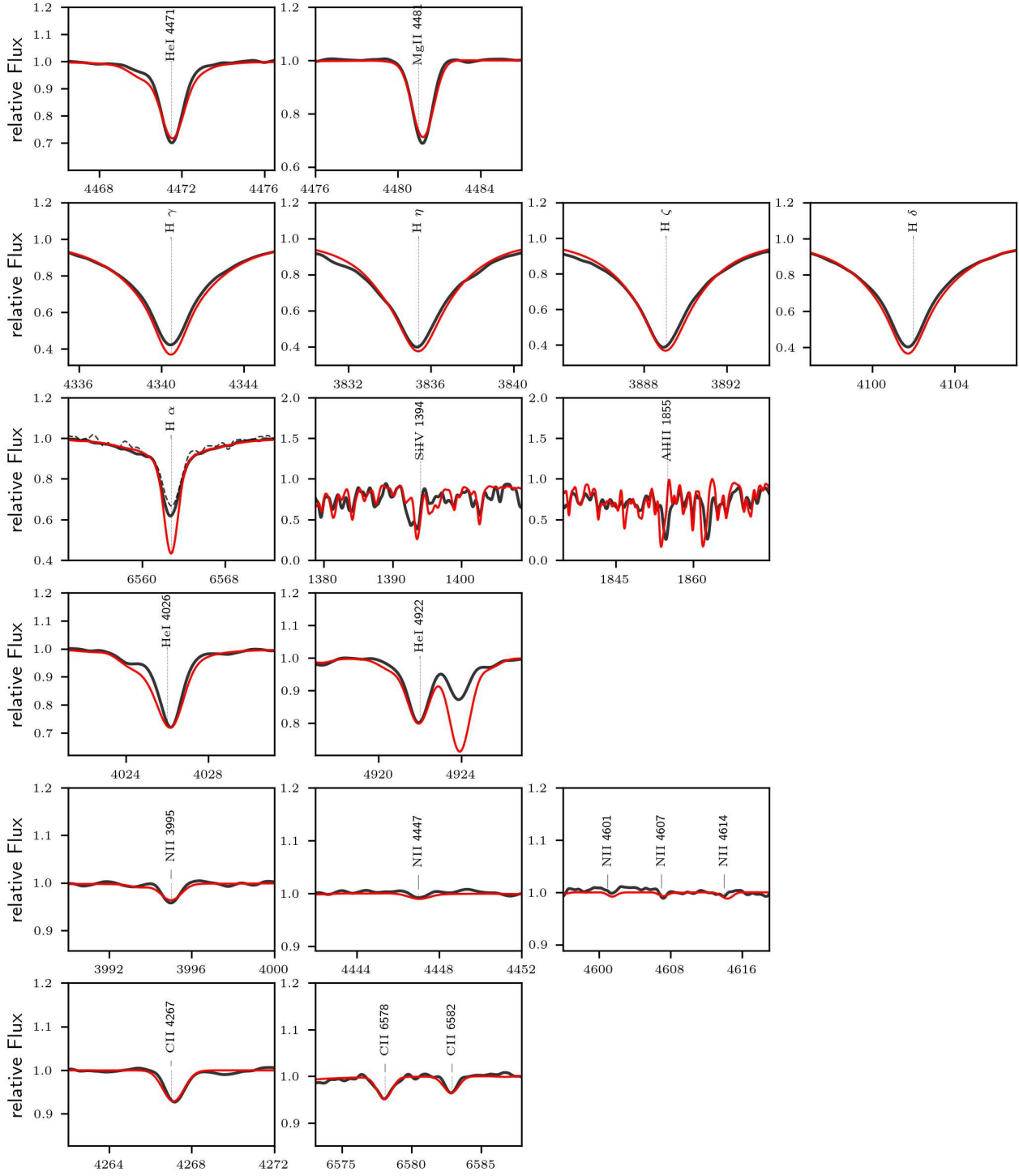
Fig. G.6: Individual line fits for Sk −67° 5. Black solid line: observed spectrum. Red solid line: spectrum of the best fitting model. The observed spectrum is corrected for $v_{\rm rad} = 295 \, {\rm km \, s^{-1}}$
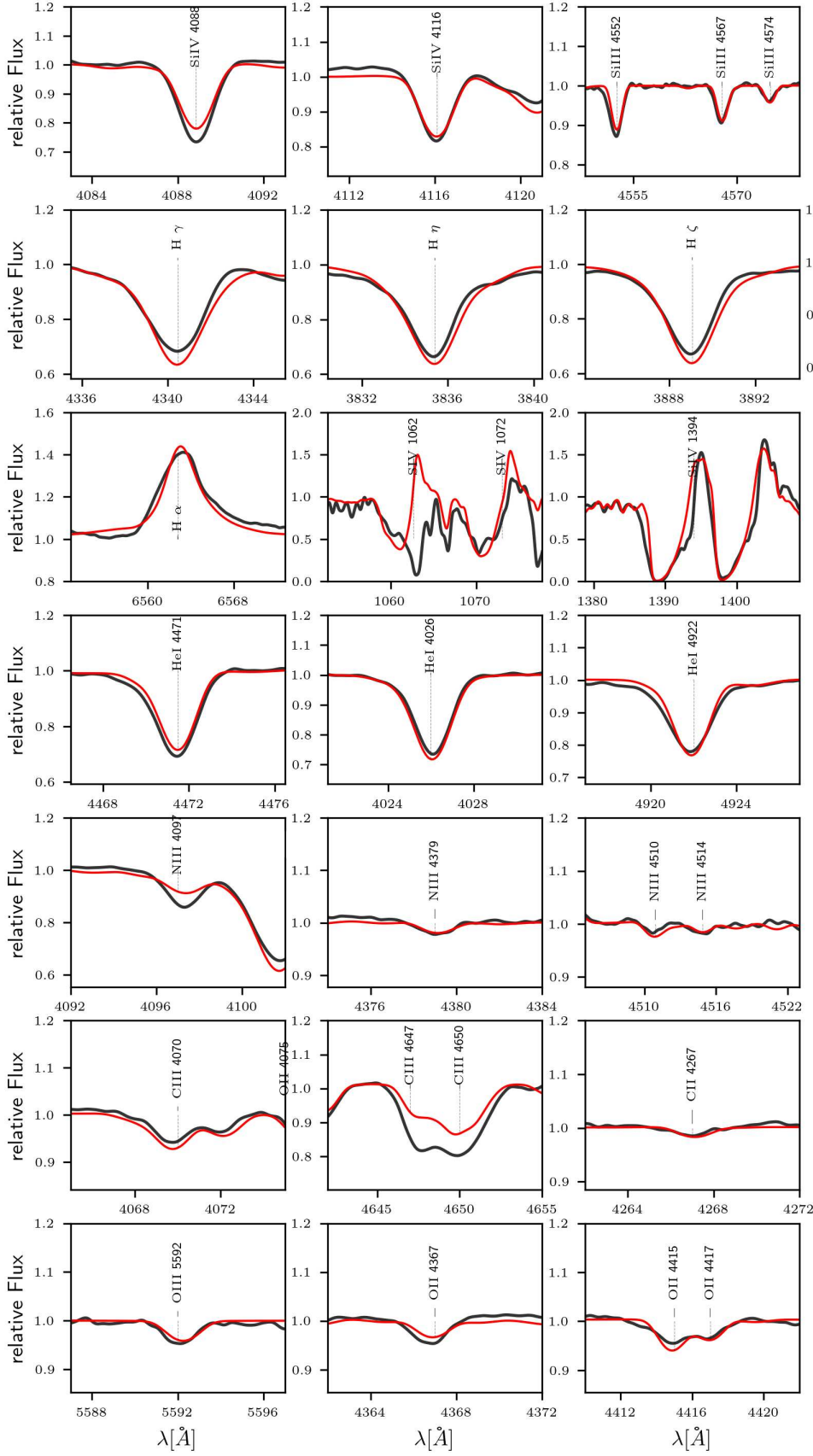
Fig. G.7: Individual line fits for Sk −68° 52. Black solid line: observed spectrum. Red solid line: spectrum of the best fitting model. The observed spectrum is corrected for $v_{\rm rad} = 255{\rm km\,s^{-1}}$
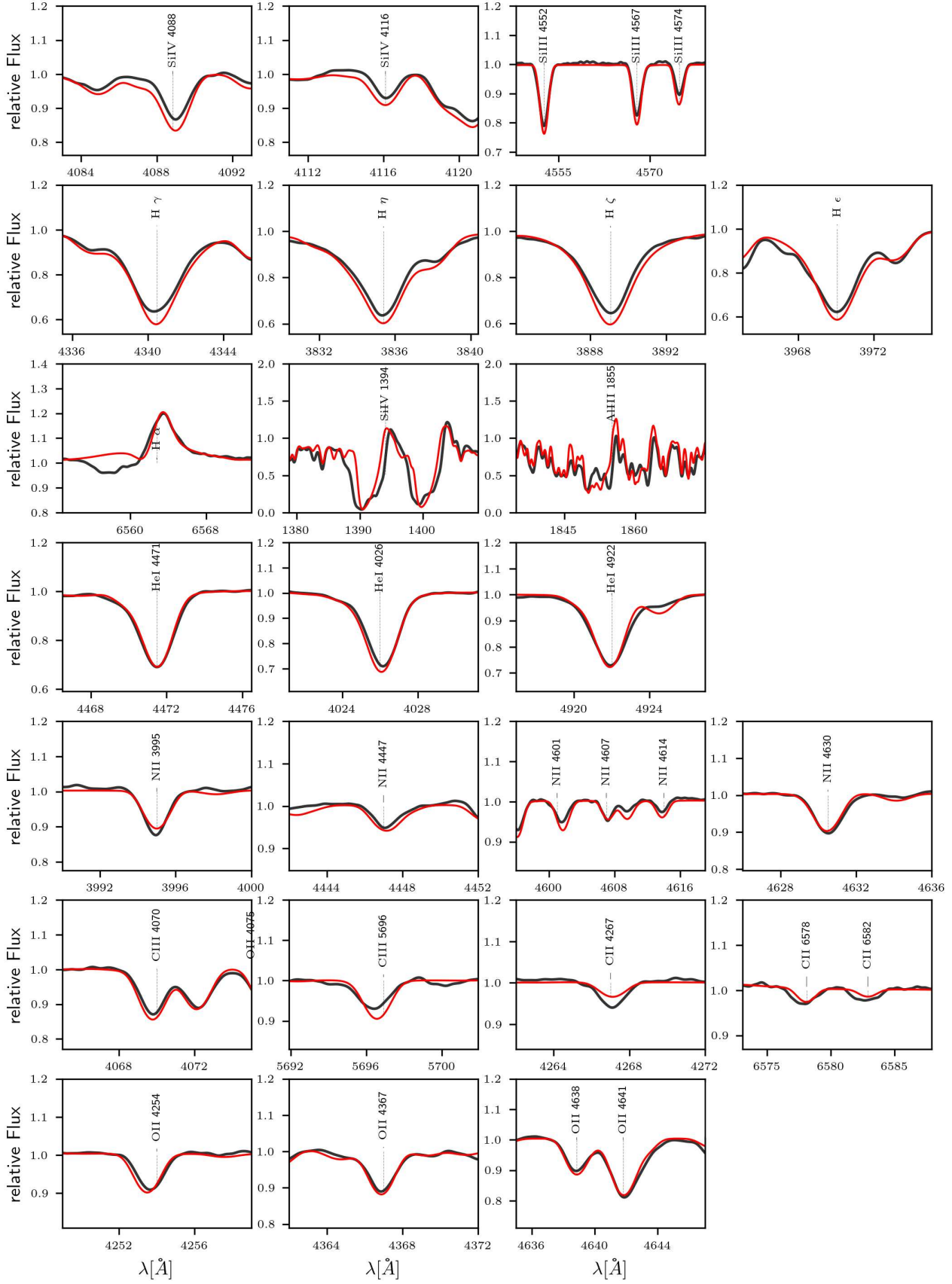
Fig. G.8: Individual line fits for Sk −69° 43. Black solid line: observed spectrum. Red solid line: spectrum of the best fitting model. The observed spectrum is corrected for $v_{\rm rad} = 255\,{\rm km\,s^{-1}}$
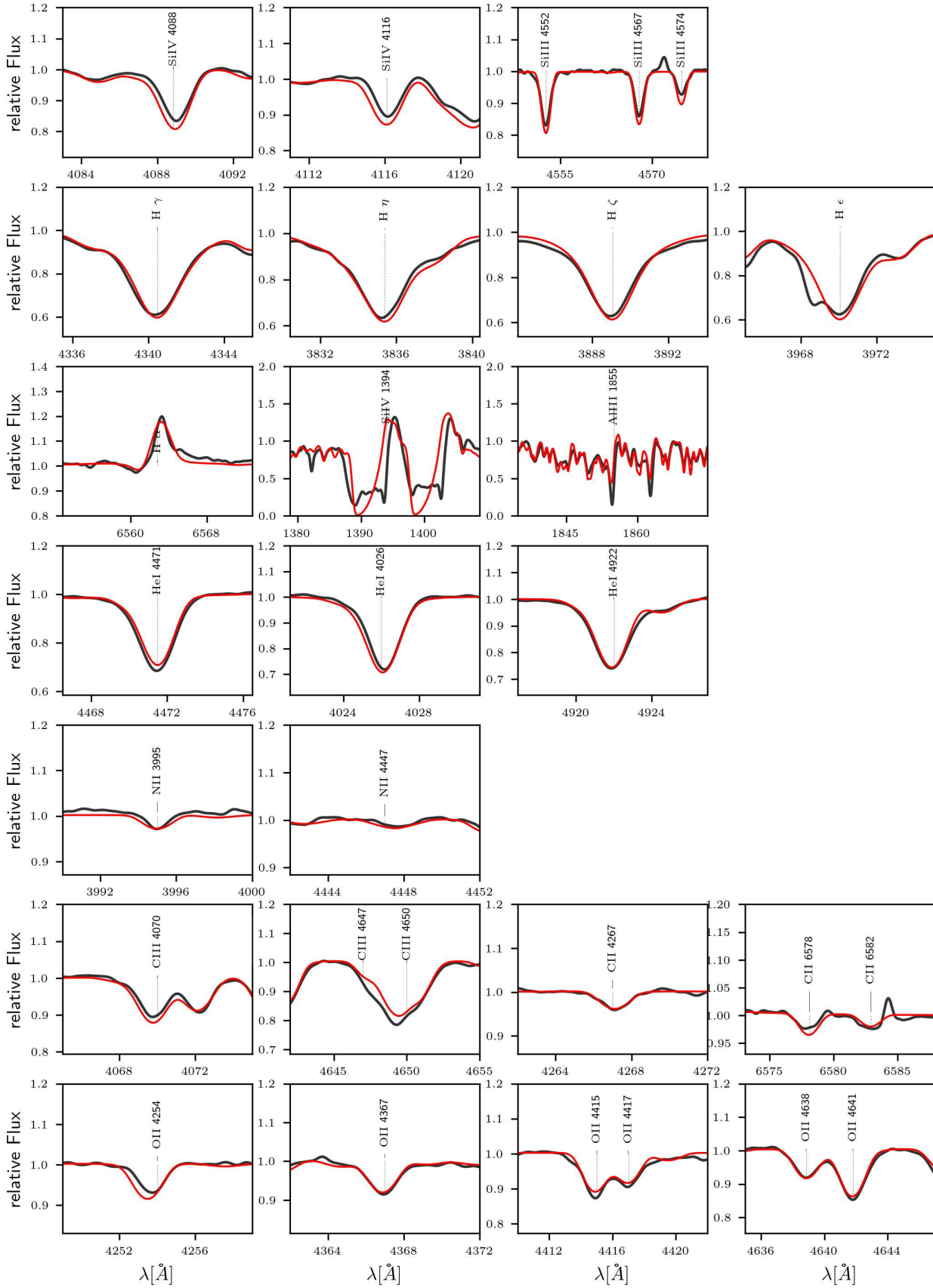
Fig. G.9: Individual line fits for Sk −68° 140. Black solid line: observed spectrum. Red solid line: spectrum of the best fitting model. The observed spectrum is corrected for $v_{\rm rad} = 260{\rm km\,s}^{-1}$
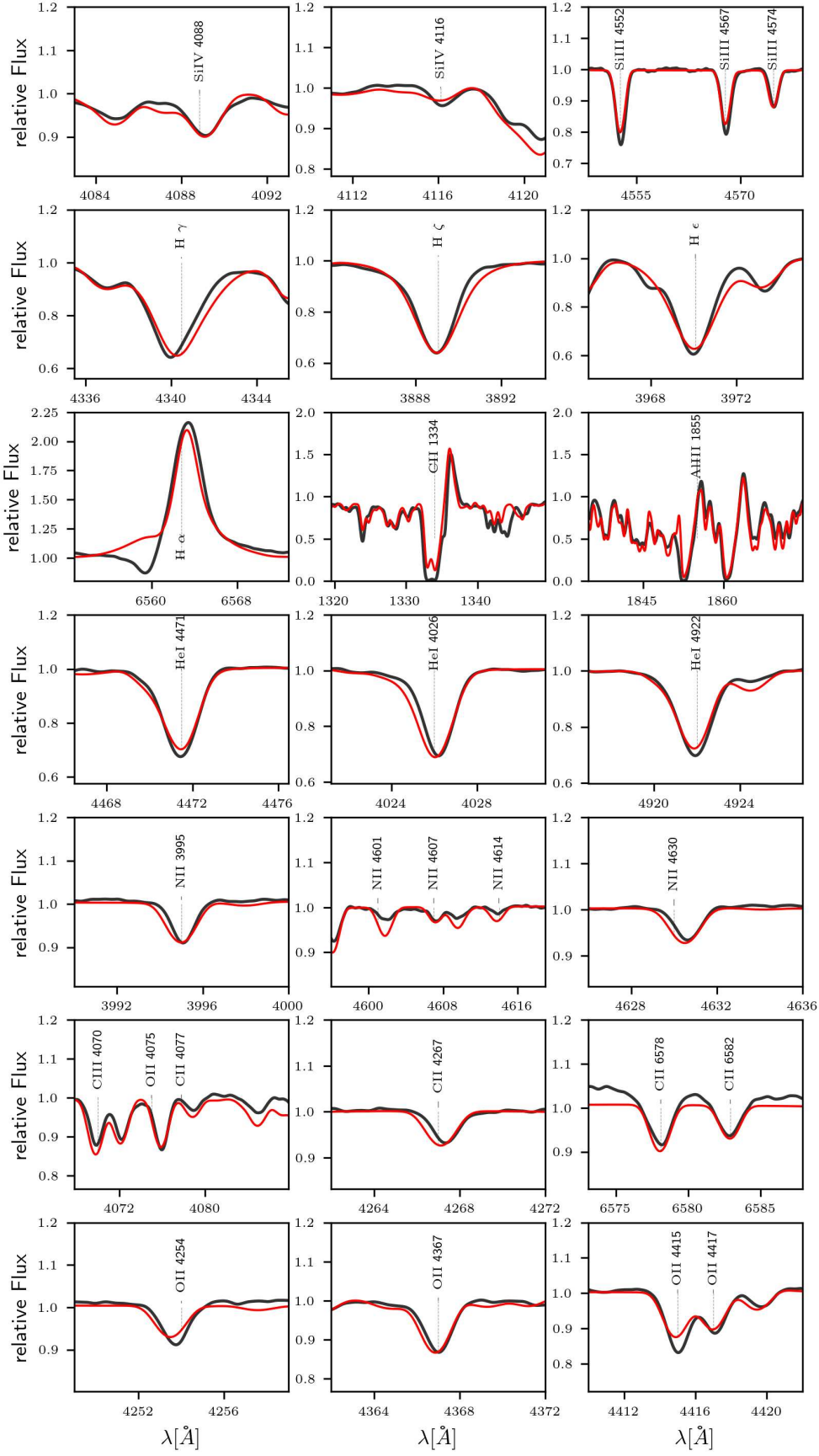
Fig. G.10: Individual line fits for Sk −67° 2. Black solid line: observed spectrum. Red solid line: spectrum of the best fitting model. The observed spectrum is corrected for $v_{rad} = 320 \text{km s}^{-1}$
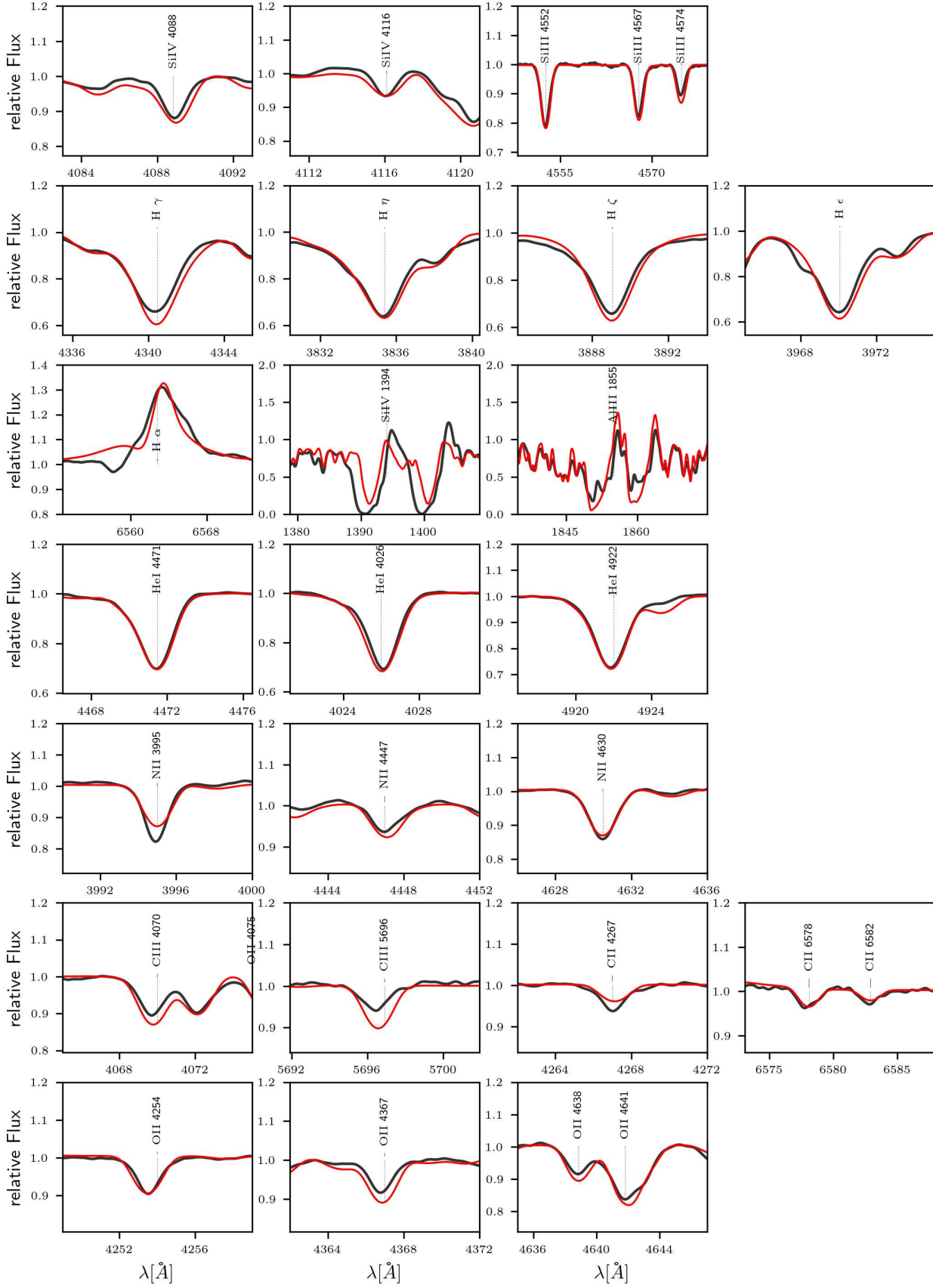
Fig. G.11: Individual line fits for Sk −67° 14. Black solid line: observed spectrum. Red solid line: spectrum of the best fitting model. The observed spectrum is corrected for $v_{rad} = 300 \mathrm{km\,s^{-1}}$
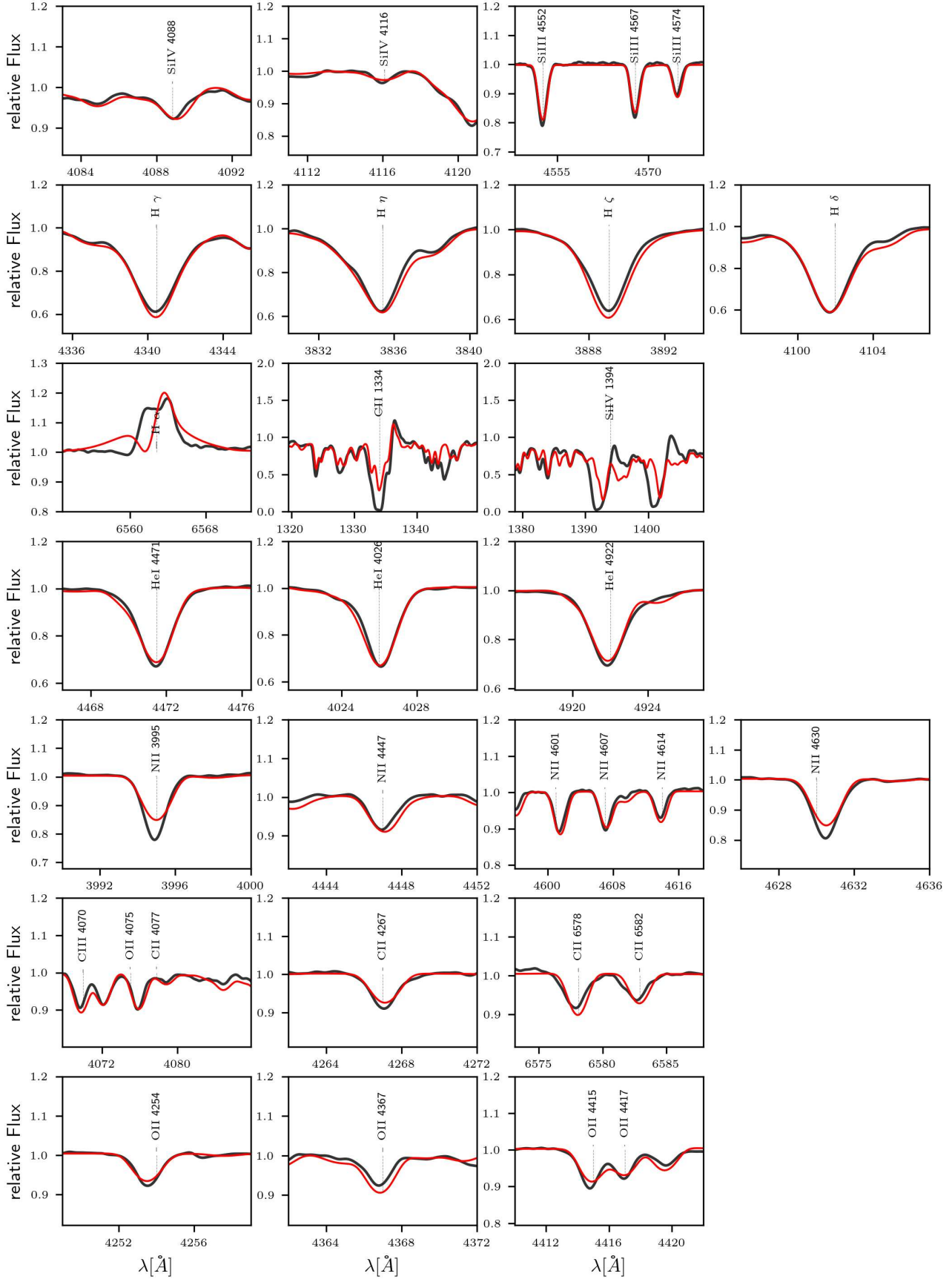
Fig. G.12: Individual line fits for Sk −69° 52. Black solid line: observed spectrum. Red solid line: spectrum of the best fitting model. The observed spectrum is corrected for $v_{\rm rad} = 260 {\rm km\,s^{-1}}$

Fig. G.13: Individual line fits for Sk −67° 78. Black solid line: observed spectrum. Red solid line: spectrum of the best fitting model. The observed spectrum is corrected for $v_{rad} = 310 \mathrm{km\,s^{-1}}$

Fig. G.14: Individual line fits for Sk −70° 16. Black solid line: observed spectrum. Red solid line: spectrum of the best fitting model. The observed spectrum is corrected for $v_{\rm rad} = 265\,{\rm km\,s^{-1}}$

Fig. G.15: Individual line fits for Sk −68° 8. Black solid line: observed spectrum. Red solid line: spectrum of the best fitting model. The observed spectrum is corrected for $v_{\rm rad} = 250\,{\rm km\,s^{-1}}$

Fig. G.16: Individual line fits for Sk −67° 195. Black solid line: observed spectrum. Red solid line: spectrum of the best fitting model. The observed spectrum is corrected for $v_{\mathrm{rad}} = 300\,\mathrm{km\,s^{-1}}$

Appendix H: Overall fitting for individual stars

Fig. H.1-H.16 are the fits for the overall spectrum of each star in
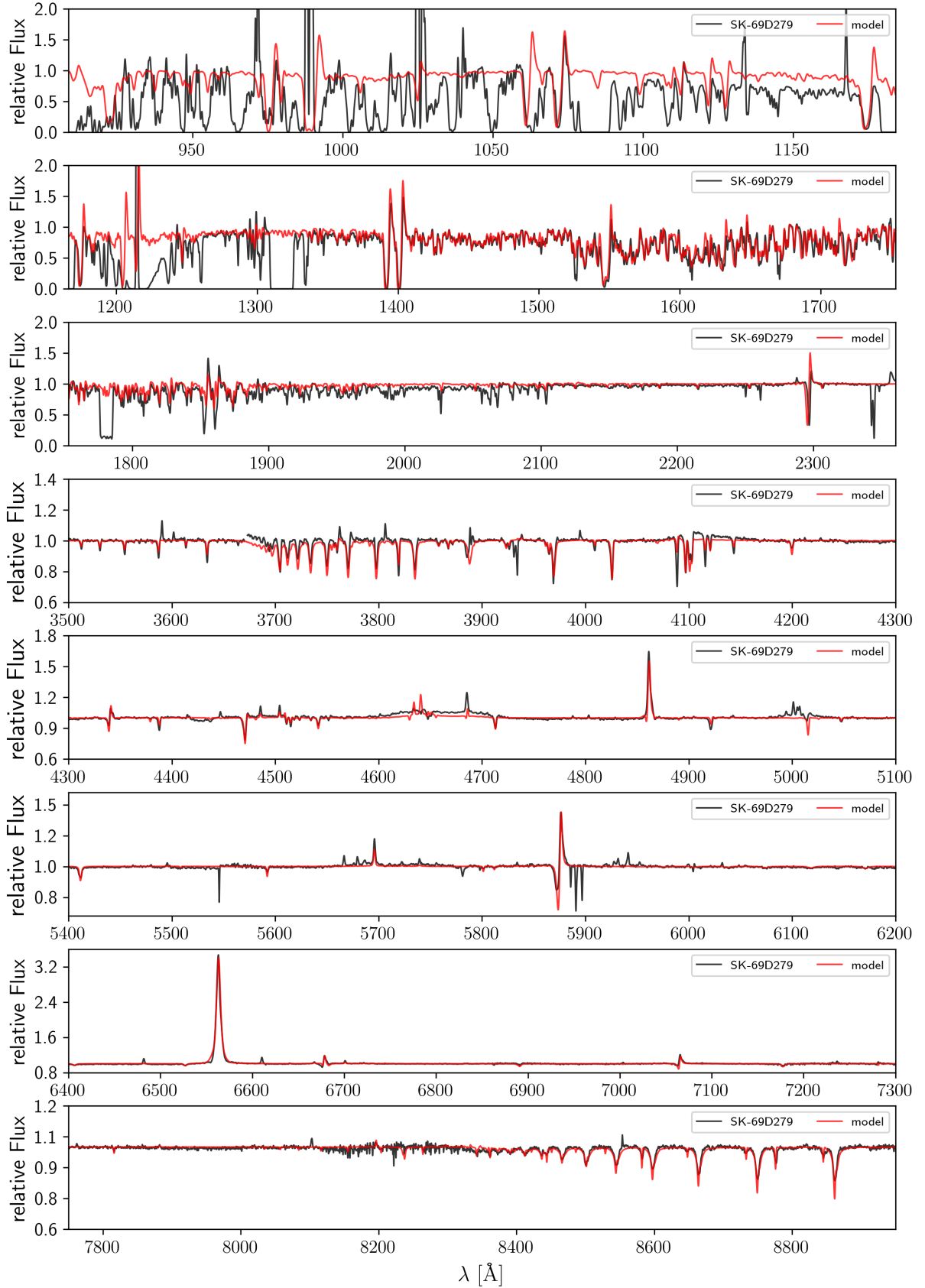our sample.
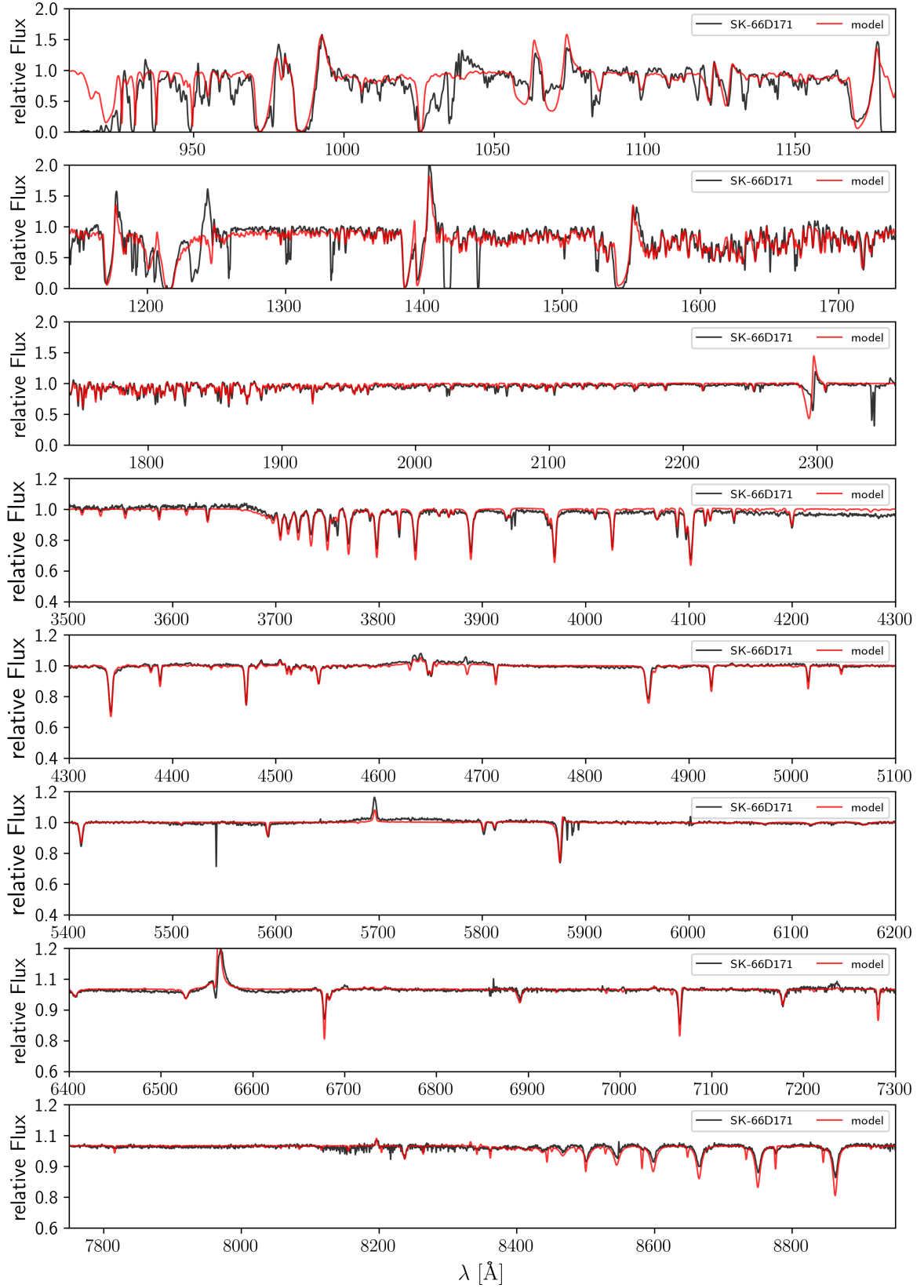
Fig. H.1: An overall view of the best fit (red solid line) to key regions of the observed spectrum (black solid line) of Sk −66° 171. From the top, the first panel is the FUV FUSE range, containing interstellar features such as *Lyδ* λ950, *Lyγ* λ973, and *Lyβ* λ1026. Second and third panels are STIS E140M FUV and STIS E230M NUV spectral ranges, respectively, and we note some interstellar features: *Lyα* λ1216, O ı + P ıı λ1302, C ıı λ1335, Si ıı λ1527, and Al ıı λ1671. The rest of the panels are the UBV and VIS XShooter spectra, with the break between the two arms at ≈ 5600 Å. The lines Ca ıı H + K and Na ı D are interstellar features. For this star, we fit the absorption profiles for *Lyα* through *Lyη*, which were calculated using H ı column density log $N(HI) = 20.7$ cm^{-2} (Fitzpatrick 1985).
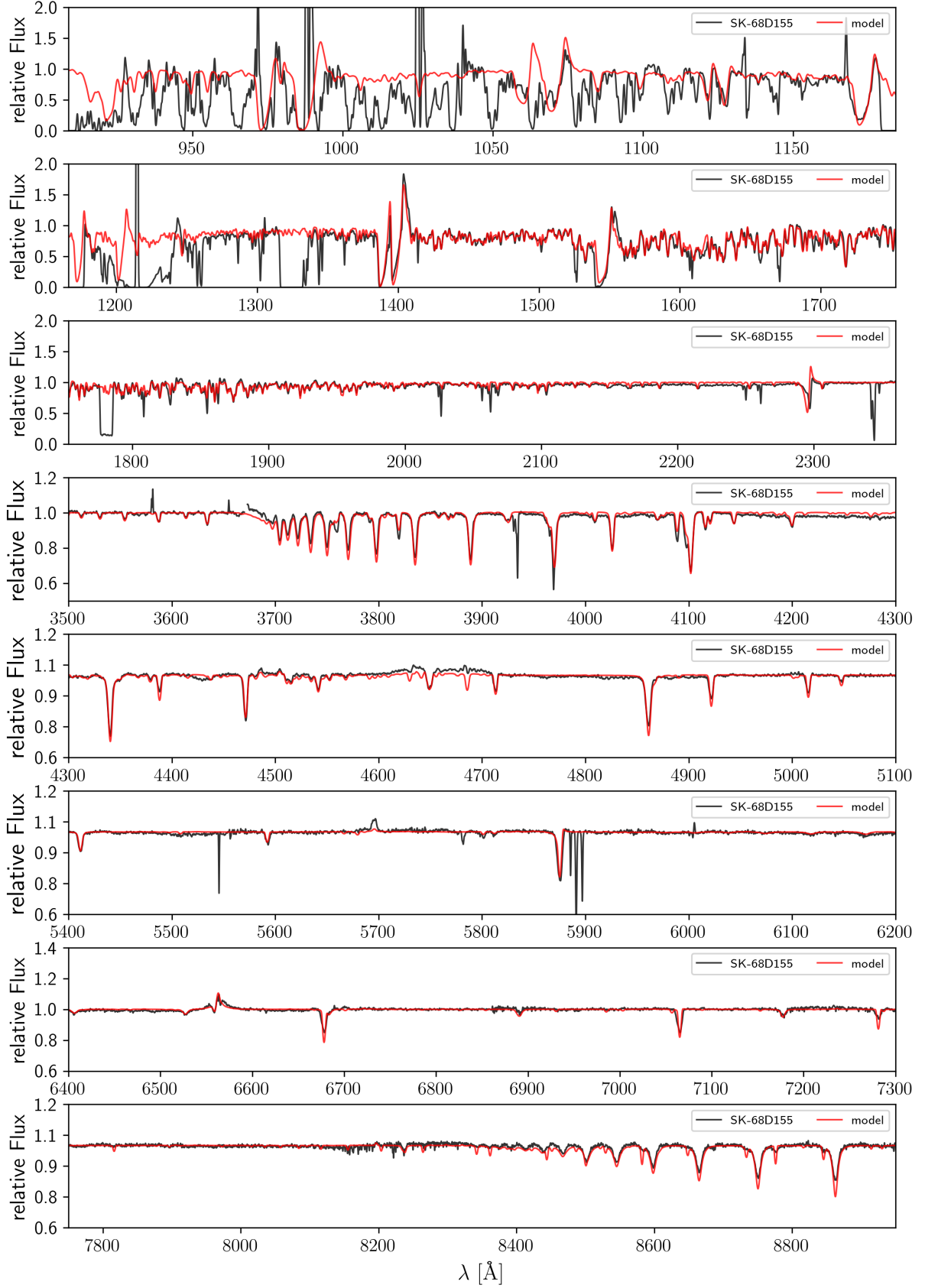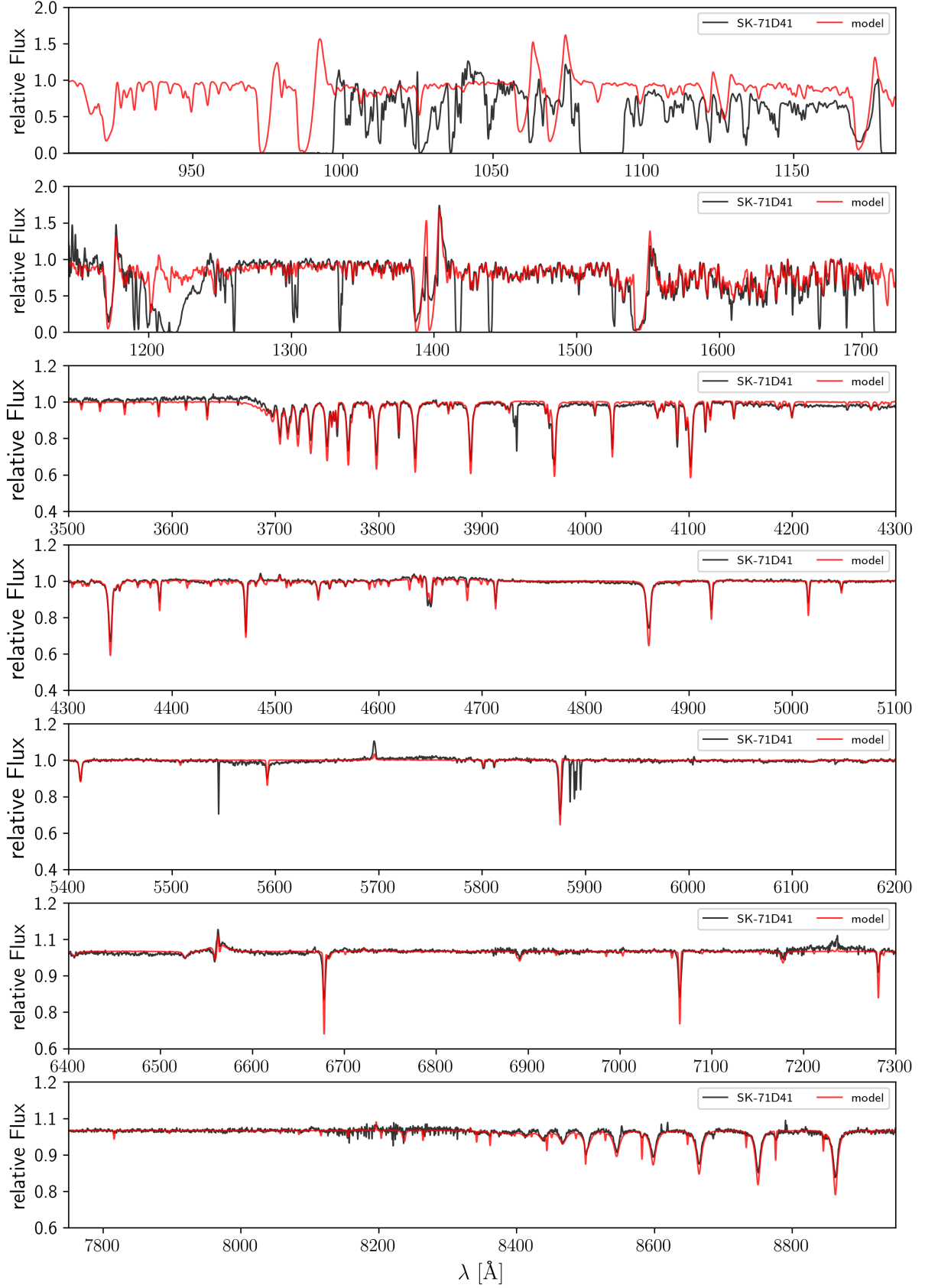
Fig. H.2: An overall view of the best fit (red solid line) to key regions of the observed spectrum (black solid line) of Sk −68° 155. From the top, the first panel is the FUV FUSE range, containing interstellar features such as $Ly\delta$ $\lambda950$, $Ly\gamma$ $\lambda973$, and $Ly\beta$ $\lambda1026$. The second and third panels are the COS G130M+G160M FUV and STIS E230M NUV spectral ranges, respectively, and we note some interstellar features: $Ly\alpha$ $\lambda1216$, O I + P II $\lambda1302$, C II $\lambda1335$, Si II $\lambda1527$, and Al II $\lambda1671$. The rest of the panels are the UBV and VIS XShooter spectra, with the break between the two arms at ≈ 5600 Å. The lines Ca II H + K and Na I D are interstellar features.
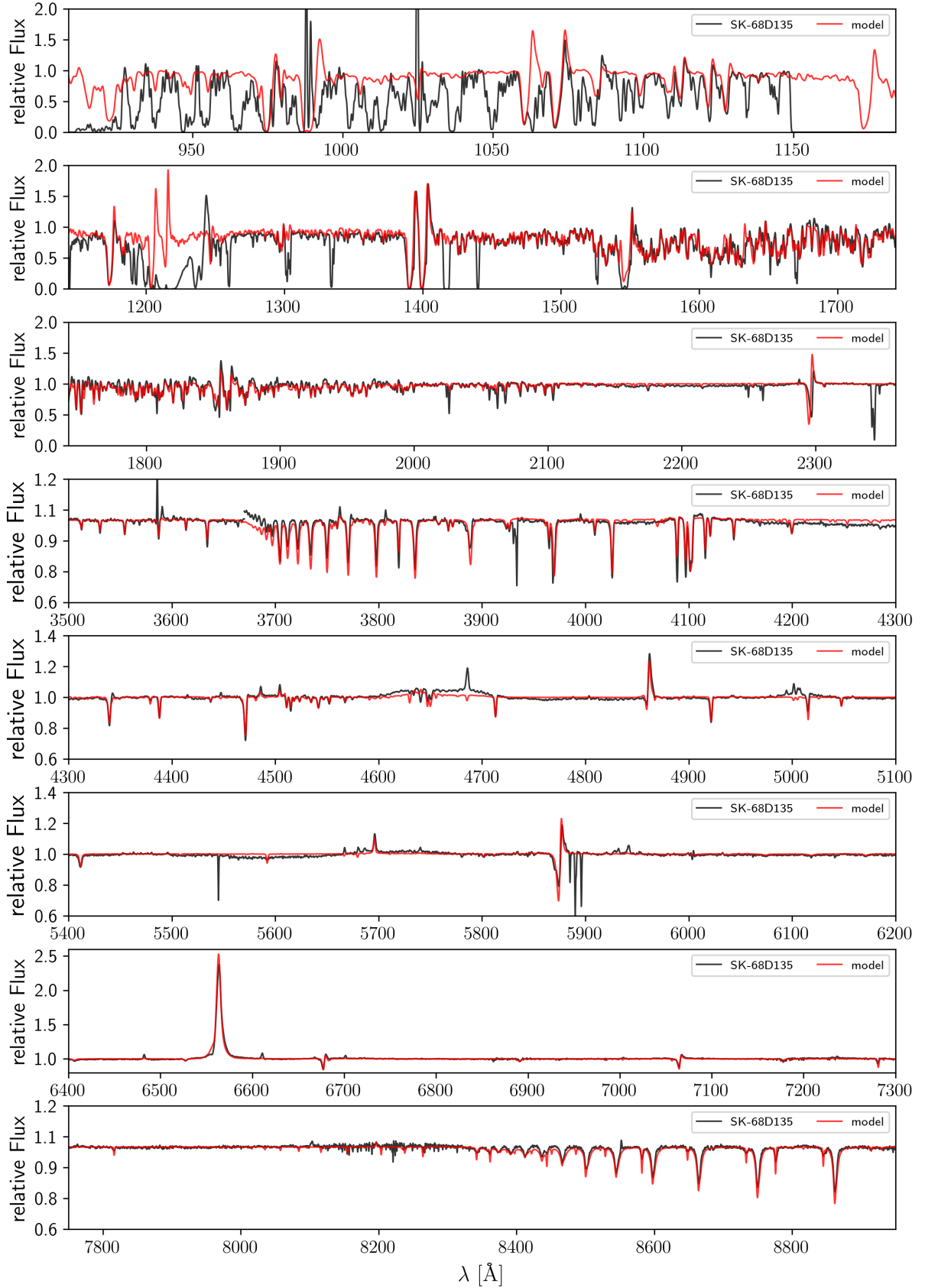
Fig. H.3: An overall view of the best fit (red solid line) to key regions of the observed spectrum (black solid line) of Sk −69° 279. From the top, the first panel is the FUV FUSE range, containing interstellar features such as *Lyδ λ*950, *Lyγ λ*973, and *Lyβ λ*1026. Second and third panels are STIS E140M FUV and STIS E230M NUV spectral ranges, respectively, and we note some interstellar features: *Lyα λ*1216, O I + P II *λ*1302, C II *λ*1335, Si II *λ*1527, and Al II*λ*1671. The rest of the panels are the UBV and VIS XShooter spectra, with the break between the two arms at ≈ 5600 Å. The lines Ca II H + K and Na I D are interstellar features.
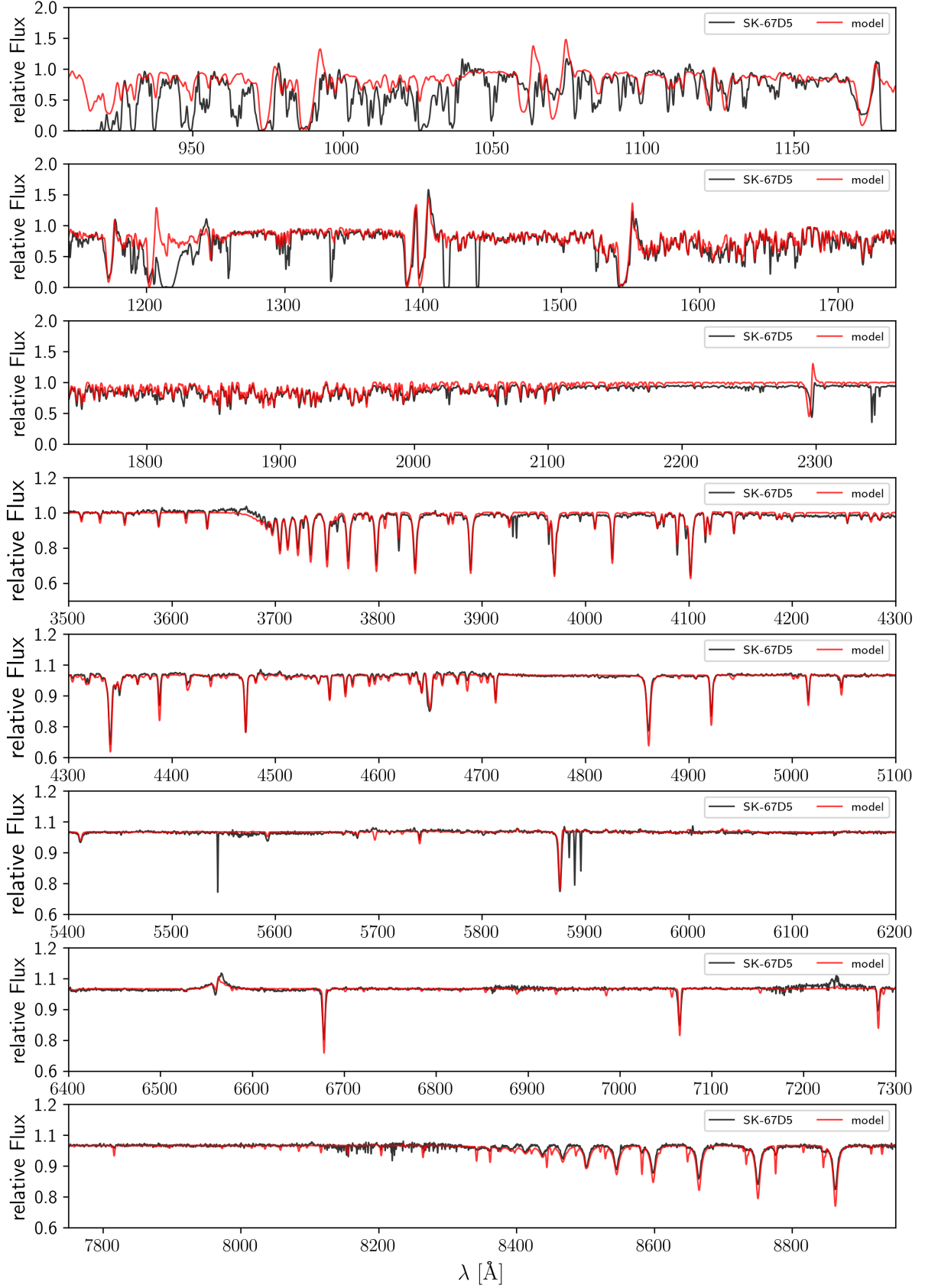
Fig. H.4: An overall view of the best fit (red solid line) to key regions of the observed spectrum (black solid line) of Sk −71° 41. From the top, the first panel is the FUV FUSE range, containing interstellar features such as $Ly\delta$ λ950, $Ly\gamma$ λ973, and $Ly\beta$ λ1026. Second panel is STIS E140M FUV, and we note some interstellar features: $Ly\alpha$ λ1216, O I + P II λ1302, C II λ1335, Si II λ1527, and Al IIλ1671. The rest of the panels are the UBV and VIS XShooter spectra, with the break between the two arms at $\approx$ 5600 Å. The lines Ca II H + K and Na I D are interstellar features.
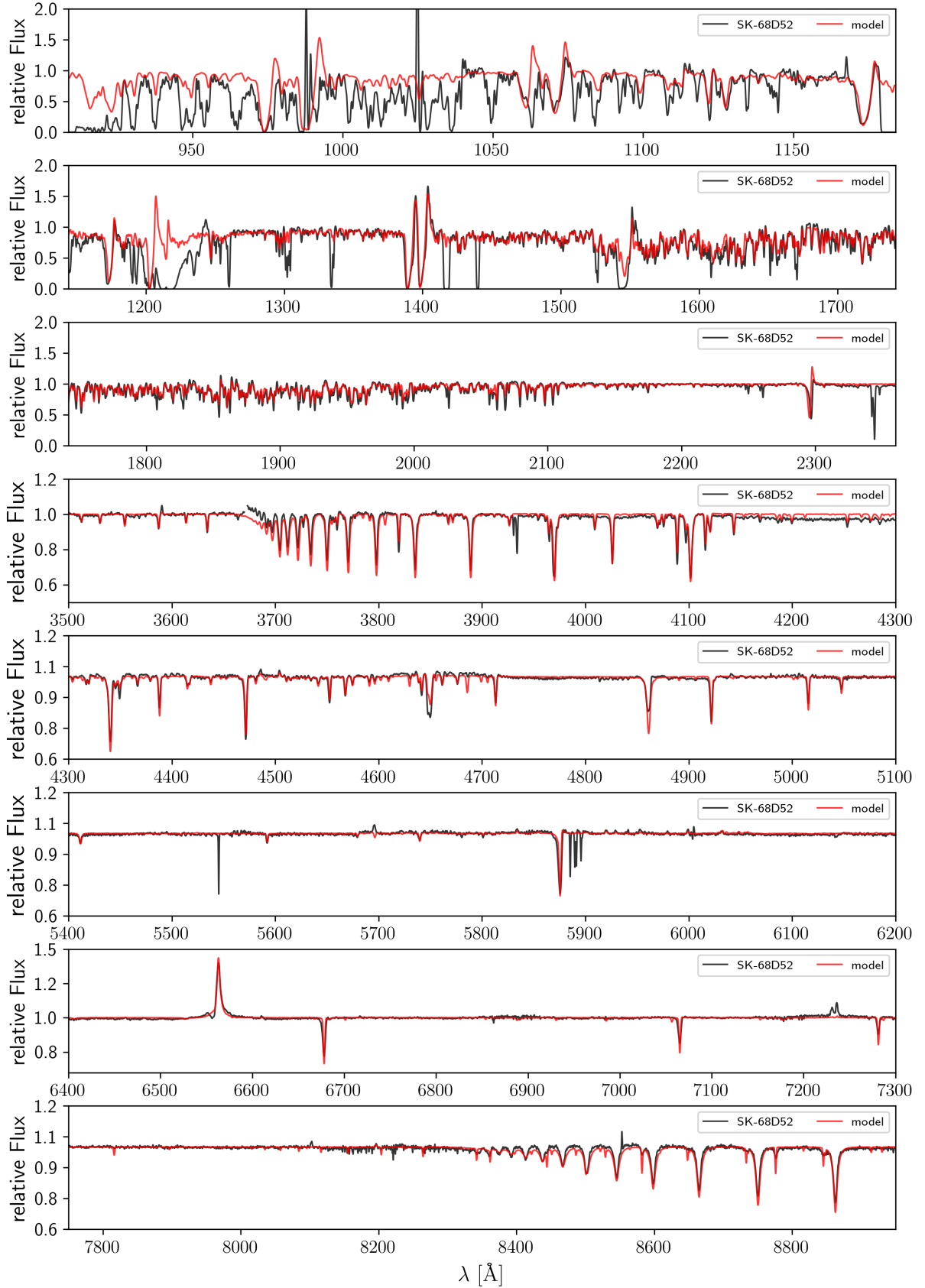
Fig. H.5: An overall view of the best fit (red solid line) to key regions of the observed spectrum (black solid line) of Sk −68° 135. From the top, the first panel is the FUV FUSE range, containing interstellar features such as *Lyδ* λ950, *Lyγ* λ973, and *Lyβ* λ1026. Second and third panels are STIS E140M FUV and STIS E230M NUV spectral ranges, respectively, and we note some interstellar features: *Lyα* λ1216, O I + P II λ1302, C II λ1335, Si II λ1527, and Al IIλ1671. The rest of the panels are the UBV and VIS XShooter spectra, with the break between the two arms at ≈ 5600 Å. The lines Ca II H + K and Na I D are interstellar features.
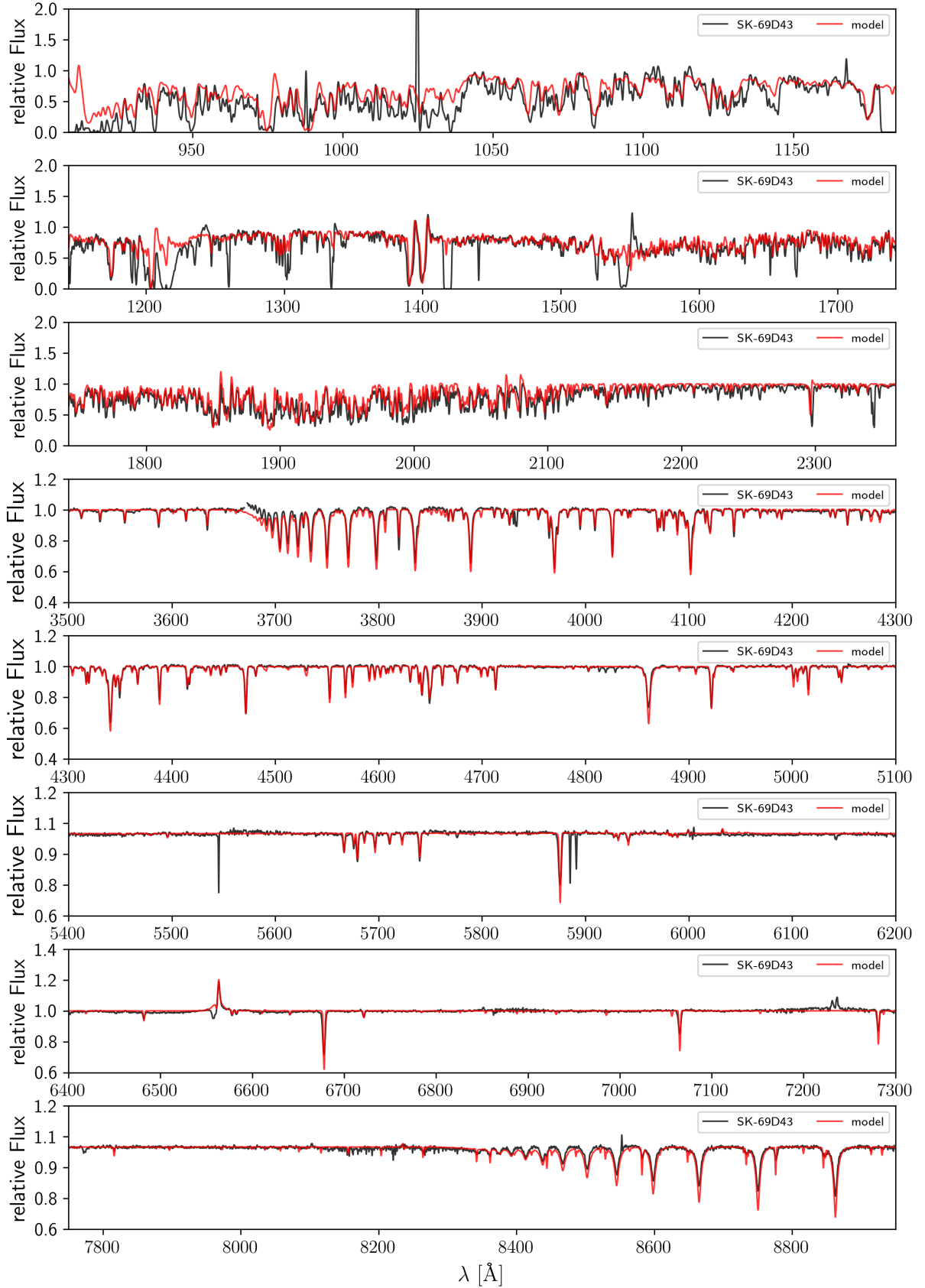
Fig. H.6: An overall view of the best fit (red solid line) to key regions of the observed spectrum (black solid line) of Sk −67° 5. From the top, the first panel is the FUV FUSE range, containing interstellar features such as *Lyδ* λ950, *Lyγ* λ973, and *Lyβ* λ1026. Second and third panels are STIS E140M FUV and STIS E230M NUV spectral ranges, respectively, and we note some interstellar features: *Lyα* λ1216, O I + P II λ1302, C II λ1335, Si II λ1527, and Al II λ1671. The rest of the panels are the UBV and VIS XShooter spectra, with the break between the two arms at ≈ 5600 Å. The lines Ca II H + K and Na I D are interstellar features.

Fig. H.7: An overall view of the best fit (red solid line) to key regions of the observed spectrum (black solid line) of Sk −68° 52. From the top, the first panel is the FUV FUSE range, containing interstellar features such as *Lyδ* λ950, *Lyγ* λ973, and *Lyβ* λ1026. Second and third panels are STIS E140M FUV and STIS E230M NUV spectral ranges, respectively, and we note some interstellar features: *Lyα* λ1216, O I + P II λ1302, C II λ1335, Si II λ1527, and Al IIλ1671. The rest of the panels are the UBV and VIS XShooter spectra, with the break between the two arms at ≈ 5600 Å. The lines Ca II H + K and Na I D are interstellar features.
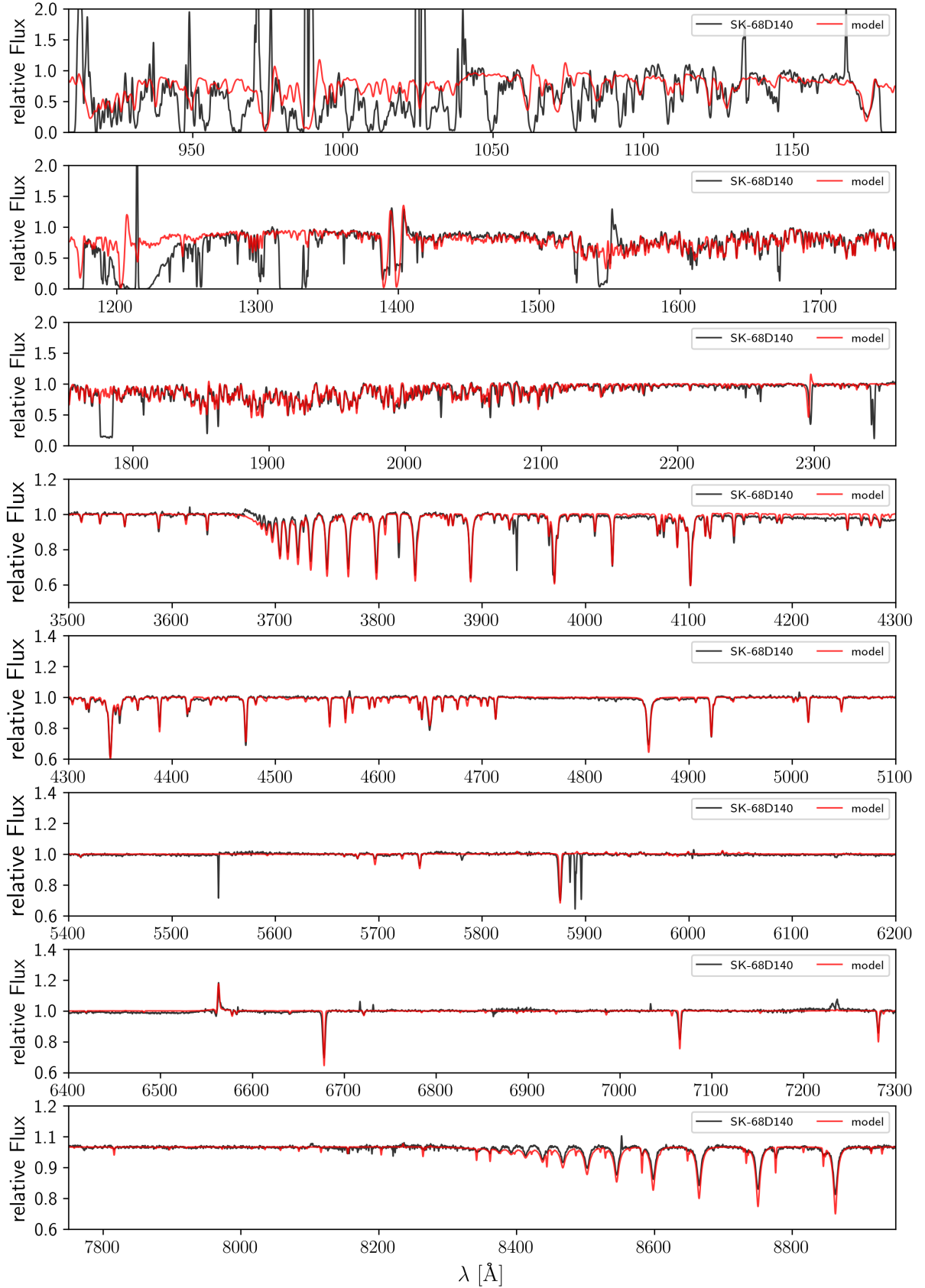
Fig. H.8: An overall view of the best fit (red solid line) to key regions of the observed spectrum (black solid line) of Sk −69° 43. From the top, the first panel is the FUV FUSE range, containing interstellar features such as *Lyδ* λ950, *Lyγ* λ973, and *Lyβ* λ1026. Second and third panels are STIS E140M FUV and STIS E230M NUV spectral ranges, respectively, and we note some interstellar features: *Lyα* λ1216, O I + P II λ1302, C II λ1335, Si II λ1527, and Al II λ1671. The rest of the panels are the UBV and VIS XShooter spectra, with the break between the two arms at ≈ 5600 Å. The lines Ca II H + K and Na I D are interstellar features.
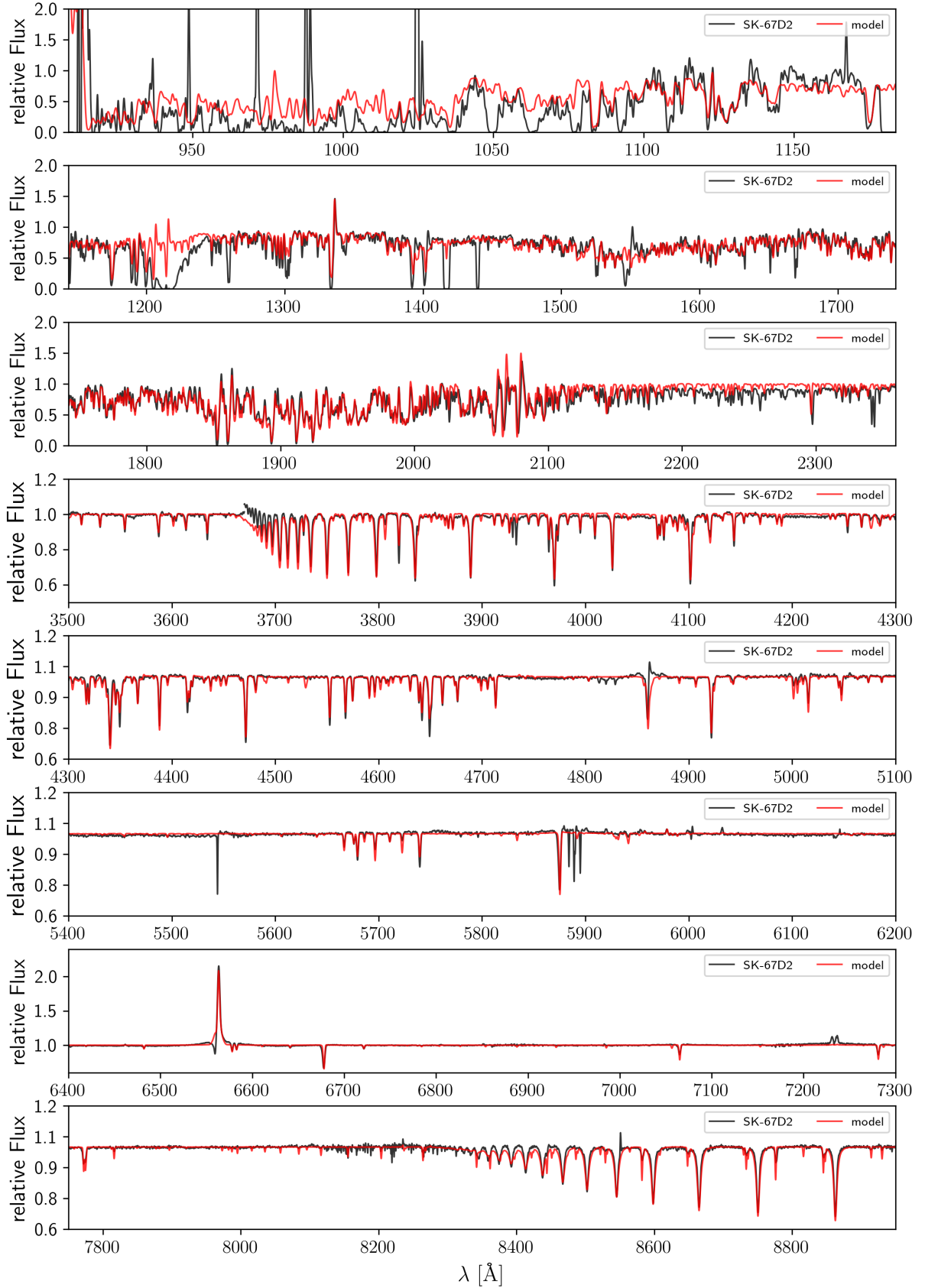
Fig. H.9: An overall view of the best fit (red solid line) to key regions of the observed spectrum (black solid line) of Sk −68° 140. From the top, the first panel is the FUV FUSE range, containing interstellar features such as *Lyδ* λ950, *Lyγ* λ973, and *Lyβ* λ1026. Second and third panels are COS G130M+G160M FUV and STIS E230M NUV spectral ranges, respectively, and we note some interstellar features: *Lyα* λ1216, O I + P II λ1302, C II λ1335, Si II λ1527, and Al II λ1671. The rest of the panels are the UBV and VIS XShooter spectra, with the break between the two arms at ≈ 5600 Å. The lines Ca II H + K and Na I D are interstellar features.
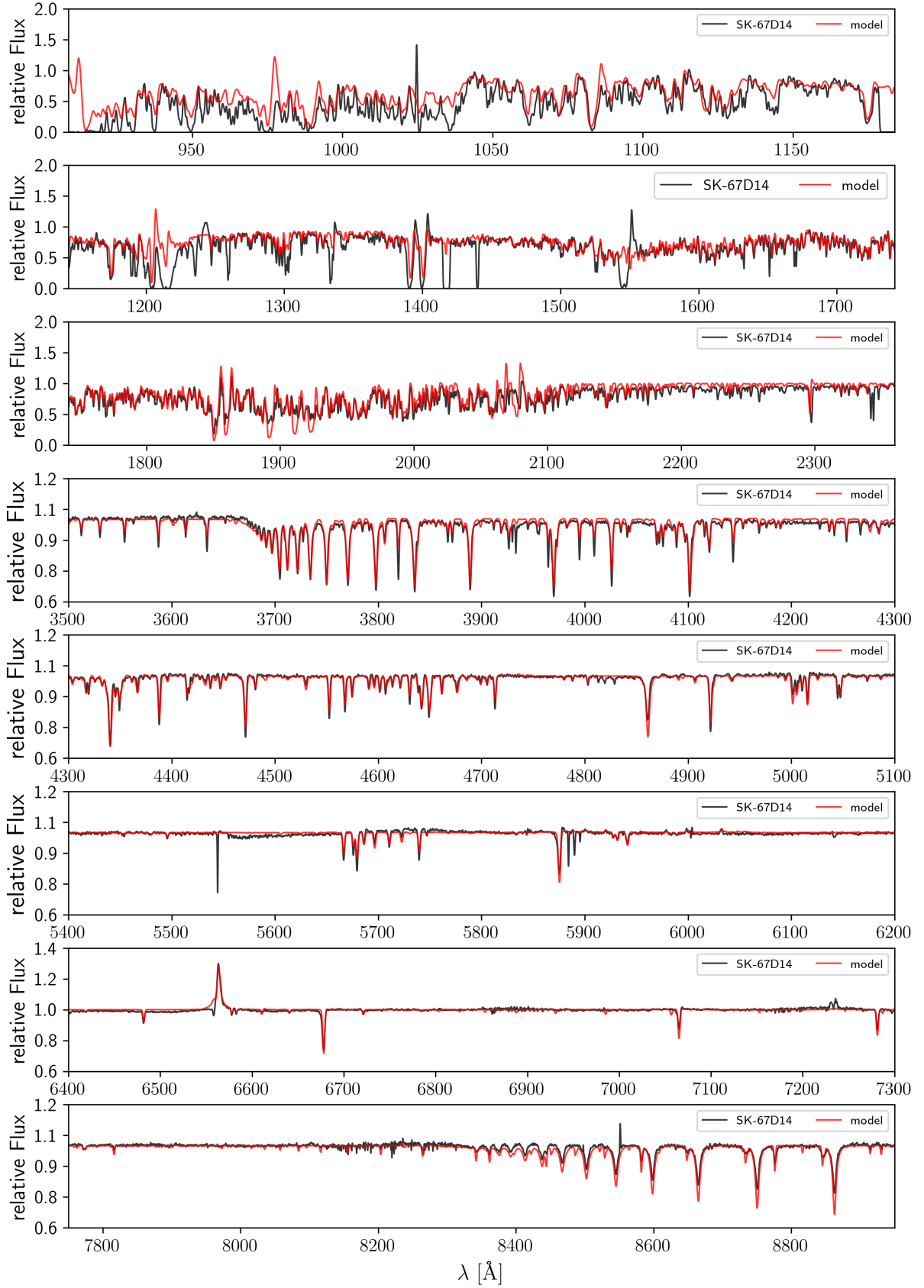
Fig. H.10: An overall view of the best fit (red solid line) to key regions of the observed spectrum (black solid line) of Sk −67° 2. From the top, the first panel is the FUV FUSE range, containing interstellar features such as *Lyδ* λ950, *Lyγ* λ973, and *Lyβ* λ1026. Second and third panels are STIS E140M FUV and STIS E230M NUV spectral ranges, respectively, and we note some interstellar features: *Lyα* λ1216, O I + P II λ1302, C II λ1335, Si II λ1527, and Al II λ1671. The rest of the panels are the UBV and VIS XShooter spectra, with the break between the two arms at ≈ 5600 Å. The lines Ca II H + K and Na I D are interstellar features.
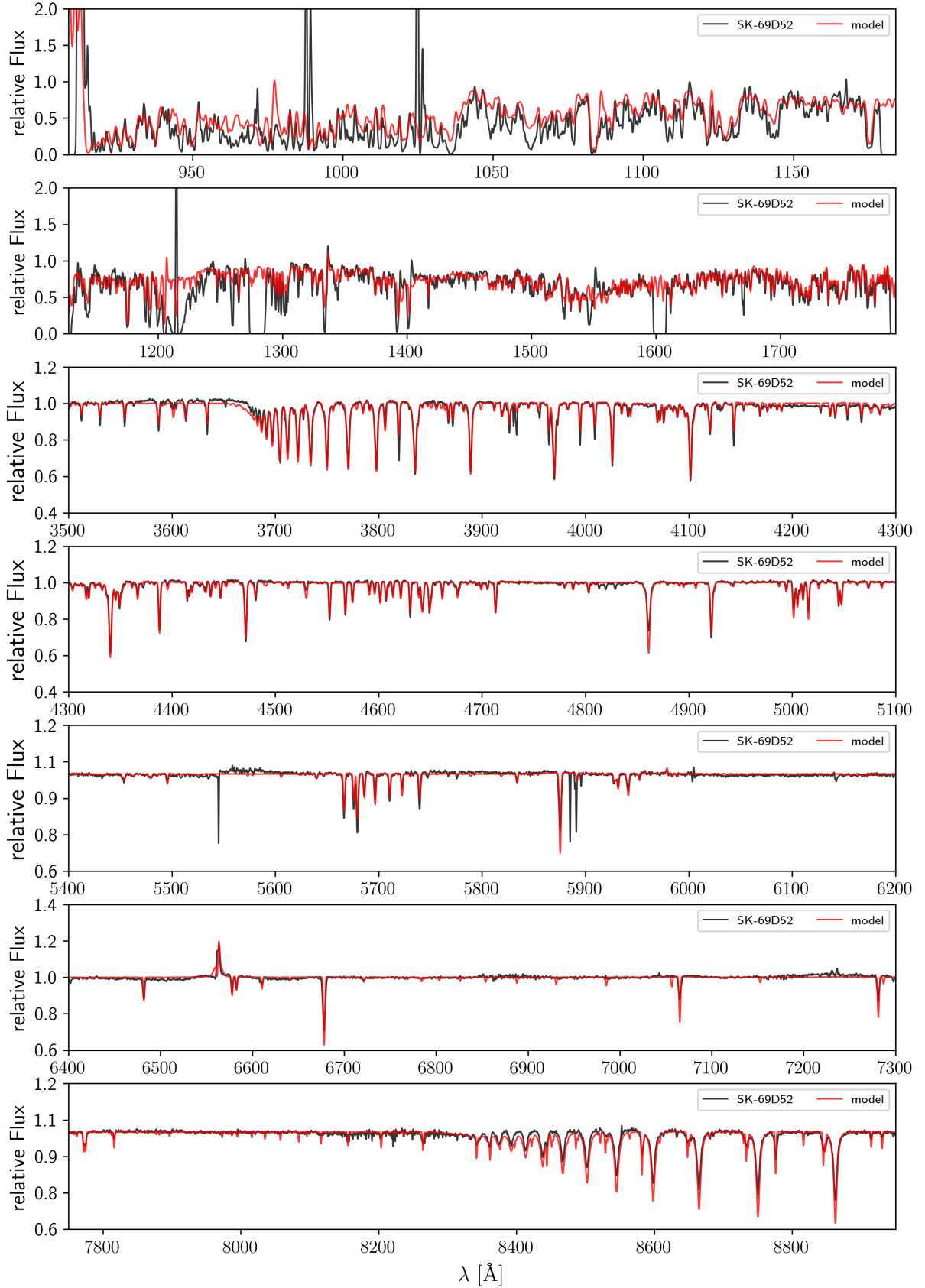
Fig. H.11: An overall view of the best fit (red solid line) to key regions of the observed spectrum (black solid line) of Sk −67° 14. From the top, the first panel is the FUV FUSE range, containing interstellar features such as *Lyδ* λ950, *Lyγ* λ973, and *Lyβ* λ1026. Second and third panels are COS G130M+G160M FUV and STIS E230M NUV spectral ranges, respectively, and we note some interstellar features: *Lyα* λ1216, O I + P II λ1302, C II λ1335, Si II λ1527, and Al IIλ1671. The rest of the panels are the UBV and VIS XShooter spectra, with the break between the two arms at ≈ 5600 Å. The lines Ca II H + K and Na I D are interstellar features.
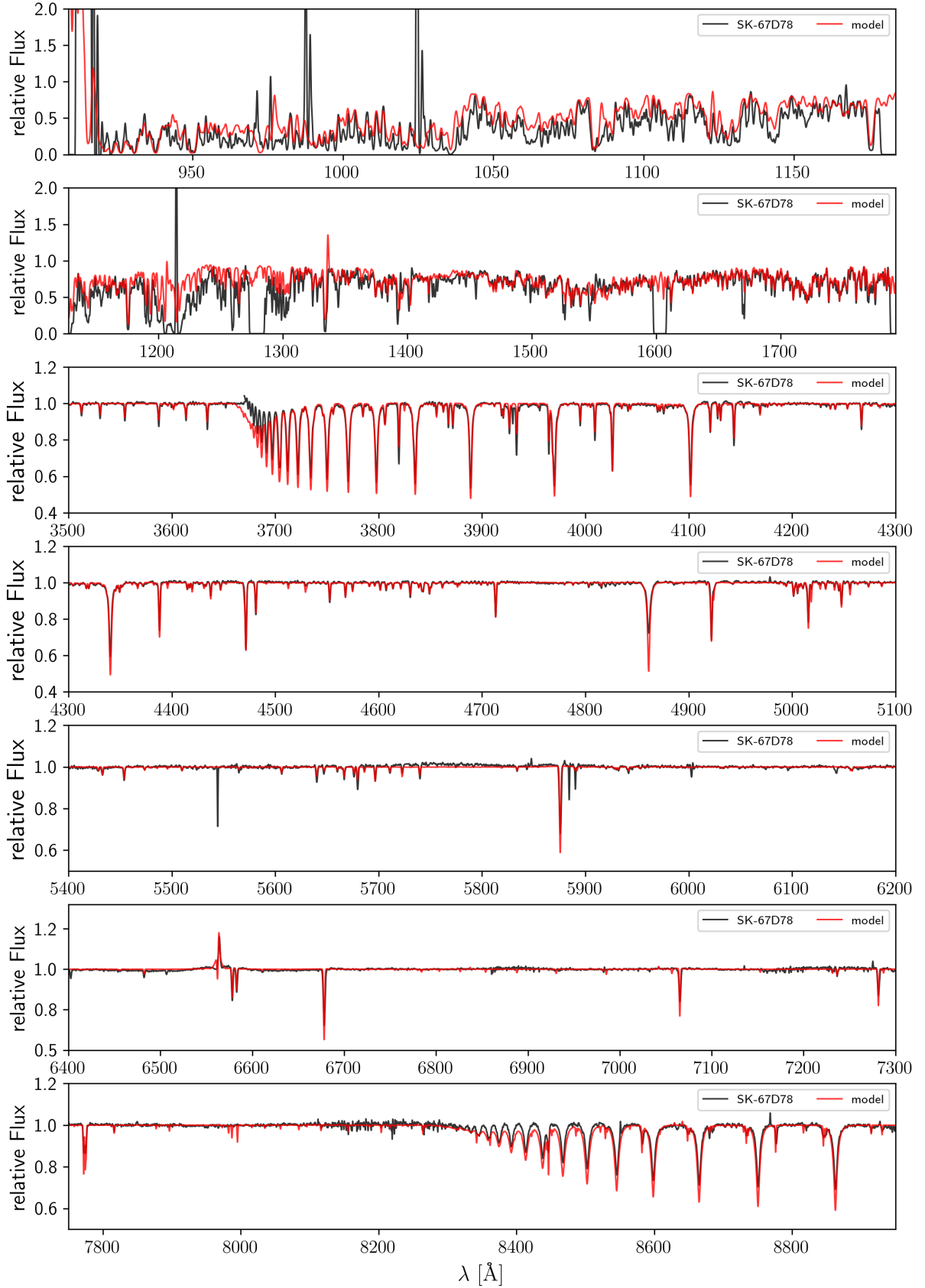
Fig. H.12: An overall view of the best fit (red solid line) to key regions of the observed spectrum (black solid line) of Sk −69° 52. From the top, the first panel is the FUV FUSE range, containing interstellar features such as *Lyδ* *λ*950, *Lyγ* *λ*973, and *Lyβ* *λ*1026. Second and third panels are COS G130M+G160M FUV and STIS E230M NUV spectral ranges, respectively, and we note some interstellar features: *Lyα* *λ*1216, O I + P II *λ*1302, C II *λ*1335, Si II *λ*1527, and Al II*λ*1671. The rest of the panels are the UBV and VIS XShooter spectra, with the break between the two arms at ≈ 5600 Å. The lines Ca II H + K and Na I D are interstellar features.

Fig. H.13: An overall view of the best fit (red solid line) to key regions of the observed spectrum (black solid line) of Sk −67° 78. From the top, the first panel is the FUV FUSE range, containing interstellar features such as *Lyδ* λ950, *Lyγ* λ973, and *Lyβ* λ1026. Second and third panels are COS G130M+G160M FUV and STIS E230M NUV spectral ranges, respectively, and we note some interstellar features: *Lyα* λ1216, O I + P II λ1302, C II λ1335, Si II λ1527, and Al IIλ1671. The rest of the panels are the UBV and VIS XShooter spectra, with the break between the two arms at ≈ 5600 Å. The lines Ca II H + K and Na I D are interstellar features.
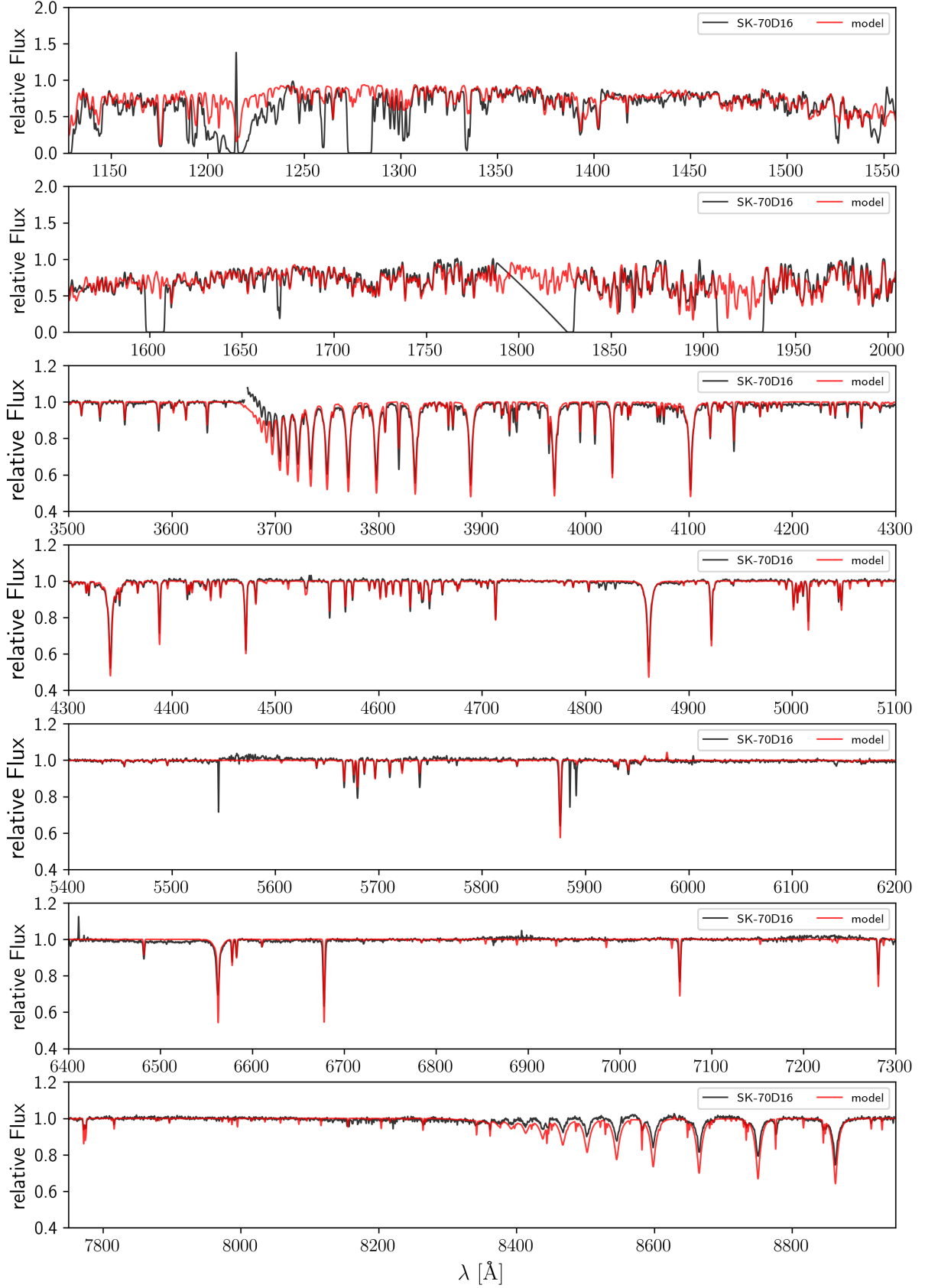
Fig. H.14: An overall view of the best fit (red solid line) to key regions of the observed spectrum (black solid line) of Sk −70° 16. From the top, the first and second panels are COS G130M+G160M FUV and COS G160M+G185M NUV spectral ranges, respectively, and we note some interstellar features: *Lyα* *λ*1216, O I + P II *λ*1302, C II *λ*1335, Si II *λ*1527, and Al II*λ*1671. The rest of the panels are the UBV and VIS XShooter spectra, with the break between the two arms at ≈ 5600 Å. The lines Ca II H + K and Na I D are interstellar features.
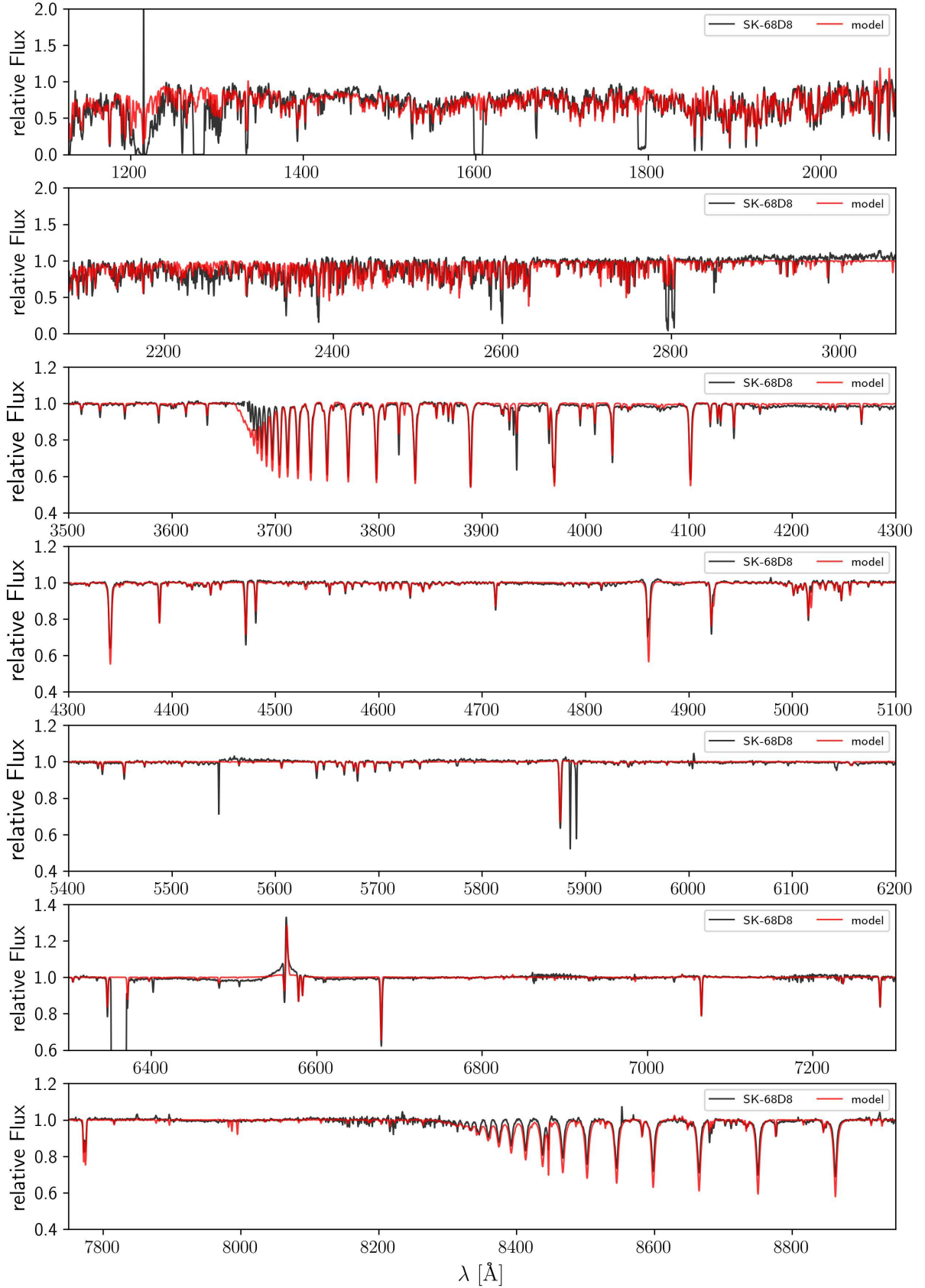
Fig. H.15: An overall view of the best fit (red solid line) to key regions of the observed spectrum (black solid line) of Sk −68° 8. From the top, the first and second panels are COS G130M+G160M FUV and STIS E230M NUV spectral ranges, respectively, and we note some interstellar features: *Lyα* λ1216, O I + P II λ1302, C II λ1335, Si II λ1527, and Al IIλ1671. The rest of the panels are the UBV and VIS XShooter spectra, with the break between the two arms at ≈ 5600 Å. The lines Ca II H + K and Na I D are interstellar features.
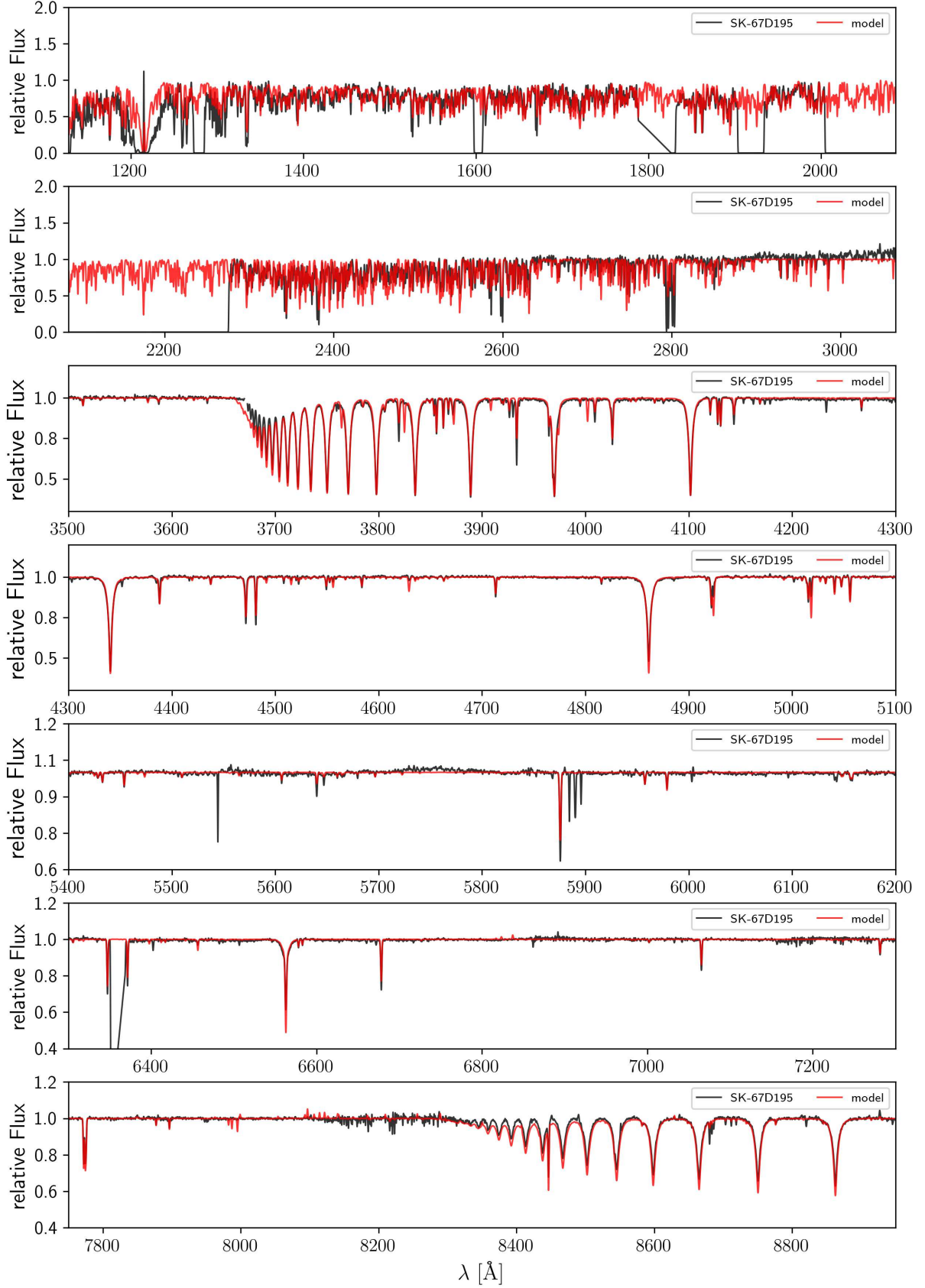
Fig. H.16: An overall view of the best fit (red solid line) to key regions of the observed spectrum (black solid line) of Sk −67° 195. From the top, the first and second panels are COS G130M+G160M FUV and STIS E230M NUV spectral ranges, respectively, and we note some interstellar features: *Lyα* λ1216, O I + P II λ1302, C II λ1335, Si II λ1527, and Al II λ1671. The rest of the panels are the UBV and VIS XShooter spectra, with the break between the two arms at ≈ 5600 Å. The lines Ca II H + K and Na I D are interstellar features.